JOURNAL OF GEOPHYSICAL RESEARCH, VOL. 91, NO. B7, PAGES 7261-7307, JUNE 10, 1986

MEASUREMENTS OF MANTLE WAVE VELOCITIES AND INVERSION FOR LATERAL HETEROGENEITIES AND ANISOTROPY 3. INVERSION

Henri-Claude Nataf,[1] Ichiro Nakanishi,[2] and Don L. Anderson

Seismological Laboratory, California Institute of Technology, Pasadena

Abstract. Lateral heterogeneity in the earth's upper mantle is investigated by inverting dispersion curves of long-period surface waves (100-330 s). Models for seven different tectonic regions are derived by inversion of regionalized great circle phase velocity measurements from our previous studies. We also obtain a representation of upper mantle heterogeneities with no a priori regionalization from the inversion of the degree 6 spherical harmonic expansion of phase and group velocities. The data are from the observation of about 200 paths for Love waves and 250 paths for Rayleigh waves. For both the regionalized and the spherical harmonic inversions, corrections are applied to take into account lateral variations in crustal thickness and other shallow parameters. These corrections are found to be important, especially at low spherical harmonic order. the "trench region" and fast velocities down to 250 km under shields. Below 200 km under the oceans, both S velocity and S anisotropy support a model of small-scale convection in which cold blobs detach from the bottom of the lithosphere when its age is large enough. The spherical harmonic models clearly demonstrate (a posteriori) the relation between surface tectonics and S velocity heterogeneities in the first 250 km: all shields are fast; most ridges are slow; below 300 km, a belt of fast mantle follows the Pacific subduction zones. However, at greater depths, large-scale heterogeneities that seem to bear no relationship to surface tectonics are observed. The most prominent feature at 450 km is a fast-velocity region under the South Atlantic Ocean. Smaller-scale heterogeneities that are not related to surface tectonics are also mapped at shallower depths: an anomalously slow region centered in the south central Pacific is possibly linked to intense hot spot activity; a very fast region southeast of South America may be related to subduction of old Pacific plate. Between 200 and 400 km, a belt of SV>SH anisotropy follows part of the ridge and subduction systems, indicating vertical mantle flow in these regions. The spherical harmonic results open new horizons for the understanding of convection in the mantle. Perspectives for the improvement of the models presented are discussed.

[1]Now at Laboratoire de Géophysique et Géodynamique interne, Université Paris-Sud, Orsay, France.

[2]Now at Department of Geophysics, Faculty of Science, Hokkaido University, Sapporo, Japan.

Paper number 5B5587.
0148-0227/86/005B-5587$05.00

The inversion is performed for transversely isotropic models that explicitly include shear wave and compressional wave anisotropy. Some a priori information based on physical considerations is used to link the variations in P and S anisotropies, and the variations in density, P velocity, and S velocity. S velocity is resolved down to a depth of about 450 km. S anisotropy is well resolved between 200 and 400 km depths. Our S velocity regionalized models exhibit trends related to surface tectonics: for the upper 200 km, the average velocity increases with the age of the crust; a very fast velocity below 300 km in

Contents

1. Introduction

Plate tectonics has demonstrated a major role for the lithospheric plates in the convective processes that govern mantle dynamics. Early on, the possibility of having other kinds of convective motions of different scales has been proposed: small-scale sublithospheric convection (Richter and Parsons, 1975), hot spot plumes (Morgan, 1971), and very large scale "tennis ball" convection (Hess, 1965). The evidence for such phenomena and the assessment of their relative importance, as well as the real organization of circulation at depth, are, however, difficult to produce when only surface observations are

available. Therefore the mapping of lateral heterogeneities as a function of depth in the mantle is essential to the study of mantle convection.

Seismology appears to be the only tool that can produce an image (though only an instantaneous one) of three-dimensional heterogneities within the earth. Indeed, both seismic body waves and surface waves have been used to investigate the earth's lateral heterogeneities. On a regional scale, body waves have proved useful in densely instrumented areas (Aki et al., 1977; Romanowicz, 1979; Babuška et al., 1984). On a global scale, surface waves provide a better coverage. Regional studies (Forsyth, 1975) and global studies using an a priori regionalization based on surface tectonics (Toksöz and Anderson, 1966; Anderson, 1967; Kanamori, 1970; Dziewonski, 1971) were in fact among the first to provide information about the depth stucture of the convective heterogeneities on the scale of the tectonic plates. Some of these studies preceded the formulation of the plate tectonics hypothesis.

Recent developments in long-period digital networks, the improved modeling of source processes, and the performances of digital computers have prompted a new approach to the problem. Spherical harmonic expansions of the heterogeneities, with no a priori regionalization, have now been obtained (Nakanishi and Anderson, 1982, 1984; Nataf et al., 1984; Woodhouse and Dziewonski, 1984).

In the present study, models of upper mantle lateral heterogeneities will be presented from both the regionalized and the spherical harmonic approach. The main advantage of the regionalization approach is that very accurate measurements can be performed. Phase velocities are measured on complete great circle paths so that the effects of the phase at the source cancel out (Satô, 1958). However, by using great circle observations alone, even though they are very accurate, only the even spherical harmonic components of the real heterogeneities can be retrieved (Backus, 1964). This basic weakness of great circle data can be bypassed if it is assumed a priori that the heterogeneities at depth are related to surface tectonics. The earth can then be divided in several different regions, and the average surface wave velocities over each region can be determined (Toksöz and Anderson, 1966). Depending on the appropriateness of the a priori choice, the way that great circle observations are actually explained varies. Souriau and Souriau (1983) have tested the variance reduction achieved by several proposed regionalizations and concluded that the regionalization of Okal (1977) was the best. It includes four oceanic regions corresponding to different age slices of the seafloor, a region for trenches and marginal seas, a shield region, and a mountainous region. Using great circle phase velocity measurements, Nakanishi and Anderson (1983) (hereafter referred to as NA1) have obtained average dispersion curves for both Love and Rayleigh waves for each of the seven regions of Okal's regionalization. Here we invert these dispersion curves and obtain the variations of shear wave velocity and anisotropy as a function of depth for each region. Love and Rayleigh waves are inverted simultaneously with anisotropy as an explicit inversion parameter whose resolution is discussed directly. The models we obtain describe useful properties of convection on the scale of the tectonic plates. However, as only that scale has been put in a priori, heterogeneities at any other scale (smaller or larger) have been mixed into what we treat as characteristic of the plate circulation.

In the spherical harmonic expansion approach, no such problem exists. For that method, direct earthquake-to-station wave trains are analyzed. Were the data flawless and the coverage at the surface of the earth complete, it would then be possible to retrieve local dispersion curves at any point at the surface of the earth with no a priori regional assumptions. Of course, the real situation is not this ideal. In particular, for this kind of data it is necessary to correct for the phase pattern at the source, so that the data are not as accurate as the great circle data. With the coverage achieved with about 250 paths, Nakanishi and Anderson (1984) (hereafter referred to as NA2) were able to retrieve the coefficients of the spherical harmonic expansion of dispersion curves up to degree 6. It is these coefficients that we invert in the present work, expanding on the results already presented by Nataf et al. (1984). Except for the regionalization, we choose the same kind of parameterization and a priori information as in the regionalized inversion so that direct comparisons can be made. The spherical harmonic representation, although coarse as yet, is practical for calculating correlations with other geophysical data (such as heat flow and the geoid). It is also a convenient frame of reference well suited for comparisons and for gradual refinement.

Before performing our inversions, we applied some corrections to take into account the lateral variations of crustal thickness and other shallow features. We find these corrections to be quite significant at low order, even for long-period surface waves.

Anisotropy is an important parameter for two reasons: first, it could be responsible for a significant part of the observed variability in surface wave velocities, and second, it could bring some valuable information on flow in the mantle. Our models are transversely isotropic, including both P and S anisotropy. The six parameters of such models cannot be resolved from the fundamental modes alone of surface waves. It is thus necessary to bring in some extra a priori information.

The inversion method we use was chosen in order to meet these requirements. We adopt the method of Tarantola and Valette (1982b). It is very flexible, in the sense that many kinds of a priori information can be easily built in through an a priori covariance matrix on the parameters. In particular, we can impose a similar S anisotropy and P anisotropy, using a priori constraints deduced from field observations on peridotites. We also place some constraints that link the variations of density and P velocity to S velocity variations. All along, we try to assess the reliability of the results that we present by displaying the usual inversion diagnostics (resolution kernels, a posteriori standard deviations, fits to the data) and the results of some other tests.

As in almost all seismological studies up to now, the data used in this study have been derived under the so-called geometric optics approximation. For surface waves this really means

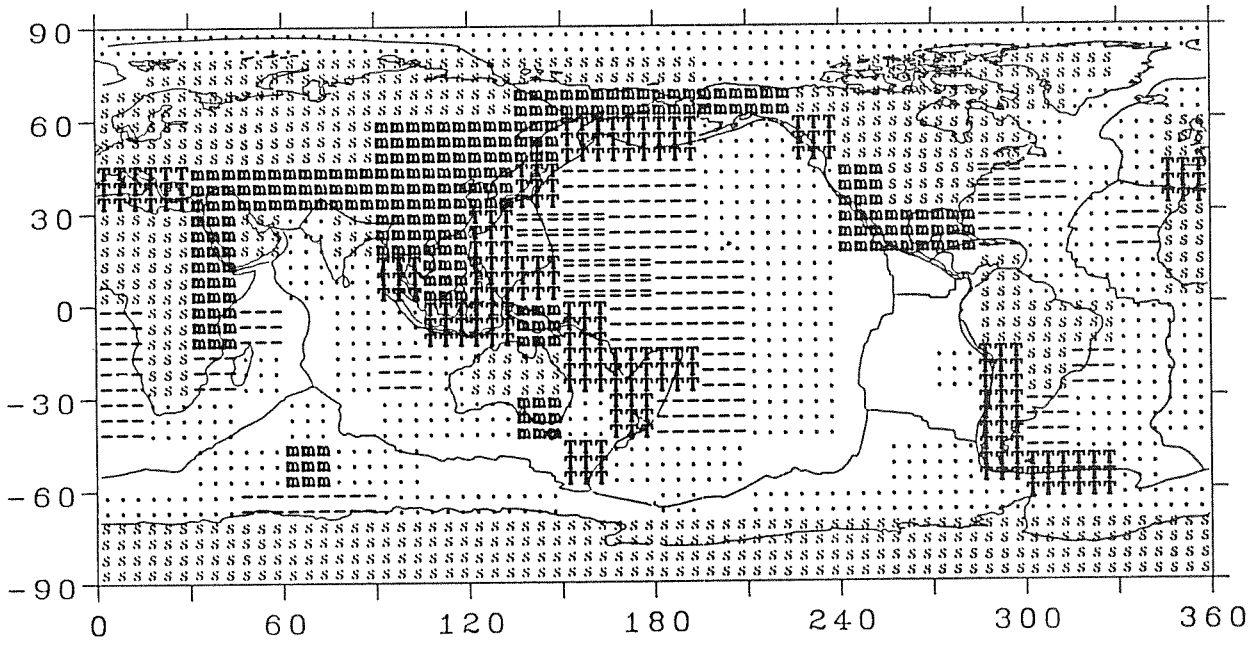

Fig. 1. Okal's (1977) regionalization. The grid size is 5°x5°. Symbols are blank, ocean 0-30 Ma; dots, 30-80 Ma; dashes, 80-135 Ma; equals, older than 135 Ma; "T", trench and marginal seas; "m", Phanerozoic mountains; "s", shields. Cylindrical equidistant projection. The same projection is used throughout this paper.

two things: first, that we neglect the difference between the measured phase velocity and the asymptotic phase velocity derived from Jean's formula, and second, that we consider that phase and group velocities of surface waves are affected only by the heterogeneities that underlie the source-receiver great circle path. The bias introduced by the first approximation can be evaluated a priori and is discussed in NA2 and in the data section. On the other hand, the validity of the second approximation depends on the amplitude of the heterogeneities and can only be assessed a posteriori once an aspherical model of the earth has been derived. We therefore consider that problem in the discussion section.

2. Data

Surface waves recorded at the International Deployment of Accelerometers (IDA) and the Global Digital Seismographic Network (GDSN) stations have been analyzed for 25 large earthquakes that occurred in 1980. Phase and group velocities of the fundamental modes have been measured on approximately 200 paths for Love waves and 250 paths for Rayleigh waves, with periods from 100 to 330 s. The data retrieval and analysis are described in NA1 and NA2.

Accurate great circle measurements have been performed (NA1) and have been used together with an a priori regionalization. Velocities have also been measured on earthquake-to-station paths, some care being taken to correct for the effects of the source mechanism and finiteness (NA2).

2.1. Regionalized Phase Velocities

We use the a priori regionalization proposed by Okal (1977) and shown in Figure 1. Seven types of regions are defined, according to their tectonic setting. There are four oceanic types corresponding to four age slices of the oceanic floor: region A (age > 135 Ma), region B (80-135 Ma), region C (30-80 Ma), region D (0-30 Ma). A separate type (region T) includes trenches and marginal seas. Two continental types are defined: mountainous regions (M) and shields (S). This regionalization is successful in reducing the variance of great circle observations (Souriau and Souriau, 1983). The variance reduction for great circle phase velocity measurements amounts to about 80% for Rayleigh waves and 60% for Love waves for periods from 150 to 300 s (NA1).

Regionalized phase slowness is obtained by using the now classical approach of Toksöz and Anderson (1966): the observed slowness at a given period on a given great circle path is the average of the slowness of the different regions taken with weights proportional to their length contribution to the path. By least squares inversion of the data observed on 200 paths for Love waves and 250 for Rayleigh waves, it is possible to retrieve the dispersion curves from 100 to 330 s for the seven individual regions (NA1). The regionalized dispersion curves thus obtained (Nakanishi and Anderson, 1983, Tables 7 and 8 and Figures 17 and 18) form the data set of the first part of the present study. It is used to determine the seismic velocity structure as a function of depth for the seven different tectonic regions.

2.2. Phase and Group Velocities in Spherical Harmonics

The information contained in great circle measurements is restricted to that part of the earth's lateral heterogeneities that is symmetric with respect to the earth's center: the even terms of the spherical harmonic representation of

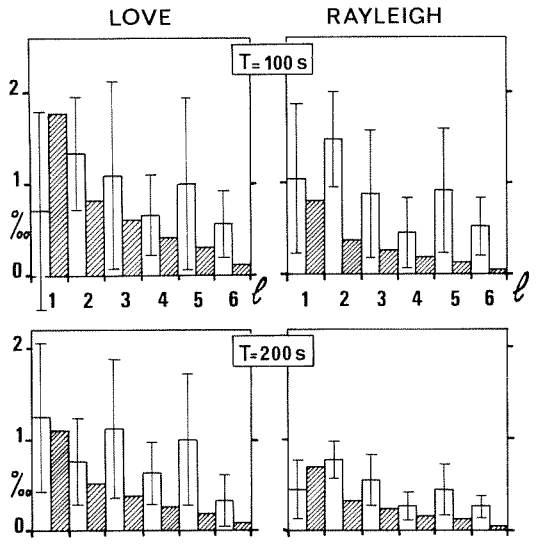

Fig. 2. Power spectrum of the corrections due to shallow layers (hatched rectangles), compared to the spectrum of the measured phase slowness variations plotted with their 2σ error bars, at periods of 100 and 200 s for Love and Rayleigh waves. Note that the correction is quite significant at low spherical harmonic order l.

the lateral heterogeneities (Backus, 1964). On the contrary, single-station measurements are sensitive to both even and odd terms. A convenient way for describing lateral heterogenities of quantities at the surface of the earth is indeed to use a spherical harmonic decomposition. The value of the quantity S at a point (θ,φ) on the surface of the earth is expressed as

$$S(\theta,\varphi) = \sum_{l=0}^{\infty} \sum_{m=0}^{l} (A_l^m \cos m\varphi + B_l^m \sin m\varphi) p_l^m(\theta) \qquad (1)$$

The spherical harmonics are fully normalized with

$$p_l^m(\theta) = \left[(2-\delta_m^0)(2l+1)\frac{(l-m)!}{(l+m)!}\right]^{\frac{1}{2}} P_l^m(\cos\theta) \qquad (2)$$

where the $P_l^m(\cos\theta)$ are the associated Legendre polynomials (see Stacey, 1977, pp. 319-323). In theory, it is possible to obtain a complete knowledge of the earth's lateral heterogneities by using single-station velocity measurements. In practice, this knowledge is limited by the errors in the data and by the coarseness of the coverage of surface wave paths on the earth. From least squares inversion of the actual data, a representation truncated to a maximum order L is obtained. With approximately 200 paths for Love waves and 250 paths for Rayleigh waves and considering the accuracy of the measurements, it was found that a good precision on the spherical harmonic coefficients could be obtained for L = 6 (NA2).

Phase and group dispersion curves are constructed with periods from 100 to 330 s for both Love and Rayleigh waves, for each of the 49 components of the L = 6 representation. At long period the approximation made in NA2 that the phase velocity is sampled uniformly over the great circle path, the zeroth-order approximation, breaks down. The first-order approximation has been derived by Schwab and Kausel (1976) for Love waves and by Wielandt (1980) for Rayleigh waves. The first-order correction increases with the increase of period and with the decrease of distance between receiver and poles and depends on the source focal mechanism. By evaluating that correction in the actual geometry and by analyzing synthetic seismograms, NA2 found that the bias in the zeroth-order approximation was at most equal to the estimated error on the data in the case of the largest periods that were analyzed (330 s). That effect was therefore neglected. To be on the safe side, we exclude from the inversion all data with periods larger than 270 s. Apart from that, the spherical harmonic dispersion curves obtained by Nakanishi and Anderson (1984, Tables 8, 9, 10 and 11) form the data set of the second part of the present study. We invert these to determine the three-dimensional seismic velocity structure of the upper mantle, limited to order 6 lateral variations.

3. Shallow Layer Corrections

Surface waves are very sensitive to the uppermost layers of the earth. In particular, the thickness of the crust, which can vary by a factor of 6 between oceans and continents, is responsible for large variations in the phase and group velocities of surface waves. Of course, the shorter the period, the larger the effect; but even for 300 s Rayleigh waves, the effect is quite important. The waves that we consider here (100-300 s Love and Rayleigh waves) thus suffer notable phase shifts due to the uppermost layers. It is therefore necessary and crucial to correct the data for the contribution of shallow layers as carefully as possible. This has been done before both the regionalized and the spherical harmonic inversions were performed. We have considered four factors: crustal thickness, P_n-S_n velocities, ocean depth, and topography. The distribution at the surface of the earth of the last two factors is obtained from a 5°x5° compilation. Crustal thickness is the dominant factor. Unfortunately, its distribution is not as accurately known. A compilation by Soller et al. (1981) provides countour maps of crustal thickness and P_n velocities over much of the world. Visual averages were taken on 15°x15° cells, and empty cells were filled in by using a predictor based on tectonic setting according to Okal's (1977) regionalization, in a way similar to Chapman and Pollack's (1975) procedure for heat flow.

In the regionalized approach, histograms are constructed for each of the seven regions, and the average is taken and built into the starting model of each region. The histograms are presented in Appendix A.

For the spherical harmonic inversion, we directly correct the data for shallow layers effects, so that a single starting model can be used for all 49 coefficients. We expand the distribution of the four shallow factors in spherical harmonics, calculate the shift in surface wave velocity due to a unit change in every factor at all pertinent periods, and deduce the resulting correction to apply to each of the 49 spherical harmonic dispersion curves. Maps and corrections are shown in Appendix A.

Figure 2 shows the power spectra of the cor-

rections at selected periods, compared to the power spectra of the measured variations in phase slowness. The power w_l of a quantity S is expressed as

$$w_l = \frac{1}{\sqrt{2l+1}} \left\{ \sum_{m=0}^{l} \left[(A_l^m)^2 + (B_l^m)^2 \right] \right\}^{\frac{1}{2}} \qquad (3)$$

where A_l^m and B_l^m are the spherical harmonic coefficients of the quantity S as defined in equation (1).

It is worth stressing that these shallow layer corrections are especially large at low order. This has primarily to do with the distribution of continents: the too well-known north-south asymmetry and the strong sectorial zoning, both low-order features.

The corrections are particulary important for Love waves: whereas the original Love wave velocity maps at 100 seconds show no systematic difference between oceans and continents (NA2), the corrected maps do. Indeed, the thick crust of continents (slow) nearly compensates the continental lithosphere (fast), so that the overall average continental velocity is close to the oceanic one.

The two points we just mentioned demonstrate that it is crucial to correct for the effects of shallow layers in order to retrieve a realistic picture of the upper mantle heterogeneities even and, especially, for its large-scale features.

4. Anisotropy

4.1. Evidence for Anisotropy

There is now considerable evidence for seismic velocity anisotropy in the earth's mantle. For a general review of that evidence, the reader is referred to two special issues of the Geophysical Journal of the Royal Astronomical Society (Bamford and Crampin, 1977; Crampin et al., 1984). On a regional scale, P_n studies have revealed that in the oceanic lithosphere, P waves traveling in the oceanic plate spreading direction are consistently faster (by about 5%) than those traveling perpendicular to the spreading direction (e.g., Hess, 1964; Raitt et al., 1969). Similar results have been obtained for continents, although the tectonic setting is usually more complex (e.g., Bamford, 1973; Vetter and Minster, 1981; Fuchs, 1983; Hearn, 1984). On a wider scale, the long-reported discrepancy between Love and Rayleigh waves in many provinces can be explained if a ~3% polarization anisotropy of S waves is allowed for (e.g., Anderson, 1961; Harkrider and Anderson, 1962; Forsyth, 1975; Schlue and Knopoff, 1977; Yu and Mitchell, 1979; Journet and Jobert, 1982).

On a global scale, S and P wave anisotropy had to be introduced by Dziewonski and Anderson (1981) in order to fit the global earth normal modes and body waves data set. The Preliminary Reference Earth Model (PREM) that they obtain by inversion of that data set displays P and S anisotropies up to 4% for depths between 80 and 200 km. Although Dziewonski and Anderson (1981) do not show the resolution kernels for their inversion, we think that the data set they use provides good constraints on the anisotropy of S waves at least. Indeed, we calculated the resolution kernels obtained for the inversion of the 120 normal modes of their data set that are most sensitive to upper mantle structure, and we found that S anisotropy was well resolved in the region where their model seems to require anisotropy. The resolution kernels are shown in Appendix B.

From a seismological point of view, it therefore seems that the long-held hypothesis of isotropy has to be abandoned. This statement is strengthened by evidence from petrology and geology; it has long been known that olivine, presumably a major constituent of the upper mantle above 400 km, is strongly anisotropic. Velocity measurements on olivine single crystals indicate anisotropies up to 25% for P waves and 20% for S waves (Kumazawa and Anderson, 1969). Unless olivine crystals are randomly oriented in the upper mantle, anisotropy should be the rule rather than the exception. Indeed petrofabric observations on ophiolites and other mafic massifs indicate that crystal orientation is strongly controlled by the ambient strain field and is therefore quite consistent on regional scales (Nicolas et al., 1971; Peselnick et al., 1974; Peselnick and Nicolas, 1978). Furthermore, Christensen and Salisbury (1979) show that using the petrofabric data for the Bay of Islands ophiolite together with the elastic moduli of olivine single crystals, they predict an azimuthal anisotropy for P waves that is in excellent agreement with the actual oceanic P_n data of Morris et al. (1969). Tectonic plate motions and convection currents in the mantle are associated with large-scale stress and strain fields, so that anisotropy can be expected on a large scale in the upper 400 km of the mantle.

4.2. Azimuthal and Polarization Anisotropy

The most general form of anisotropy involves 21 elastic coefficients instead of the two which characterize an isotropic body. However, surface waves are affected by only a subset of the independent combinations of these elastic coefficients: six for Love waves and 12 for Rayleigh waves (Smith and Dahlen, 1973). A special case of anisotropy is transverse isotropy with a vertical axis of symmetry: it corresponds to the most general kind of anisotropy that can be given to a radially symmetric earth (Backus, 1967). Transverse isotropy involves five elastic coefficients (Love, 1927); there is no anisotropy in the horizontal plane, but the velocities of body waves vary in a vertical plane, depending on the angle between the direction of propagation and the vertical. Also, S waves have different velocities depending on whether they are polarized in the vertical plane (SV) or in the horizontal plane (SH) (Anderson, 1961). For that reason, transverse isotropy is sometimes called polarization anisotropy. Because it involves no azimuthal dependence, transverse isotropy can be incorporated into standard methods to calculate normal modes of a layered earth (Anderson, 1961; Backus, 1967; Takeuchi and Saito, 1972). For these reasons, transverse isotropy was chosen to describe the Preliminary Reference Earth Model (PREM) of Dziewonski and Anderson (1981).

In the present study, we will also restrict our attention to transversely isotropic models. There is no a priori reason to believe that this type of anisotropy is dominant over azimuthal anisotropy on a regional scale. In fact, much of

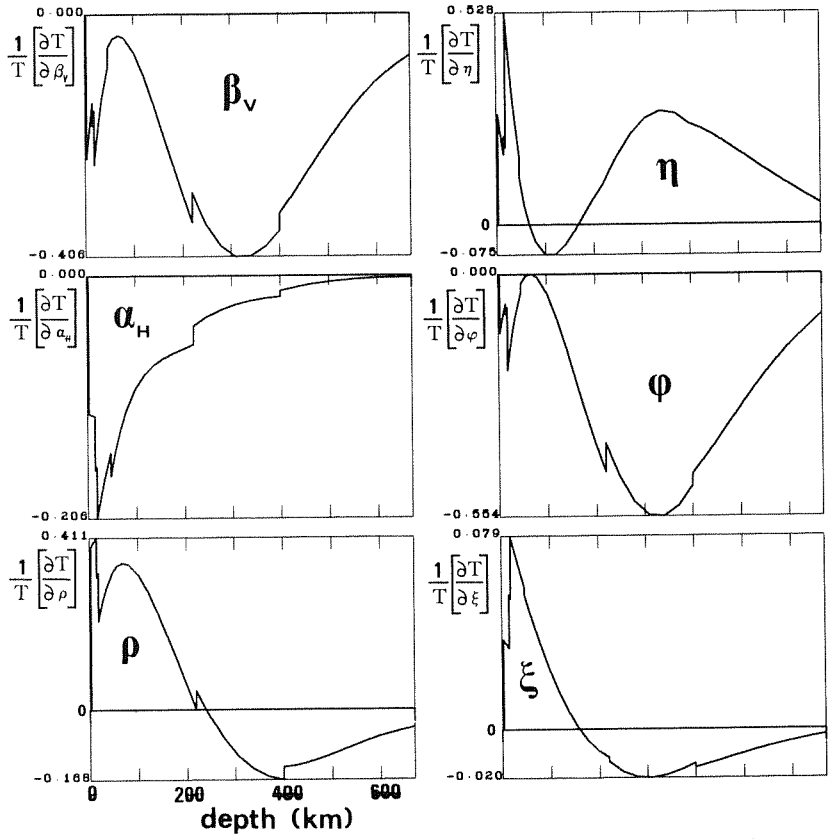

Fig. 3. Partial derivatives of the period T of the ${}_0S_{40}$ normal mode (T~210 s Rayleigh wave) with respect to the six parameters of a transversely isotropic earth (ρ, α_H, β_V, ξ, ϕ, and η) as a function of depth in the upper mantle. Units are 10^{-3} km^{-1} for ξ, ϕ, and η; 10^{-3} km^{-1} g^{-1} cm^3 for ρ; and 10^{-3} km^{-1} km^{-1} s for α_H and β_V. The model used to calculate the partials is PREM.

the evidence that we have for anisotropy comes from the azimuthal variation, which can reach several percent. However, even if the most general kind of anisotropy is considered, the average over all azimuths of surface wave velocities depends on five combinations of the elastic coefficients only. These combinations reduce the actual medium to a transversely isotropic medium whose equivalent coefficients can be calculated from Smith and Dahlen's (1973) more general expressions, as shown in Appendix C. Therefore, if a good azimuthal coverage is achieved for every region, or spherical harmonic, the azimuthal average replaces the actual azimuthal variation and we have an equivalent transversely isotropic medium. Of course, valuable information on the azimuthal dependence is lost in that process. In that respect, our approach must be regarded as a first step. Indeed, Tanimoto and Anderson (1984, 1985) using a data set extended from NA2 retrieve both azimuthal-dependent and -independent terms for the larger-scale heterogeneities. Nevertheless, it must be kept in mind that the information in fundamental Love and Rayleigh waves is limited and that the direct retrieval of the lateral heterogeneities of the density and the five elastic coefficients of a transversely isotropic earth model is beyond reach at present.

In the following, we define the five independent combinations of the elastic coefficients as from Takeuchi and Saito (1972):

$$\alpha_H = \sqrt{A/\rho}$$
$$\beta_V = \sqrt{L/\rho}$$
$$\xi = N/L = (\beta_H/\beta_V)^2 \qquad (4)$$
$$\phi = C/A = (\alpha_V/\alpha_H)^2$$
$$\eta = \frac{F}{A-2L}$$

where the A, C, F, L, and N are the five elastic coefficients of the equivalent transversely isotropic medium, as given in Appendix C. The parameter ξ describes the anisotropy of S waves, ϕ describes the anisotropy of P waves, and η is the fifth parameter needed to describe fully transverse isotropy.

4.3. Seismological and Geodynamical Relevance of Anisotropy

Once one admits the existence of anisotropy in the earth's upper mantle, it can be tested whether anisotropy leads to sizeable effects for the data set we are dealing with: the dispersion curves of fundamental Love and Rayleigh waves. The goal of this subsection is to show that this is indeed the case and furthermore that anisotropy carries valuable information concerning the mechanics of the mantle.

In dealing with lateral heterogeneities, it

should be recognized that velocity variations induced by changes in crystal orientation can exceed those due to changes in temperature. Figure 3 illustrates this point by displaying the partial derivatives of the period of the ${}_0S_{40}$ mode (~212 s Rayleigh wave) with respect to density and the five other parameters. It can be observed that the shapes of the β_V and ϕ kernels are almost identical. This means that there exists an almost complete trade-off between SV velocity and P wave anisotropy. Paying attention now to the amplitudes of the kernels, let us see what kind of parameter variations we need in order to explain a phase velocity anomaly of, say, 0.03 km/s (typical of the observed anomalies at this period). Changing the parameters over a 100-km-thick layer around the depth of maximum amplitude (~300 km), the β_V variation that we need to explain the anomaly is 0.12 km/s versus a ϕ variation of 0.1. Going one step further, a β_V variation of 0.12 km/s can be due to a ~350°C temperature variation, whereas a ϕ variation of 0.1 (a 5% P anisotropy variation) can be produced by a 90° shift of the preferred orientation of crystals in a realistic mantle (see Appendix D). We note that an undulation of about 100 km of the 400-km discontinuity would also cause the same phase velocity anomaly.

Based on geodynamical considerations, it is difficult to expect temperature variations at a given depth in excess of, say, 600°C in the upper mantle. On the other hand, extrapolating from the observed azimuthal dependence of P_n waves, P anisotropy up to 7% cannot be ruled out. On both seismological and physical grounds it thus appears that anistropy in the upper mantle can contribute quite significantly to the observed lateral heterogeneities of surface wave velocities. This is why it is necessary to include anisotropy in the inversion of surface waves and free oscillation data.

Although this, of course, complicates the procedure, it should be emphasized that anisotropy can be a useful tool for geodynamics. Whereas velocity variations can help us map temperature heterogeneities in the mantle and thus place constraints on its dynamics, anisotropy can help us trace convective motions in the mantle and thus place bounds on its kinetics. This is because motions in the mantle lead to preferential crystal orientations through their associated strain fields (McKenzie, 1979).

Anisotropy appears to be a necessary and useful complement for both seismology and geodynamics. This has indeed been recognized: early on, Hess (1964) pointed out that the azimuthal dependence of P_n velocities in the oceanic lithosphere was an important clue in favor of seafloor spreading; more recently, Anderson and Regan (1983) and Regan and Anderson (1984) built consistent oceanic velocity models including both thermal and orientation effects to fit surface wave data in the Pacific; Tanimoto and Anderson (1984, 1985) used the azimuthal anisotropy of surface wave velocities as a marker of convective motions in the mantle. In this paper we retrieve information on the transverse isotropy of the different tectonic regions as defined by Okal (1977) and of the spherical harmonic expansion of the upper mantle's lateral heterogeneities up to degree 6.

5. Inversion

5.1. Forward Problem

The forward problem consists in calculating the periods of the normal modes for a given spherical, anisotropic earth model. Indeed, as we will see in the next section, we transform our original phase and group velocity data into the period of normal modes with integer mode number. Our transformed data are then the periods of a given set of normal modes for every region or spherical harmonic coefficient. The model is defined by the values of the density, the five elastic coefficients, and the shear and bulk quality factors for all radii from the center of the earth to its surface. We use the computer program EOS written by A. Dziewonski to calculate for a given model and for each chosen normal mode its period, phase velocity, group velocity, and partial derivatives of the period with respect to the model parameters. The calculation includes the effects of sphericity, gravity, and dissipation. The program is adapted from F. Gilbert's isotropic earth program to include transverse isotropy following the guidelines of Takeuchi and Saito (1972). Backus (1967) was the first to deduce the scalar equations of elastic gravitational oscillations of a transversely isotropic, radially stratified, spherically symmetric earth.

We analyze fundamental surface waves with periods from 100 to 300 s, and can retrieve information only about the upper mantle. Therefore, in all the inversions that we perform, we leave the inner part of the earth unmodified: we use PREM parameters from the center of the earth to the top of the lower mantle (at a depth of 670 km). We also keep the quality factors of PREM unchanged for all radii. The upper mantle is divided into 34 layers, on top of which lay 13 layers of crust and ocean. Below the crust, seismic discontinuities are kept at depths of 80, 220, 400, and 670 km. Between these discontinuities, both the forward calculation and the inversion are conducted as continuous operations. All the models we present are at the reference period of 1 s (see Dziewonski and Anderson, 1981).

5.2. Inversion Algorithm

A glance at the partial derivatives displayed in the previous section makes it obvious that the data we have do not enable us to determine uniquely all six parameters for all radii in the upper mantle. Our problem is obviously underconstrained. In order to retrieve valuable and meaningful information, various inversion methods have been designed that all lead to some kind of well-constrained average of the parameters under study. Starting from the corner stone work of Backus and Gilbert (1967, 1968, 1970), various improvements have been proposed from either a conceptual or a practical point of view. Among those, the discovery of the importance of a priori information (be it explicit or hidden) as a major ingredient for constraining underconstrained problems has proved most useful (Franklin, 1970; Jordan and Franklin, 1971; Sabatier, 1977a,b; Jackson, 1979). This has led Tarantola and Valette (1982a) to propose a fully

"Cartesian" probalistic approach to inversion problems. The application of their very general formulation to the more specific but widespread problem of slightly nonlinear least squares inversion, along the lines of Backus and Gilbert, yields inversion algorithms that are both practical and conceptually pleasant (Tarantola and Valette, 1982b). They have the advantage over Backus and Gilbert's (1967, 1968, 1970) and Wiggins'(1972) algorithms in that they explicitly include a priori information on the parameters. The philosophy of Tarantola and Valette's algorithms can be summarized as follows: the answer obtained (a posteriori model with its error bar, or more generally its covariance matrix) is as close to "reality" as possible, given the data (with error bars), a theory that relates them to the model, and the a priori knowledge assigned to the model parameters (a priori model with its covariance matrix).

Mathematically, if the theory gives the "data" $\underline{d}$ for the model $\underline{p}$ through a functional g by $\underline{d} = \underline{g}(\underline{p})$ and if G is the matrix of the partial derivatives of g with respect to $\underline{p}$, the model $\underline{\hat{p}}$ that best fits the observed data $\underline{d}_o$ and the a priori information chosen (in a least squares sense) is given as the limit when $k \to \infty$ of $\underline{\hat{p}}_k$ defined by

$$\underline{\hat{p}}_{k+1} = \underline{p}_o + \left\{ C_{p_o p_o} G_k^T (C_{d_o d_o} + G_k C_{p_o p_o} G_k^T)^{-1} \times \left[\underline{d}_o - \underline{g}(\underline{\hat{p}}_k) + G_k \times (\underline{\hat{p}}_k - \underline{p}_o) \right] \right\} \quad (5)$$

where $C_{d_o d_o}$ is the covariance matrix for the data, $C_{p_o p_o}$ is the a priori covariance matrix for the model, and $\underline{p}_o$ is the a priori model. When the functional g is linear in $\underline{p}$, no iteration is needed, and the a posteriori model $\underline{\hat{p}}$ is found by setting k = 0 in equation (5). In that case, the a posteriori covariance matrix $C_{\hat{p}\hat{p}}$ on the model is analytically expressed as

$$C_{\hat{p}\hat{p}} = C_{p_o p_o} - C_{p_o p_o} G^T (C_{d_o d_o} + G C_{p_o p_o} G^T)^{-1} G C_{p_o p_o} \quad (6)$$

The a posteriori maxtrix $C_{\hat{p}\hat{p}}$ contains all the information we need concerning the "accuracy" with which our best fitting model $\underline{\hat{p}}$ is obtained. The diagonal terms give the a posteriori standard deviation on the model parameters, and the off-diagonal terms describe the trade-off between parameters at different depths. The trade-off is more commonly discussed in terms of "resolving kernels" (Backus and Gilbert, 1970) or a resolution matrix. For Tarantola and Valette's algorithm, the resolution matrix R is given by Montagner and Jobert (1981) as

$$R = C_{p_o p_o} G^T (C_{d_o d_o} + G C_{p_o p_o} G^T)^{-1} G \quad (7)$$

For nonlinear problems, no analytical matrix expression has been found for the a posteriori covariance matrix nor for the resolution matrix. However, the problem we study here is only slightly nonlinear, and computing the a posteriori covariance matrix using equation (6) at any step k gives pretty much the same answer, which should be reliable enough. For the same reason only a few iterations on k are needed to obtain a stable and convergent $\underline{\hat{p}}$ model.

In our case the model $\underline{p}$ is made of six continuous functions of the radius r, corresponding to the six parameters of a transversely isotropic earth (namely, ρ, α_H, β_V, ξ, ϕ, and η). The matrix formulation presented above is easily generalized to include continuous functions (Tarantola and Valette, 1982b). The resolution R is made of 6 x 6 continuous functions of the radius r and carries information about the usual depth resolution for each parameter but also about the "trade-off" between different parameters. The data $\underline{d}$ are the periods of the selected torsional and spheroidal normal modes.

From a practical point of view, the main advantage of Tarantola and Valette's (1982b) algorithm for our application is that it gives complete flexibility for defining the a priori covariance matrix of the parameters. This will prove useful for introducing a priori links between parameters: for example, we may have a priori physical reasons to believe that, at a given depth, density, P velocity, and S velocity should vary in the same way if their variations are due to variations in temperature. The use of an a priori covariance matrix on the parameters enables us to enter such a priori information, making it possible to constrain an otherwise very undetermined problem.

In the next section, some of these aspects will be exemplified as we use a very special application of Tarantola and Valette's algorithm (namely, finding a model curve to fit data that are its values and the values of its derivative at given points) in order to combine the informations brought by phase velocities on one hand and group velocities on the other.

6. Combining Phase Velocity and Group Velocity Information

6.1. Method

For the earthquake-to-station observations that are used to derive the spherical harmonic expansion of lateral heterogeneities, NA2 measured both phase and group velocities. Of course, if the phase velocity measurements were perfect, no further information would be brought by the group velocity measurements. However, as the measurements carry some errors, nontrivial information is brought by complementing phase velocity measurements with group velocity data (Anderson and Toksöz, 1963; Gilbert, 1976).

Group velocity data could be added to the phase velocity data set and partial derivatives calculated with respect to the model parameters and included in the inversion procedure. This approach, however, suffers two drawbacks: (1) the number of data is doubled, thus making the inversion computations much heavier, for a gain in information that might not justify it, and (2) partial derivatives for group velocities involve a numerical differentiation so that at least twice as many periods (Rodi et al., 1975) or modes must be calculated in the forward problem than needed for phase velocity inversion.

Furthermore, phase and group velocities are measured at a given period T, whereas in a spherical earth, computations are best done at a given mode number n. When relating a model to observations, it is therefore necessary to convert from

mode numbers to periods. For a correct interpolation to be made, more modes than actually needed must be calculated each time a model is tested. In the inversion procedure the data do not change, and it is logical to first convert these from a fixed period to a fixed and integer mode number. Only the same limited number of modes then needs to be calculated at each model-testing step.

To perform this conversion and combine the information brought by phase velocity and group velocity, we designed the following method:

The Rayleigh-Ritz formula defines the phase velocity C of a given mode in a spherical earth with radius $R_\oplus$ as $C = \omega/k = (2\pi/T)/[(n+1/2)/R_\oplus]$, where T is the period of the normal mode considered and n is its mode number. The group velocity U is $U = d\omega/dk = d(2\pi R_\oplus/T)/dn$. Introducing the variable $x = 2\pi R_\oplus/T$, we then have

$$n(x) = \frac{x}{C(x)} - \frac{1}{2} \tag{8}$$

$$\frac{dn}{dx}(x) = \frac{1}{U(x)} \tag{9}$$

If we can find a smooth continuous curve that relates n to x, it is easy to pick integer n values and read the corresponding x value and thereby deduce the period T of the normal mode n. The problem is therefore to find a smooth n(x) curve given the values it takes at selected points (from the phase velocity data in equation (8)) and given the values its derivative takes at selected points (from the group velocity data in equation (9)). This is a typical inversion problem and, as such, is treated as an example by Tarantola and Valette (1982b). The "model" is the continuous function n(x). The "data" are the phase velocity and group velocity measurements at selected x values. The standard deviations on these measurements are built into the covariance matrix for the data. The problem is linear, and the partial derivatives are the Dirac distribution for the phase velocity data and its derivative for the group velocity data. The a priori covariance matrix of the parameters is chosen as

$$C_{p_o p_o}\left[n(x_1), n(x_2)\right] = \sigma_o^2 \exp\left(-\frac{(x_1-x_2)^2}{2\,\Delta_o^2}\right) \tag{10}$$

where σ_o is the standard deviation of the a priori guess on n and Δ_o is the typical x length scale of permitted undulations. The a priori model p_o can be chosen as

$$n_o(x) = ax + b \tag{11}$$

where the constants a and b are roughly estimated. The inversion now is particularly simple because most integrations involved can be performed analytically (see Tarantola and Valette (1982b) for more details).

The correlation length Δ_o is arbitrarily chosen so as to avoid unwanted undulations in the a posteriori model n(x) curve and its derivative. A "best" smooth curve is then obtained, together with its a posteriori standard deviation calculated from the a posteriori covariance matrix of the parameters. Integer n values are picked, and the corresponding T(n) data read with their standard deviations. When actually dealing with the spherical harmonic coefficients of phase and group slowness, a slight modification of the method we just described is required. This is presented in Appendix E.

An advantage of our approach is that one can check how consistent phase and group velocities are, before trying to find an earth model to fit them. In our spherical harmonic inversion we use this facility to test how well determined the individual coefficients are.

6.2. Compatibility Between Phase and Group Velocity Data

If one can find a reasonably smooth curve to simultaneously fit phase and group velocity data, these data are consistent. On the contrary, if no reasonable curve can be found, there is some inconsistency between the two data sets. As phase and group velocities are measured and expanded independently, their consistency can be used as a criterion for judging how well determined and reliable are the individual coefficients of the spherical harmonic expansion.

This is best seen in some examples. Figure 4 displays the fits obtained for three individual coefficients that all appear to be quite consistent. For these three coefficients (B_2^2, A_4^3, and A_6^2) the smooth curve we invert for is found to give a good fit to the phase velocity measurements (drawn with their error bars), while its derivative also accurately fits the group velocity measurements (drawn with their error bars) for the chosen correlation length Δ_o. We therefore deduce that phase and group velocities are consistent for these particular spherical harmonic coefficients, which are probably well constrained by our data. This is confirmed by the fact that they all show fairly small error bars.

On the contrary, Figure 5 illustrates the case of "bad" coefficients. For these two coefficients, A_3^3 and A_5^2, no "reasonable" curve can be found that fits the phase and group velocity data simultaneously. They are inconsistent. The curve that we obtain can be seen as a reasonable curve that complies as best as possible with both data sets. For these coefficients, phase or group velocities or both, are not well constrained, and one or both are not reliable. This is confirmed by the large standard deviations that affect them. Our procedure usually tends to reduce the amplitude of such "bad" coefficients, while attempting to produce a reasonable compromise.

It is interesting to test all the coefficients using the qualitative criterion we just defined. Coefficients that have near-zero amplitudes at all periods for both phase and group velocities are automatically "good" but they are not very interesting because they contribute little to the lateral heterogeneneities. We are thus left with two types of coefficients: "good" ones for which phase and group velocities are consistent and which contribute significantly to lateral heterogenities, and "bad" ones that display some inconsistency between phase and group velocities and have large ampitudes. The second type of coefficients might lead to spurious results, so that it may be better to eliminate them at the end.

Listed as "good" coefficients are the following:

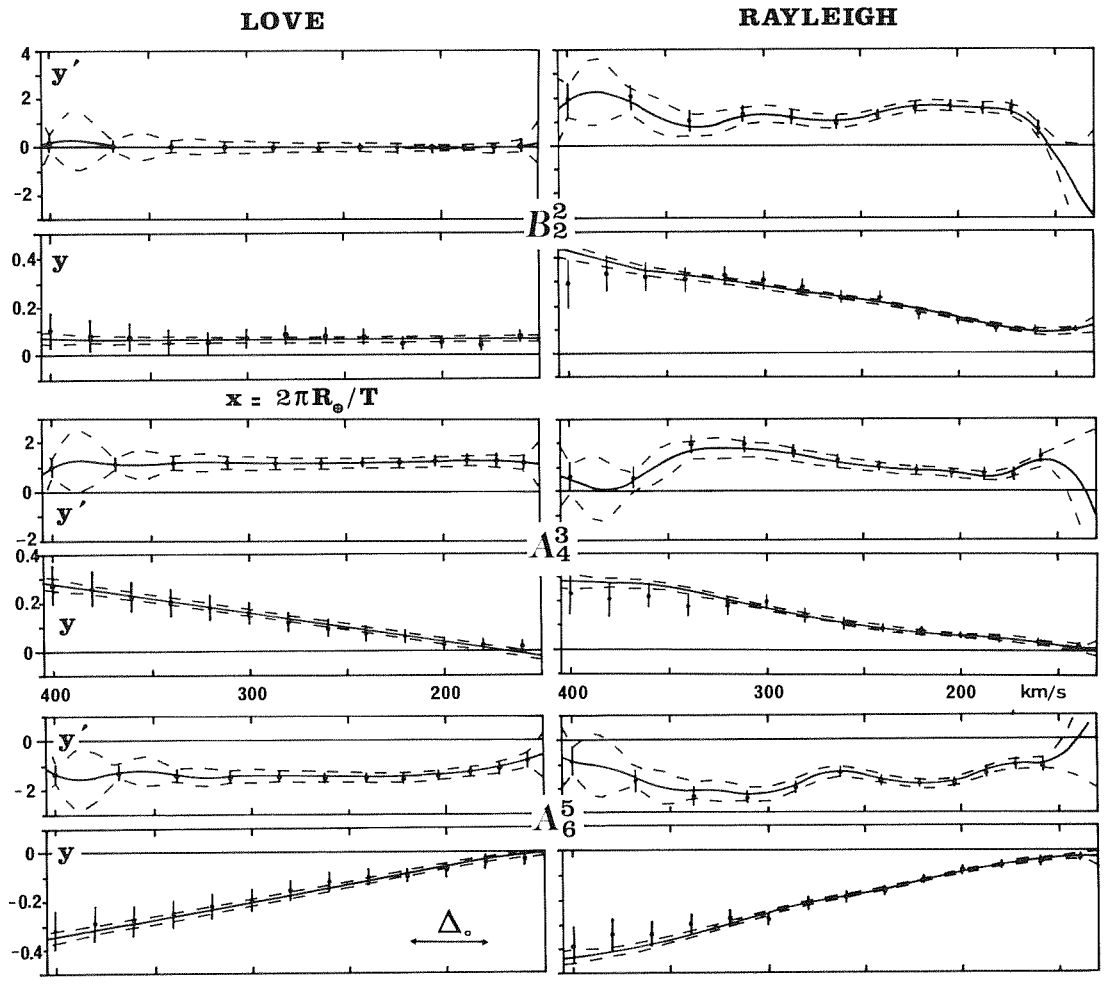

Fig. 4. Three examples of "good" spherical harmonic coefficients for which phase and group velocity data are found to be in agreement. The functions y' (transformed group velocity) and y (transformed phase velocity), as defined in Appendix E, are plotted against $x = (2\pi R_\oplus)/T$, where T is the period. The data points are drawn with their 2σ error bars. A unique continous model is built that fits the y data, while its derivative fits the y' data, using a special inversion algorithm. It is drawn with its a posteriori standard deviation (dashed lines). The horizontal bar is the a priori smoothness length Δ_o.

A_1^1, B_2^1, B_2^2, A_3^0, A_3^1, A_3^2, B_3^3, A_4^1, A_4^3, B_4^4, A_5^1, A_5^2, A_5^4, B_5^1, B_5^4, B_5^5, A_6^3, B_6^3, and B_6^4. "Bad" coefficients are A_3^3, B_3^3, B_4^4, A_5^5, B_5^5, B_6^2, and B_6^5.

Even order harmonics are usually well determined (NA2); they also display a good consistency. Some odd order harmonics show a good consistency, but most "bad" coefficients are odd order harmonics.

7. A Priori Information

A priori information, be it hidden or explicitly expressed, is an essential ingredient in any inversion "cuisine." It enters the procedure in several different ways: we have already made use of some a priori information when introducing shallow layer corrections; the choice of a reference average earth model is also based on information obtained from other data: it is thus to be considered as a priori information for our inversion. Another piece of information that we need to bring in concerns the smoothness of the expected parameter variations in the upper mantle. Additionally, physical constraints can place bounds on the range of possible variations, as well as on the correlation that may exist between some of the parameters.

In Tarantola and Valette's (1982b) inversion method, this kind of a priori information is explicitly introduced through the a priori covariance matrix on the parameters $C_{p_o p_o}$. The next subsections describe the a priori choices we make, and how they are used to build a reasonable a priori covariance matrix.

7.1. Correlation Length

As in section 6, a correlation length Δ_o can be used to describe the smoothness of the expected variations with depth of a given parameter $\underline{p}(r)$. Assuming a Gaussian distribution, the a priori covariance matrix is expressed as

$$C_{p_o p_o}(\underline{p}(r_1),\underline{p}(r_2)) = \sigma_o^2(\underline{p}) \exp\left(-\frac{(r_1-r_2)^2}{2\,\Delta_o^2}\right) \quad (12)$$

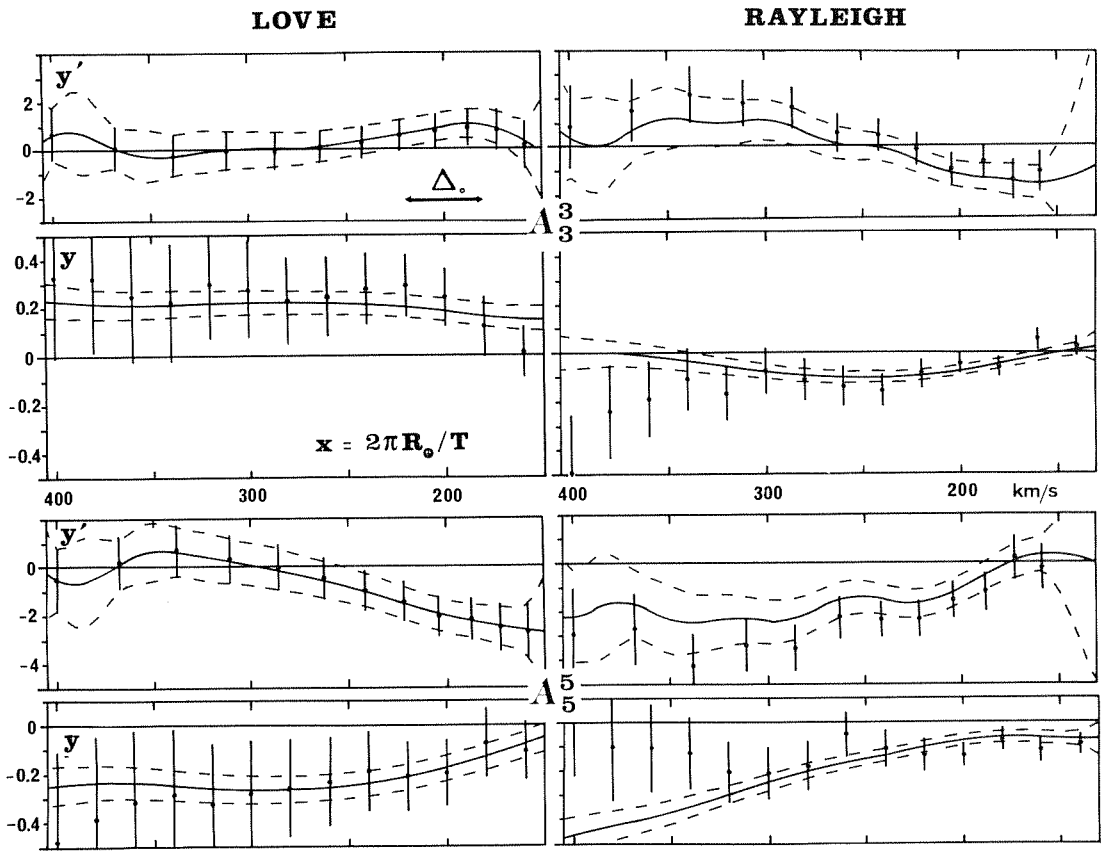

Fig. 5. Two examples of "bad" spherical harmonic coefficients for which phase and group velocities are found to be inconsistent. Other conventions as in Figure 4.

When the distance $|r_1-r_2|$ between two points is small as compared to the correlation length Δ_0, the a priori covariance between the parameters at the two corresponding radii is strong, and they are thus required to vary little with respect to one another in the inversion process. The correlation length Δ_0 controls the smoothness of the variations of the parameters with depth.

Ideally, we would like to choose a correlation length based on physical arguments; for example, from the modeling of convection in the mantle, we expect temperature variations, and hence the seismic velocity variations they produce, to be "smooth" on a scale of some 50-100 km (the thickness of the lithospheric boundary layer). Strong variations can, however, occur on the scale of the minerals that the mantle is made of. Besides the fact that such variations are of little geodynamical interest, they are of course unresolvable by the data set that we are dealing with. This raises the question of the degree of "roughness" that we are able to detect, considering the depth sensitivity of the data we use. Logically, no such concern should be raised at this stage, since depth-resolution is an output of the inversion procedure indeed. However, if we choose too small a correlation length, the answer we get is poorly constrained; we are faced with a long-recognized problem: the trade-off between resolution and precision (Backus and Gilbert, 1970). Two different philosophies are available.

1. On the one hand, "classical" inversion methods (Backus and Gilbert, 1970; Wiggins, 1972) let the data "decide" what roughness they can actually resolve, given their uncertainties. The danger is then that the a posteriori standard deviation for the parameters depends heavily on the shape of the resolution kernels, which is optimized by the inversion procedure but might be very different from a Gaussian distribution and therefore difficult to assess physically (Jackson, 1979).

2. On the other hand, Tarantola and Valette's method includes smoothness as a required a priori ingredient. The a posteriori standard deviation for the parameters then expresses the way that the data constrain the variations of the parameters on the a priori given scale. The danger in that case is that if the a priori scale that we choose is too fine, no significant constraint is brought by the data in the end.

Faced with this dilemma, we are led to "cheat" a little with the logic of Tarantola and Valette's method: the choice we make for the a priori correlation length will take into account the way we expect the data to resolve the parameters with depth. For example, although we have no a priori physical reason to believe that variations are more smooth at 600 km depth than at 100 km depth, we choose a correlation length at depth that is twice the shallow one because we know that our data have a better resolution near the surface than at depth. Figure 6 shows the variation of the a priori correlation length Δ_0 with depth that we finally retain, for both the regionalized and the spherical harmonics inversions, as a reasonable compromise between real a priori information and a guess at the degree of roughness we can constrain from the data.

We should mention that a third way of con-

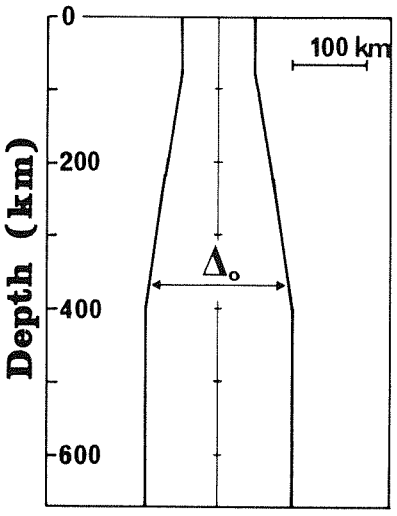

Fig. 6. Plot of the a priori correlation length Δ_o that we choose, as a function of depth. It describes the required smoothness of the models we invert for and enters the inversion procedure through the a priori covariance matrix, as given by expressions (12) and (21).

trolling the variations of the model with depth is to parameterize these variations using a set of functions of depth such as polynomials (Dziewonski and Anderson, 1981) or Legendre polynomials (Woodhouse and Dziewonski, 1984). The inversion is then treated as a classical least squares inversion, the model being overdetermined. The problem with this method is that little natural flexibility is left to the model and that the functions might not be well suited for an optimal resolution to be achieved either. On the other hand, the parameterization makes the computations much lighter and the results easier to communicate.

In fact, we have chosen the latter approach when dealing with lateral heterogeneities as we expanded the data in spherical harmonics using a simple least squares inversion method (NA2), whereas it would have been possible to use Tarantola and Valette's method with some horizontal a priori correlation length (Montagner, 1986). We believe that our mixed approach sets a possible compromise between the freedom that needs to be left to the earth for expressing its heterogeneities and the order that we need to bring in for understanding them.

7.2. Physical Constraints on the Parameters

In this subsection, physical constraints are used to place bonds on the expected variations of the parameters and on the way they correlate. If two parameters $\underline{p}$ and $\underline{q}$ are correlated, their a priori covariance is nonzero. In the $(\underline{p},\underline{q})$ plane the a priori expected variations define an ellipsoidal domain, as sketched in Figure 7. The a priori covariance matrix for these two parameters can be written as

$$C_{p_o p_o} = \begin{pmatrix} \sigma_o^2(\underline{p}) & s\sigma_o(\underline{p})\sigma_o(\underline{q}) \\ s\sigma_o(\underline{p})\sigma_o(\underline{q}) & \sigma_o^2(\underline{q}) \end{pmatrix} \quad (13)$$

The coefficient s governs the degree to which $\underline{p}$ and $\underline{q}$ are correlated. If s = 0, $\underline{p}$ and $\underline{q}$ are uncorrelated; if s = 1, the correlation is complete. For convenience, the correlation can be expressed approximately in terms of an average ratio t so that

$$\frac{\Delta\underline{q}}{\Delta\underline{p}} = t \quad (14)$$

The ratio t corresponds to the slope of the long axis of the ellipse in Figure 7, and s describes the spread away from the t line. If the correlation is strong enough (i.e., (1-s) small enough), expression (13) becomes

$$C_{p_o p_o} = \begin{pmatrix} \sigma_o^2(\underline{p}) & st\,\sigma_o^2(\underline{p}) \\ st\,\sigma_o^2(\underline{p}) & t^2\,\sigma_o^2(\underline{p}) \end{pmatrix} \quad (15)$$

with

$$s = \sqrt{1 - \left(\frac{\sigma_1}{\sigma_p}\right)^2} \quad (16)$$

We note that the parameter s cannot be interpreted in terms of a spread of the ratio t contrary to what was stated by Nataf et al. (1984). In the following, we will try to define the a priori σ_o, t, and s that we need for building a physically reasonable a priori covariance matrix for the parameters ρ, α_H, β_V, ξ, ϕ, and η that we invert for.

Let us examine the factors that induce variations in the model parameters at a given depth: (1) undulations of the seismic discontinuities, be they phase or chemical transitions, produce horizontal variations of density and P and S velocities and, possibly, of the anisotropic parameters, (2) temperature heterogeneities produce variations in density and P and S velocities but have no effect on anisotropy, (3) changes in crystal orientation are responsible for variations of the anisotropic parameters, have some influence on P and S velocities, and have no effect on density.

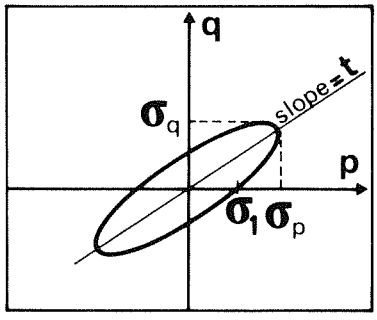

Fig. 7. Schematic drawing of the a priori covariance domain for two correlated parameters **p** and **q**. The slope of the long axis of the ellipse defines an average ratio t. The parameter $s=\sqrt{1-(\sigma_1/\sigma_p)^2}$ describes the spread away from the t correlation line. The case drawn corresponds to t=0.67 and s=0.83.

If convection takes place in the upper mantle, we have reasons to believe that all three factors, undulations, temperature, and orientation, are present and play a role in shaping the earth's lateral heterogeneities. Our goal here, however, is not to test a given convection model but merely to use some reasonable physical constraints to produce rough a priori guesses on the variations of the different parameters. In that spirit, we will assume that variations in density, α_H, and β_V are mostly due to temperature variations alone. We then expect all three factors to decrease when the temperature increases. More precisely, the temperature derivatives of density, α_H, and β_V for olivine are estimated from Kumazawa and Anderson (1969):

$$\frac{1}{\rho}\frac{\partial \rho}{\partial T} = -2.5 \times 10^{-5}\ K^{-1}$$

$$\frac{1}{\alpha_H}\frac{\partial \alpha_H}{\partial T} = -5 \times 10^{-5}\ K^{-1} \qquad (17)$$

$$\frac{1}{\beta_V}\frac{\partial \beta_V}{\partial T} = -5 \times 10^{-5}\ K^{-1}$$

These numbers are not to be taken at face value, as they can vary substantially, depending on the temperature, the chemical composition, and what phases (e.g., olivine, β-phase, γ-spinel) we consider in the upper mantle. What remains, however, is that lateral variations in ρ, α_H, and β_V are expected to be correlated and that the range of plausible variations in these parameters can be bounded if we believe that lateral variations in temperature do not exceed, say, 1200°C. Using this kind of argument, we choose the following a priori constraints:

$$\sigma_o(\beta_V) = 0.2 \text{ km/s}$$

$$\frac{\Delta\rho}{\Delta\beta_V} = 0.3 \frac{g/cm^3}{km/s} \quad \text{and} \quad s = 0.875 \qquad (18)$$

$$\frac{\Delta\alpha_H}{\Delta\beta_V} = 1.5 \quad \text{and} \quad s = 0.92$$

It is worth noting that this kind of a priori constraint also gives a fairly good description of the variations to expect from undulations of the seismic discontinuities.

Changes in crystal orientation are responsible for variations in the anisotropic parameters. In Appendix D the changes in all six inversion parameters are given for a change of the flow from horizontal to vertical in a realistic anisotropic mantle. Although α_H and β_V are found to vary in such a process, we will neglect these variations and consider that only ξ and ϕ vary, neglecting also the variation in η. We will consider that, a priori, changes in the anisotropic parameters ξ and ϕ on the one hand and changes in ρ, α_H, and β_V on the other hand are decoupled, and we choose the following a priori constraints:

$$\sigma_o(\xi) = 0.1$$
$$\frac{\Delta\phi}{\Delta\xi} = -0.5 \quad \text{and} \quad s = 0.875 \qquad (19)$$

We have retained the fact that ϕ and ξ vary in opposite ways for any realistic anisotropic mantle. The rationale for the choice of the numerical factor is based on the variations observed when changing the preferred orientation from horizontal to vertical in a realistic mantle material (Appendix D). The ϕ variation is then in fact larger than the ξ variation. However, as we excluded η from the inversion, we added its effect to the ϕ effect, since ϕ and η correspond to almost identical partial derivatives. The resulting equivalent ϕ variation is then typically half the ξ variation (with opposite sign).

If the 400 km discontinuity, in part, marks the transition from olivine to spinel and orthopyroxene to garnet (majorite), we should expect the mantle below that depth to be more isotropic. Therefore we reduced the a priori $\sigma_o(\xi)$ to 0.05 below 400 km.

In the spherical harmonic inversion, we invert every coefficient with the same a priori constraints. However, as we expect variations for one given coefficient to be smaller than overall variations between regions, we divided the above σ_o by 2 for both β_V and ξ.

7.3. Discontinuities

PREM, and the earth, presumably, shows several seismic discontinuities. The 670-km and the 400-km discontinuities are well known and are presumed to exist everywhere on the globe. PREM also displays discontinuities at 80 km and 220 km. Because of these discontinuities, the partial derivatives G are discontinuous at the corresponding radii. The problem therefore arises of what a priori correlation to choose between the two sides of the boundary. Indeed, on physical grounds we might expect a cold sinking convection current to produce fast seismic velocities on both sides of the boundary if convection passes through; on the other hand, the effect, in terms of the amplitudes of velocity variations, might be different depending on which side of the discontinuity we look at, due to different material properties. We thus expect heterogeneities on both sides to be correlated, but we can allow for a reduction of correlation when crossing a seismic discontinuity. Undulations of the discontinuity would also produce some equivalent loss of correlation across an average discontinuity. Mathematically, if we use equation (12) to build the a priori covariance matrix, the two lines of the matrix corresponding to the two sides of a discontinuity will be identical; $C_{p_o p_o}$ will then be singular, which might lead to some numerical problems in the inversion algebra.

For these reasons, both physical and mathematical, we find it convenient to apply a reduction of correlation across the seismic discontinuities. Equation (12) becomes

$$C_{p_o p_o}[\underline{p}(r_1), \underline{p}(r_2)] = \lambda \sigma_o^2(\underline{p}) \exp\left(-\frac{(r_1 - r_2)^2}{2\Delta_o^2}\right) \qquad (20)$$

where the coefficient λ is 1 when r_1 and r_2 are on the same side of the discontinuity and λ takes some value between 0 and 1 when they are on different sides. In the following, $\lambda = 0.8$ was chosen.

7.4. A Priori Covariance Matrix

Combining the ingredients proposed in the previous subsections we are able to build the complete a priori covariance matrix on the parameters $C_{p_o p_o}$. The general expression for its elements is

$$C_{p_o p_o}[\underline{p}(r_1),\underline{q}(r_2)] = st\,\sigma_o(\underline{p},r_1)\,\sigma_o(\underline{p},r_2)\left[\prod_i \lambda(\mathrm{disc}_i)\right] \times \exp\left(-\frac{(r_1-r_2)^2}{2\,\Delta_o(r_1)\Delta_o(r_2)}\right) \quad (21)$$

where the definitions of the symbols have been presented above, together with the values we choose for them in our inversions.

The a priori covariance matrix for the data $C_{d_o d_o}$ is chosen diagonal and built with the standard deviations obtained from the regionalized or spherical harmonic expansions. It is not strictly valid to consider that all data are independent, especially since we have in fact introduced some correlation between them when combining phase and group velocities. Our simplification is equivalent to giving more weight to the individual data points than they actually deserve. The effect is to exaggerate the required parameter variations, as we show in section 9.

The choice of our a priori covariance matrix can seem rather arbitrary and rigid. It is indeed important to realize that selecting an a priori information is not innocent. Were the model well constrained by the data alone, no such problem would arise, since the information brought in a priori would be overwhelmed by the information brought in by the data. Unfortunately, the phase velocities of fundamental mode Love and Rayleigh waves do not carry enough information to constrain fully the variations with depth of the six parameters of a transversely isotropic upper mantle. Faced with this reality, one might be tempted to ignore some of the parameters altogether. For example, one could assume isotropy and invert for ρ, α, and β only, or even for β, the dominant parameter, alone. We think that such an a priori choice is no longer physically reasonable and that the apparent confidence that it brings can be misleading. We prefer building a seemingly more complicated a priori cuisine that rests upon more reasonable physical assumptions while permitting some flexibility for violating them. Our results, of course, will depend on the choice we make for the a priori information, as a few examples will show in section 10. The reader should refer to our final results as, at most, being the best that we can extract from our data with our present knowledge.

8. Resolution and Trade-Off

Before getting to the earth's models that we obtain by inversion, it is necessary to examine what resolution we have from the data that we use. As we invert for five different parameters (ρ, α_H, β_V, ξ, ϕ), resolution also includes the trade-off between parameters. The resolution function R given by equation (7) tells us what kind of resolving power as a function of depth we have for a given parameter and also what "leakage" from other parameters comes in.

Figure 8 shows the generalized resolution functions for the inversion of the B_2^2 spherical harmonic coefficient. We show only one set of resolution functions; they are almost identical for all the spherical harmonic coefficients and are rather similar to the ones obtained for the inversion of the different regions. The resolution is plotted at selected depths for the five parameters. Each resolution line comprises one segment that is the usual "resolution function" or "averaging kernel" and four other segments that describe the trade-off with the other parameters. Ideally, we would like to obtain a delta function centered on the target depth (marked by an arrow) and zero trade-off with the other parameters.

It is important to realize that if the usual depth resolution is dimensionless, this is no longer true for the trade-off between parameters. The problem then arises of how to compare parameters that are of different physical nature. It seems reasonable to relate each parameter to some natural scale (Jordan, 1973). It is easy to show that if one uses a scale u_i to define dimensionless parameters $\underline{\ddot{p}}_i = \underline{p}_i/u_i$, then the dimensionless resolution function $\ddot{R}$ for these new parameters is given by

$$\ddot{R}[\underline{\ddot{p}}_i(r_m),\underline{\ddot{p}}_j(r_n)] = \frac{u_j(r_n)}{u_i(r_m)}\,R[\underline{p}_i(r_m),\underline{p}_j(r_n)] \quad (22)$$

The amplitude of the trade-off between two parameters depends on the scale chosen. The most natural choice is to pick the a priori standard deviation σ_{oi} as a scale for each parameter $\underline{p}_i$, as they have been defined precisely so as to bracket the physically plausible variations of the parameters. The larger is σ_{oi} for a parameter $\underline{p}_i$, the larger are the variations that we expect for the latter, and through equation (22), the smaller is the trade-off of the other parameters with it.

We now examine the sets of resolution/trade-off plots of Figure 8. As expected, the two best resolved parameters are β_V and ξ. Typical values for the width at midheight of the β_V resolution kernels are 150 km at 200 km depth, and 250 km at 400 km depth. Similar values have been obtained for inversions of data in the same period range (e.g., Lévêque, 1980). However, we also note a significant trade-off with ϕ (P anisotropy). This, of course, comes from the almost perfect identity of shape between the β_V and ϕ partial derivatives for Rayleigh waves as discussed in section 4. The ξ resolution kernels are not well behaved for depths shallower than about 160 km; for these depths there is also a significant trade-off with shallow β_V structure. The ξ resolution kernels are rather wide: about 250 km at 200 km depth, and 350 km at 400 km depth. We note that α_H is completely unresolved in our inversions.

In conclusion, we can get a fair resolution of β_V variations throughout most of the upper man-

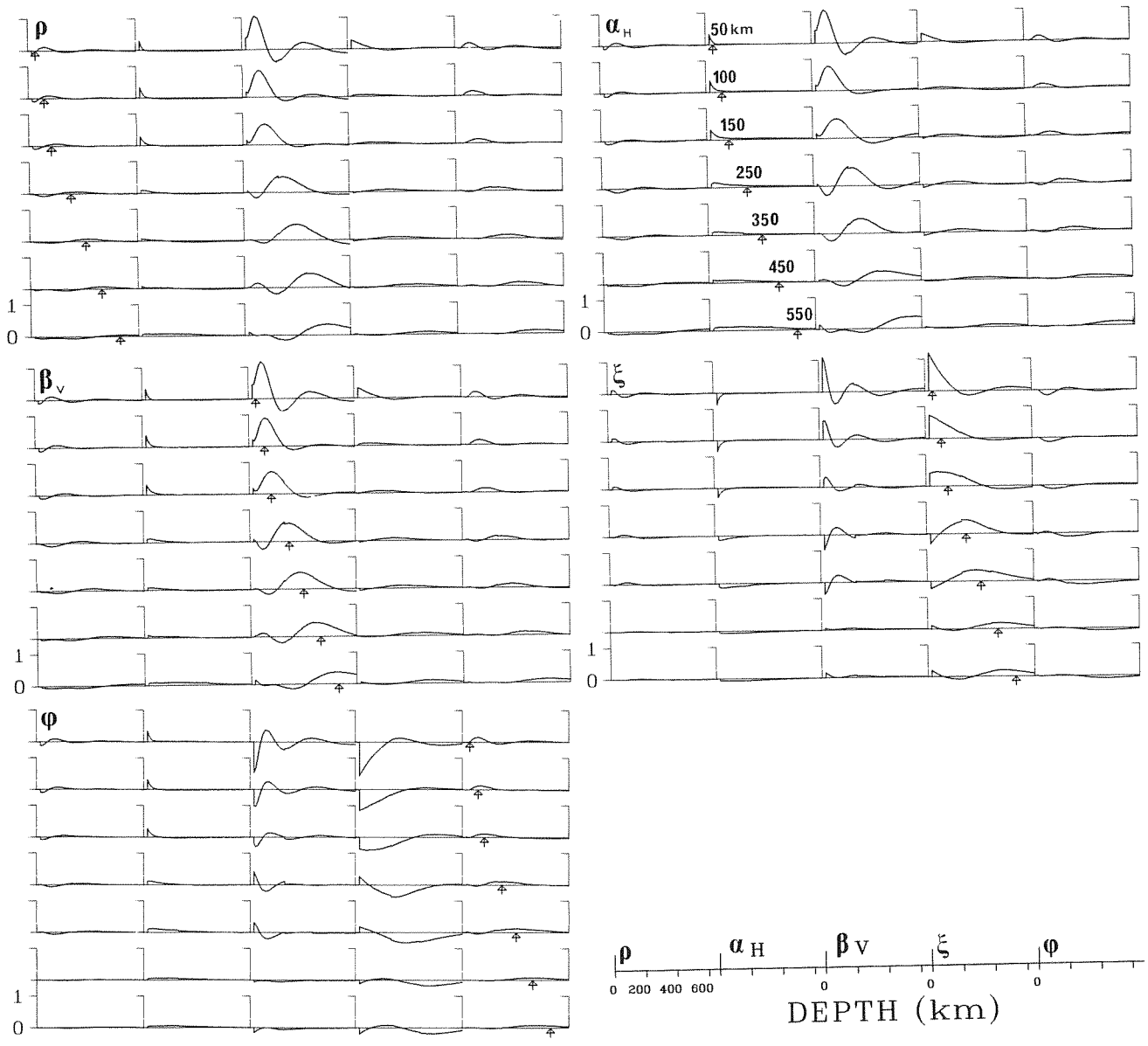

Fig. 8. Resolution/trade-off functions for the B_2^2 coefficient. Each line is the line of the resolution function that corresponds to the tested parameter at the tested depth (marked by an arrow). Units are 10^{-3} km^{-1}. Each of the five segments spans the upper mantle. Each segment corresponds to a different parameter. Every parameter is normalized with its a priori standard deviation σ_o. Note that β_V and ξ are the best resolved parameters.

tle. S anisotropy is not as well resolved, but we should get reliable estimates of ξ variations averaged between 200 and 400 km depth. Shallow S anisotropy might be contaminated by β_V variations. The other parameters (ρ, α_H, and ϕ) that we invert for will be mostly controlled by the a priori information that links them to β_V and ξ.

9. Regional Inversion

In this section we present the models we obtain for the seven tectonic regions of Okal's regionalization shown in Figure 1 and discuss their implications. We examine the fits and the standard deviations of the models and design a few tests to assess how reliable our models are. Our results corroborate some now well-established features, such as the thickening of a fast lithospheric lid with age in the oceans, and the presence of a fast mantle under shields. The trench, or convergence, region has a distinct signature. Anisotropy indicates horizontal flow under the oceans except for the youngest and oldest parts where the flow is vertical.

9.1. Regionalized Models

Figures 9 and 10 show the structure of the upper mantle for the four oceanic regions (A, B, C, D). Figures 11 and 12 show the results obtained for the three other regions (T, M, S). In Figures 9 and 11 we plot the differences from the

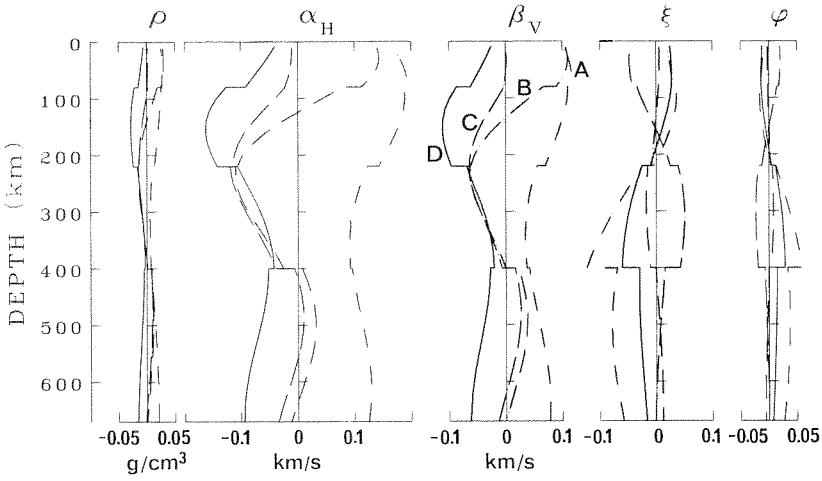

Fig. 9. Final oceanic models (regions A, B, C, and D). We plot the deviations, from the a priori model, of the five parameters we invert for, as a function of depth in the upper mantle. Below 80 km, the a priori model is PREM for all regions. Note the evolution of the β_V structure with the age of the seafloor in the first 200 km.

corresponding a priori models. Below 80 km, the a priori model is PREM for all regions. Between 80 km and the base of the crust, the α_H and β_V structure of the a priori models varies depending on the P_n value chosen for the corresponding region. In Figures 10 and 12 the absolute values are plotted (for a 1-s period seismic wave reference).

The β_V structures of the four oceanic regions indicate a correlation with the age of the ocean floor. Region D, the youngest region (0-30 Ma), has lower than average velocities throughout the upper mantle. The velocity is especially low between 80 and 250 km depth. The velocity in the upper 220 km increases gently with age from region D to region C (30-80 Ma) to region B (80-135 Ma) and increases even more to region A (more than 135 Ma). Except for the latter, the oceanic regions display the same lower-than-average velocity between 200 km and 400 km. As discussed below, many of these features have already been described in regional or global studies of the oceanic mantle. We also note that at depths greater than 400 km, the youngest ocean (D) is slow, whereas the oldest region (A) is fast. For ages from 30 to 135 Ma, we find no significant variations at these depths.

The evolution of S anisotropy (ξ) with age is not as obvious. If we focus on the slice between 200 and 400 km depth, where resolution is best, we find that the two extreme regions (D and A) have a significant negative $\Delta\xi$ signature. As shown in Appendix D, a negative $\Delta\xi$, i.e., a less than unity ξ, i.e., SV>SH, is diagnostic of vertical flow for any realistic olivine-rich material. In both regions we could be seeing a vertical mantle flow. Region C (30-80 Ma), on the contrary, has a significant SH > SV signature (i.e., horizontal flow), while region B (80-135 Ma) shows almost no anisotropy beyond that of the reference model PREM.

The region of trenches and marginal seas (T) has a peculiar β_V signature: low velocity in the upper 300 km and high velocity below that depth. One interpretation is that we are seeing the slow mantle associated with marginal seas and island

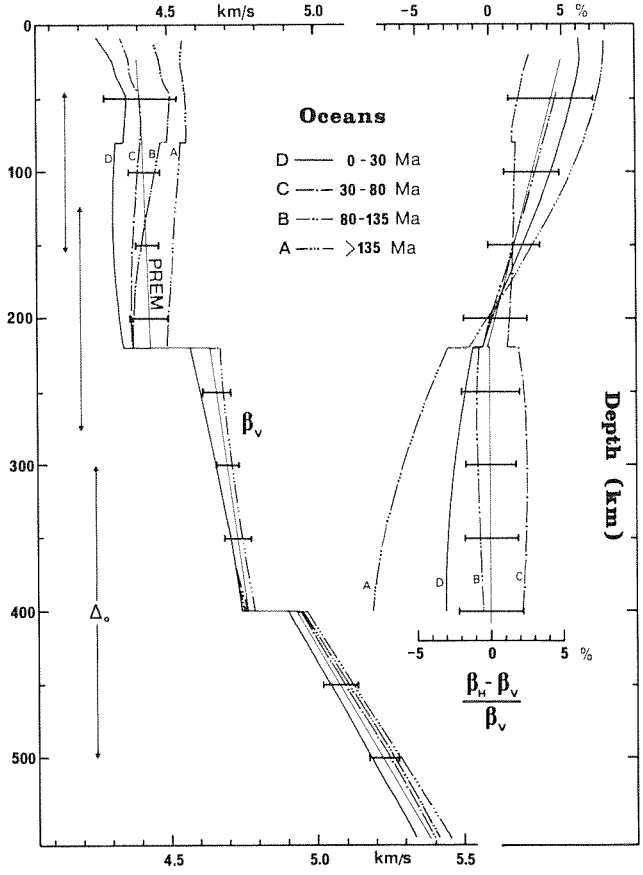

Fig. 10. Final oceanic models. Absolute β_V and S anisotropy values as a function of depth. The reference period is 1 s. The solid line is PREM, and the horizontal bars attached are our 2σ a posteriori standard deviations. The vertical bars are the a priori correlation length Δ_o at selected depths. The scale for S anisotropy ((SH-SV)/SV) has been chosen so that the velocity variations that it describes are comparable to the β_V variations. For region A the model obtained from the third iteration is plotted.

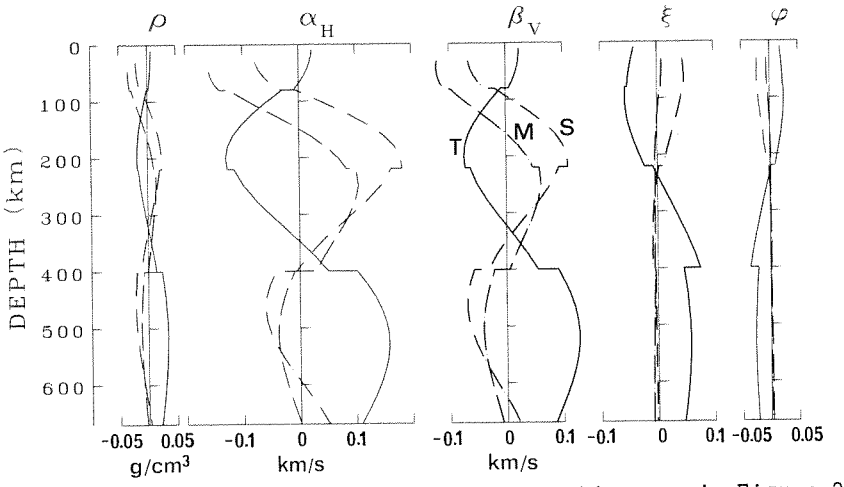

Fig. 11. Final models for regions T, M, and S. Conventions as in Figure 9. Note the large fast β_V anomaly at depth for the trench region. Also note that the continental regions (S and M) require no anisotropy below 200 km.

arc volcanism at shallow depth and cold subducted oceanic lithosphere at larger depths. There is a significant SH>SV anisotropy below 200 km in that region and about 2.5% SV>SH anisotropy at shallower depths, consistent with vertical flow.

The shield region (S) is characterized by fast mantle down to 300 km, with a tendency toward a slow mantle below 400 km depth. There is almost no anisotropy, except in the upper 200 km where an SH>SV anisotropy is detected. The mountainous region (M) requires no anisotropy. Its β_V structure indicates a slow uppermost mantle, with a somewhat fast zone between 200 and 400 km. Before discussing in more detail the implications of our results, we present a few elements that help assess their reliability.

9.2. Fits to the Data

Figures 13 and 14 show the fits that our final models give to the regionalized data. For each of the seven regions, we display, for both Love and Rayleigh waves, the data (from NA1), the fit given by the starting model, and the fit obtained from the final model, all referenced to the corresponding PREM values. The original C(T) data have been transformed to T(n) data by interpolating the phase velocities to integer n values. The differences from PREM are plotted as period differences $\Delta T(n)$ for given mode numbers n. Differences in terms of phase velocity variation $\Delta C(T)$ at a given period T can be deduced using the classical formula:

$$\left(\frac{\Delta C}{C}\right)_T = -\frac{C}{U}\left(\frac{\Delta T}{T}\right)_n \qquad (23)$$

where C, U (the group velocity), and T can be taken as the PREM reference values listed by Dziewonski and Anderson (1981) for the chosen mode numbers n.

We observe that for all regions we obtain a good fit of both Love and Rayleigh waves data. Our models are too stiff to fit some of the wiggles in the data, but these are probably artifacts of the data retrieval. We also note that the data at the longest period (330 s) are not satisfied by our models in some regions. At these periods the traveling wave approach starts to break down so that the data might be biased (NA1).

It is interesting to note the importance of the crustal corrections when examining heterogeneities in the mantle. For example, comparing

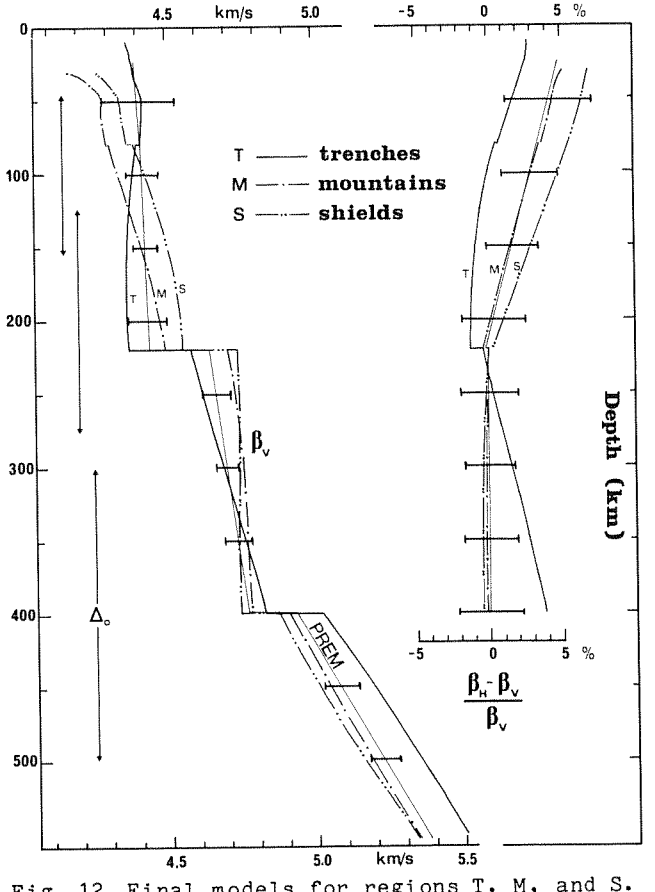

Fig. 12. Final models for regions T, M, and S. Absolute β_V and S anisotropy values. Conventions as in Figure 10.

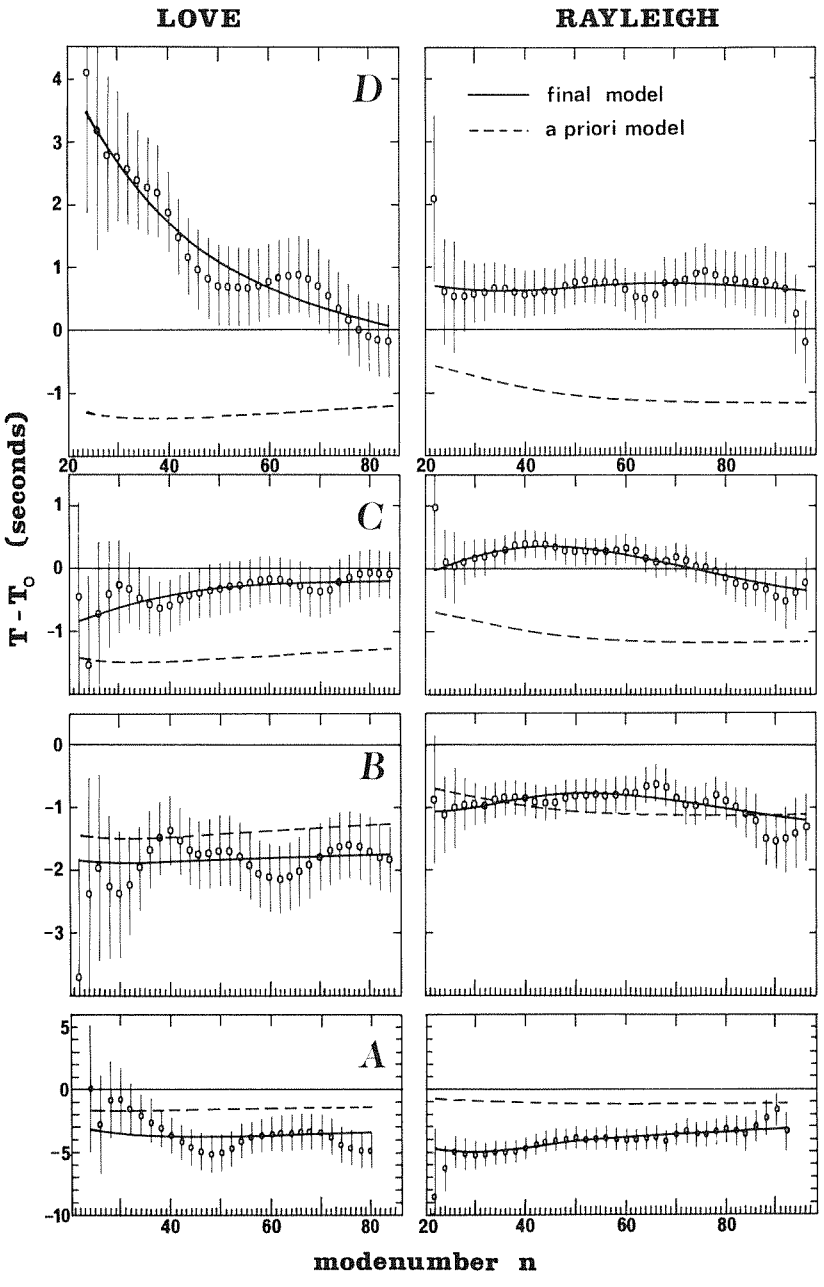

Fig. 13. Fits to the data for the oceanic regions. For each region, the periods for Love (left) and Rayleigh (right) waves are plotted with their 2σ error bars against the mode number n. The solid line is the fit given by our final model; the dashed line is for the a priori model. All values are differences from the corresponding PREM values.

data from region D (young ocean) and region S (shields), we find that at short periods both are very close to the average. However, when we compare them to the values given by their respective a priori models, which include realistic crustal structures, we observe that there exists a substancial difference. This difference of about 2 s must be accounted for by heterogeneities in the mantle, which explains why we find a slow lithospheric mantle for young oceans and a fast one under shields.

Finally, we note that our models, which include anisotropy, have no problem in fitting Love and Rayleigh wave data simultaneously. This by itself does not mean that anisotropy is in fact required for explaining the data. However, we show in the next subsection that for some regions the anisotropy found in the model is above the noise level given by its a posteriori standard deviation, meaning that anisotropy is indeed necessary to explain the data, given the choice of a priori information.

9.3. A Posteriori Standard Deviations

The diagonal terms of the a posteriori covariance matrix given in expression (6) are the squares of the a posteriori standard deviations

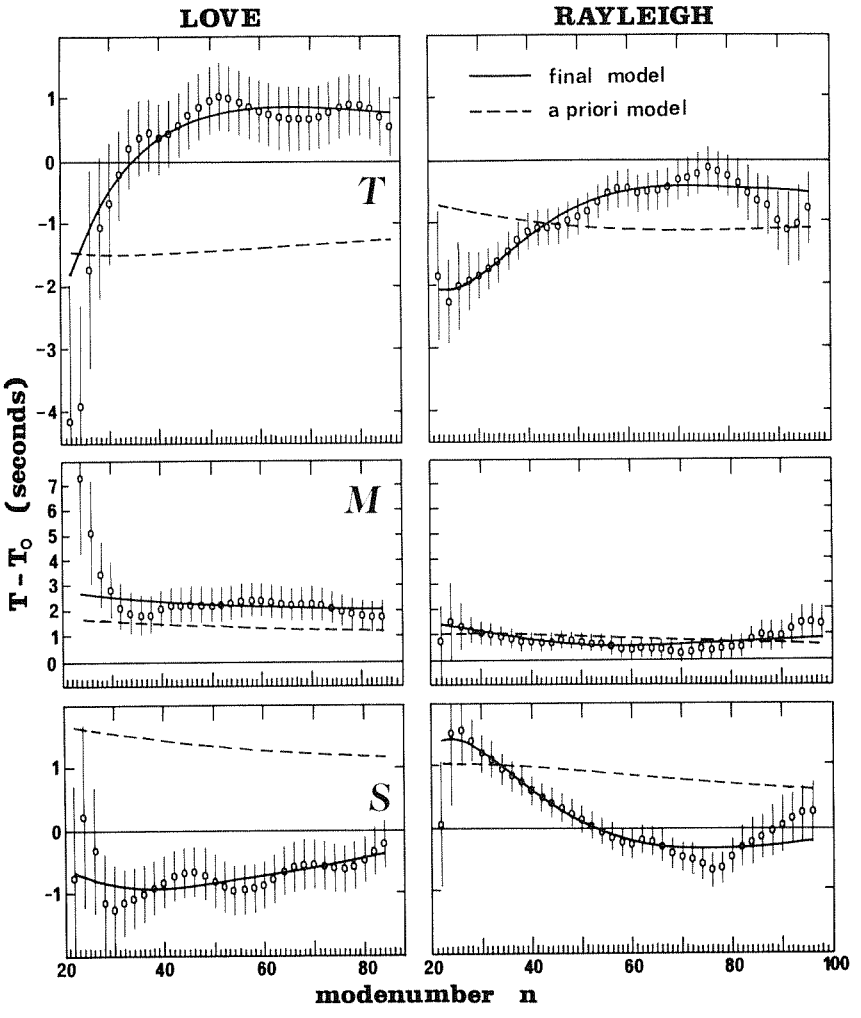

Fig. 14. Same as Figure 13 for the T, M, and S regions.

of the parameters. They describe how well constrained are the features displayed by the models produced by the inversion. Figure 15 is a plot of the a posteriori standard deviations for all five parameters as a function of depth for two regions: region A and region C. As can be seen from the proportion of the total surface of the earth that they occupy (see Appendix A), these two regions represent two extremes: the best constrained region (C) and the worst one (A). All other regions lie in between. We define a variance reduction V_R by

$$V_R = 1 - \frac{\sigma_{\hat{p}}^2}{\sigma_o^2} \qquad (24)$$

where $\sigma_{\hat{p}}$ and σ_o are the a posteriori and a priori standard deviations, respectively. The maximum variance reductions we obtain are 97% for β_V, 88% for ξ, 85% for a_H, 78% for ρ, and 77% for ϕ. As we had deduced from the resolution plots, β_V and ξ appear to be the best constrained parameters. If we now compare the a posteriori standard deviation plots to the actual variations displayed in the models, we find that the variations in the density ρ and in the P anisotropy ϕ practically all lie within the error bars and are thus unconstrained. Their variation merely reflects the variations of the other parameters, which are constrained, to which they are a priori linked. One exception is the high-density zone below 400 km found for the trench region. Another one is the PV>PH anisotropy required below 200 km for region A (old ocean).

For β_V, most variations between 80 km and 400 km are really constrained features. Below 400 km, only the very high velocity of the trench region and the somewhat low velocity of the shield region are above the noise level. Although the four oceanic regions do seem to show a nice evolution with age at these depths, we cannot assert it with any confidence. All β_V variations above 80 km are not well constrained.

SH>SV anisotropy (i.e., horizontal flow) is required between 200 km and 400 km depth for the C region (ocean, 30-80 Ma) and for the trench region, whereas the D region (youngest ocean) and the A region (oldest ocean) require SV>SH anisotropy (i.e., vertical flow) at these depths. Regions A and T seem to require anisotropy below 400 km, even though we have a priori almost rejected this possibility by setting a small a priori standard deviation. However, these two regions might be affected by instabilities in the regionalization process: region A covers a small

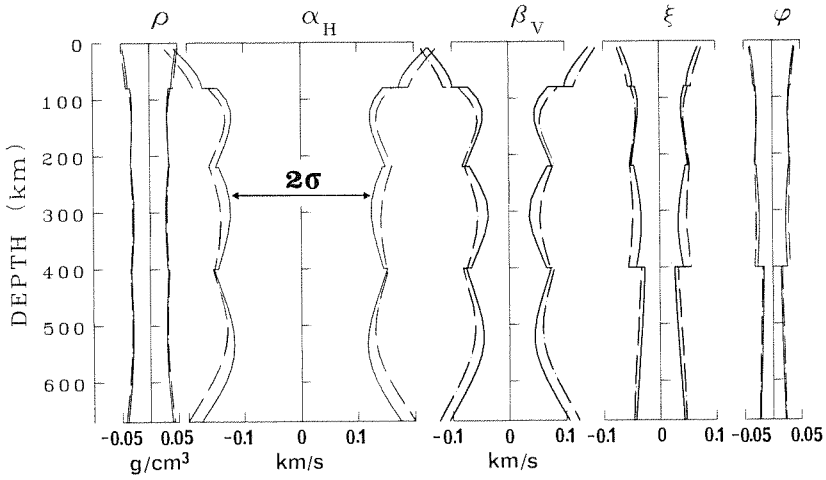

Fig. 15. A posteriori standard deviations for the best resolved (C, solid line) and the worst resolved (A, dashed line) regions.

proportion of the earth's surface, and region T has a rather heterogeneous topography (see Appendix A).

9.4. Convergence

We have seen that for a nonlinear inverse problem, we must iterate expression (5) to obtain the final converged model. Luckily, the inversion of surface waves phase velocities is not very nonlinear, and only a few iterations are needed. A sufficient convergence is usually achieved after only one iteration (k=1 in expression (5)). All models and fits presented in the previous subsections were the results of the second iteration (k=2), except for region A. Here we show how convergence is reached for region A by displaying the models (Figure 16) and the fits (Figure 17) obtained for k=0,1,2,3. The data for region A are rather far from the average, so that it takes one more iteration for this model to stabilize. For the other regions, the k=2 models are close enough to the final converged models for our purposes.

9.5. Test on Data Independency

All the data points that we invert are not really independent; the phase velocity that we measure at a period T is in fact an average over some period range, which might overlap with the neighboring measurement. Ideally, we should evaluate this overlap and build an a priori covariance matrix on the data $C_{d_o d_o}$ accordingly. However, we neglected such interactions in our inversion and considered all data to be independent. This simplifiction might be unjustified (N. Jobert, personal communication, 1983). In order to test the influence of data selection, we ran a case where only every fifth data point is taken and assumed independency again. Region M was chosen. Figure 18 shows the models obtained from the inversions of the complete data set and the reduced data set. Figure 19 shows the associated fits. Although the two fits look almost as good with respect to the complete data set, the two models show some substantial differences. Anisotropy is unaffected, but the β_V structure is somewhat changed. As could be expected, the inversion

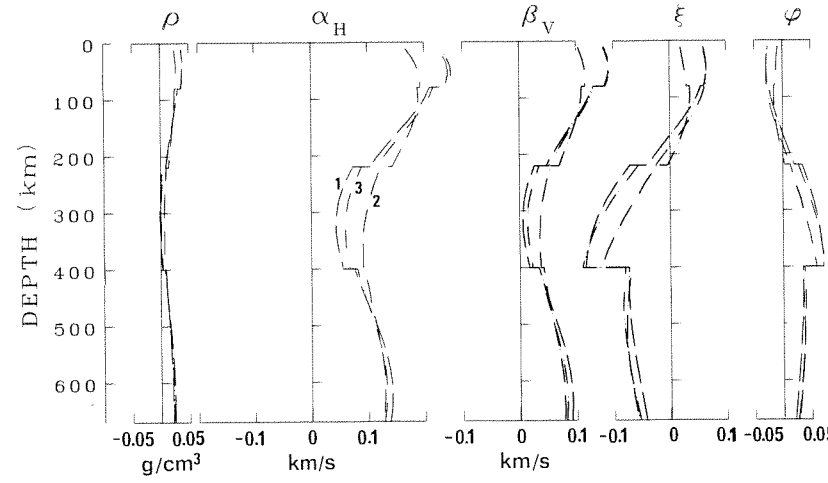

Fig. 16. Convergence of the iterative inversion: the models for region A. The models obtained for the first, second, and third iterations are drawn. Other conventions as in Figure 9.

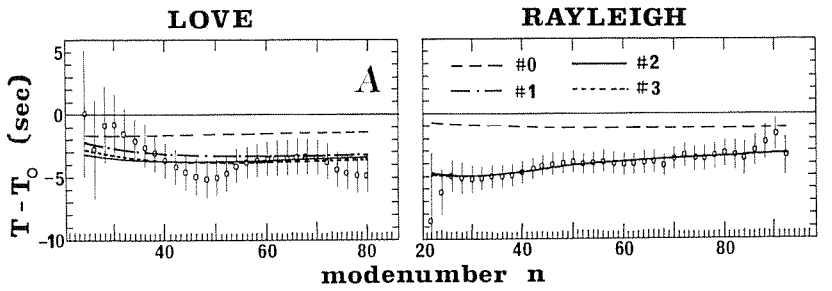

Fig. 17. Convergence of the iterative inversion: the fits for region A. The fits to the data obtained for the first, second, and third iterations are drawn. Other conventions as in Figure 13.

of the reduced data set yields smaller overall amplitudes. Nevertheless, the pattern of variations with depth remains almost unchanged. This problem, together with the influence of the choice for the a priori correlation length on the parameters, Δ_o, is here to remind us that great care must be observed when interpreting the results of surface wave inversions.

9.6. Group Velocities

Although we did not measure group velocities for the different tectonic regions, it is interesting to calculate them for our models in order to compare them to previous or future observations. Figures 20 and 21 show the group velocities that we calculate for Love and Rayleigh waves from the models of our seven regions.

9.7. Discussion

Before the discovery of plate tectonics, surface waves had been used to demonstrate the difference in mantle structure between oceans and continents (Dorman et al., 1960; Brune and Dorman, 1963). After the discovery of seafloor spreading, there were many investigations of the oceanic upper mantle. In fact, seismology would soon bring supporting evidence to the new concept.

9.7.1. Oceans. Many studies, both regional and global, demonstrate the systematic evolution of the oceanic uppermost mantle with the age of the seafloor. In a detailed study of surface waves dispersion in the Nazca plate, Forsyth (1975) showed the existence of a fast lithospheric lid, whose thickness increases with age. A pronounced low-velocity zone was observed in the youngest parts of the ocean (Wu, 1972). A very similar behavior was discovered in the Pacific plate by Mitchell and Yu (1980). The thickness of the lid increases from about 30 km for a 5 Ma ocean to 50 km for 40 Ma, 90 km for 80 Ma, and 120 km for the oldest ocean. These findings supported convective models of seafloor spreading, which required the thickening of a cold oceanic lithosphere with age or, equivalently, the cooling and growth of a thermal boundary layer (Turcotte and Oxburgh, 1967; McKenzie, 1967). The data that we use do not provide enough resolution to follow accurately the thickening of the lid with age. However, our models show quite a systematic increase with age of the lid thickness and of the velocity in the first 200 km. The difference in velocity (0.2 km/s) is not unreasonably different from what a thermal model of the lithosphere would produce.

With the installation of long-period digital seismographs, it became possible to go one step further and investigate heterogeneities below the lithosphere. One question was in the air and needed an answer: do ridges have deep hot roots

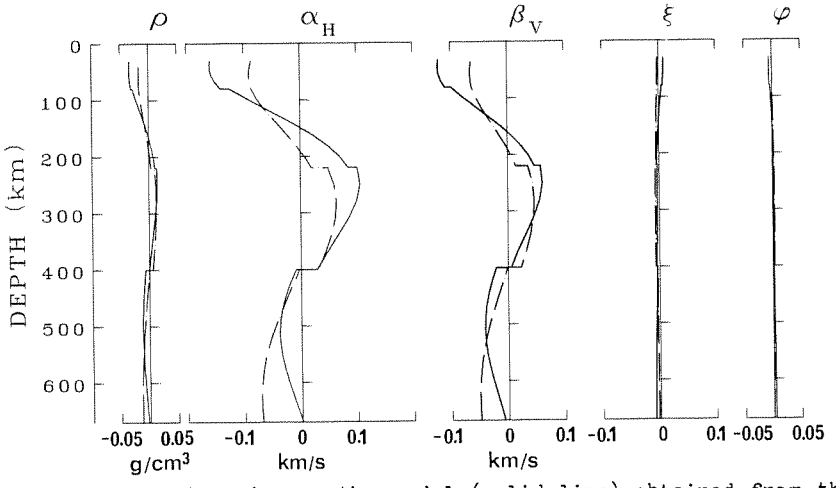

Fig. 18. Test on data independency: the model (solid line) obtained from the inversion of the complete data set is compared to the model (dashed line) obtained using a reduced data set for region M. Other conventions as in Figure 9.

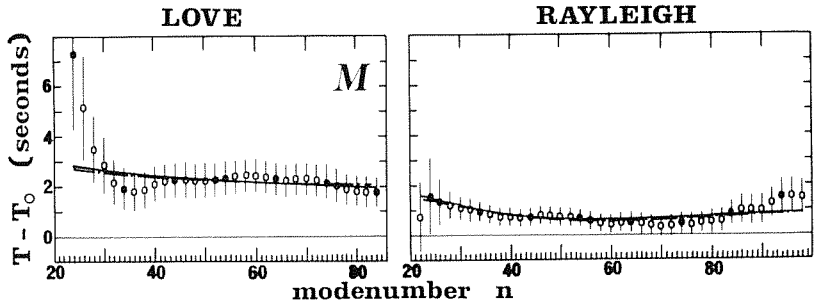

Fig. 19. Test on data independency: the fits obtained for the two models of Figure 18. The solid data points form the data subset that was inverted to obtain the second model. Other conventions as in Figure 13.

or are they merely surface features produced by the pulling apart of the oceanic plates? Comparisons of deep structures in the oceans were performed from regional and global studies. Lévêque (1980), Wielandt and Knopoff (1982), and Montagner and Jobert (1983) find old oceans to be faster than young oceans down to at least 500 km. Nakanishi (1981) found no significant difference between young and old oceans below 300 km. Dziewonski and Steim (1982), using waveform inversion, inferred the existence of substantial shear velocity differences (0.2 km/s) between young and old oceans for depths from 400 km to 670 km. In our models, old oceans are faster than young oceans by about 0.1 km/s at the same depths, but we have seen that the a posteriori standard deviation was about as large. In summary, shear velocity data seem to indicate that ridges are slower than old oceans throughout the entire upper mantle. It is then tempting to conclude that ridges have a deep hot root. However, we will see that the S anisotropy results suggest an alternative hypothesis.

From Forsyth's (1975) study it became evident that anisotropy could play an important role in the dispersion of oceanic surface waves. Indeed, his models for the Nazca plate display a 3.5% SH>SV anisotropy in the first 120 km and possibly a 3% SV>SH anisotropy from 120 to 400 km. Mitchell and Yu (1980) also advocate an SH>SV anisotropy of about 2.5% in the lid for old ocean but could not resolve deeper anisotropy. All these studies considered only S anisotropy. Anderson and Regan (1983) pointed out that by also considering P wave anisotropy, it was possible to build oceanic models that were rather different from the previous ones but that fitted the data as well. Their models are characterized by a very thin lid (45 km at 80 Ma) above an anisotropic low-velocity zone with SH>SV at most ages. Using very long-period data, Schlue and Knopoff (1977) and Journet and Jobert (1982) have a better resolution below the lid and also find SH>SV. Journet and Jobert note that this anisotropy increases with age in the first 150 km of the mantle. In the Pacific, Montagner (1985) confirms this trend and finds that for young oceans, one could even have SV>SH in the upper 150 km.

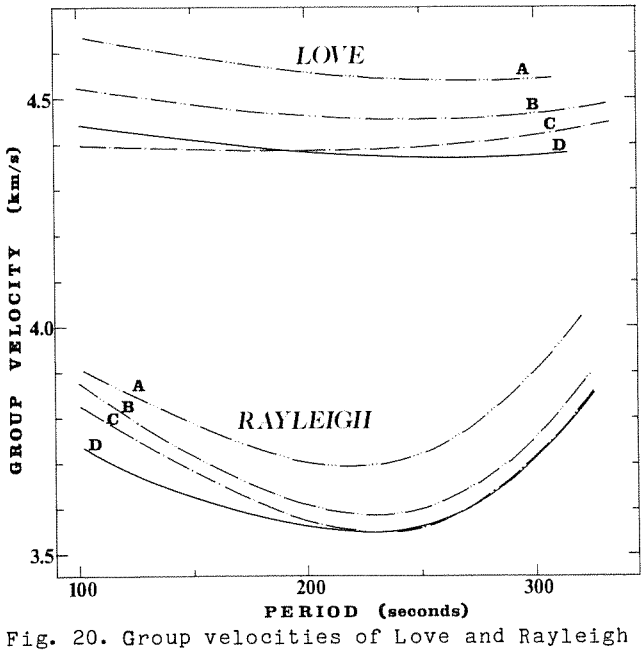

Fig. 20. Group velocities of Love and Rayleigh waves calculated from our models for the oceanic regions.

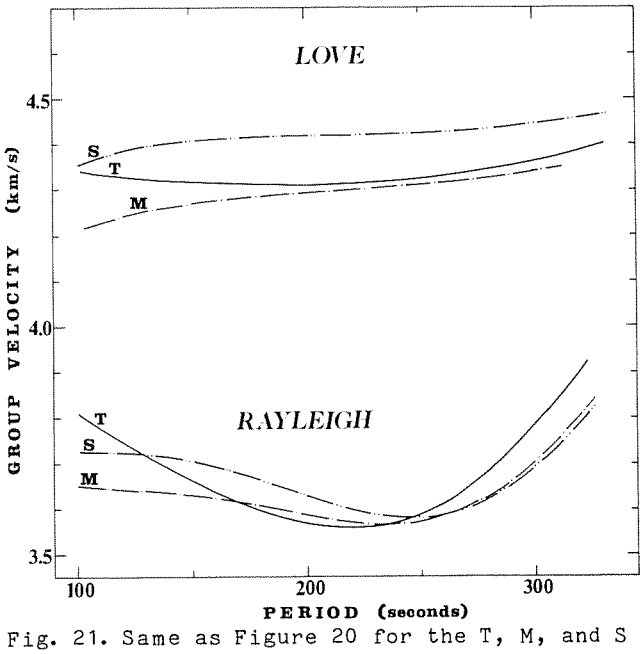

Fig. 21. Same as Figure 20 for the T, M, and S regions.

Our analysis shows that when using very long period Love and Rayleigh waves, it is difficult to resolve anisotropy above 200 km because of S velocity contamination. Below 200 km, we must remain cautious about the validity of the results. Nevertheless, our results seem to indicate that young oceans (region D) have SV>SH (vertical flow). For older oceans (region C) the anisotropy corresponds to horizontal flow (SH>SV), but this anisotropy is progressively replaced by SV>SH anisotropy again when the age of the ocean increases (region B and region A).

Together with the shear velocity results, this behavior suggests a possible scenario: as the plates move apart, hot material is advected up at ridges; shear velocities are slow down to 200 km, and the flow is vertical (region D). Then the material turns around, and the flow becomes horizontal (SH>SV) and the lithosphere thickens (region C). When the oceanic lithosphere is old enough, thermal boundary layer instabilities develop at its base (Parsons and McKenzie, 1978; Jaupart and Parsons, 1985), and cold blobs detach and founder into the mantle (Houseman and McKenzie, 1982; Fleitout and Yuen, 1984). These cold blobs create a dominantly vertical flow beneath the lithosphere (regions B and A) and advect cold material to increasingly larger depths. The shear velocity differences between young and old oceans below 300 km could then result from the fact that blobs are inhibited under the ridges while abundant under old oceans (Houseman, 1983) rather than being due to the presence of an active deep hot rising current under the ridge.

9.7.2. Trenches and marginal seas. The trench region (T) is remarkable by its deep and very fast signature. This peculiarity already mentioned by Nakanishi (1981) can be seen as observational evidence for cold subducted lithosphere. A major element of the dynamics of plate convection is thus detected. Above 300 km, the cold subducted slab is not seen: it is presumably hidden by the presence of hot material associated with volcanism and marginal seas, two phenomena that often accompany subduction. Anisotropy seems to indicate a vertical flow between 100 and 200 km and a horizontal flow from 200 to 400 km, a somewhat counterintuitive result.

9.7.3. Continents. Shields have long been known to be underlain by a thick cold lithosphere (Brune and Dorman, 1963). In our models they are characterized by fast velocities from 80 km to about 300 km. Above 80 km, the lower-than-average velocity displayed by our model is not a significant resolvable feature. Below about 350 km, shields seem to be slower than the average earth (and than the oldest oceans). We find no evidence for the "tectosphere" advocated by Jordan (1975), although shields on average are indeed faster than most oceanic regions, but not the oldest oceans, down to 400 km. The mountainous region (M) is very similar to the shield region except in the top 200 km, where it is slower, in agreement with Nakanishi's (1981) findings. We note that our M region taken from Okal (1977) comprises regions as different as the East African rift and the Himalayan belt. The two continental regions seem to require no anisotropy between 200 and 400 km.

The regionalized approach serves to constrain better the structure of mantle convection on the scale of the tectonic plates. It has the drawback, however, of hiding possible smaller-scale features and to unduely distribute possible very large scale features. In the next sections, we will show that the spherical harmonic approach nicely confirms some of the regionalized results but also permits us to go one step beyond.

10. Inversion for Spherical Harmonic Coefficients

In this section, we present the variations with depth of the five parameters (ρ, α_H, β_V, ξ, ϕ), in the case of a few selected spherical harmonic coefficients. Of course, to get an image of the real earth, one has to combine all the coefficients, as we do in the next section. However, some coefficients are better constrained than others in our inversion, and it is useful to examine a few coefficients individually. The results are given for all the coefficients at selected depths in Table 1 for β_V and in Table 2 for ξ. We also give some elements that help assess the reliability of our results (standard deviations, fits to the data, and a few other tests).

10.1. Models

The B_2^2 coefficient is of special interest: it is a well-constrained coefficient, and it describes most of the degree 2 variations. Our inversion results for that coefficient are shown in Figure 22. At 370 km depth it has the largest β_V variation of all coefficients (-0.021 km/s). The associated S anisotropy is not very large (less than 1%). Below 400 km, no significant β_V anomaly is required, although α_H remains negative throughout the upper mantle. Figure 23 gives the results for the A_3^3 coefficient. As we have seen in section 6, it is a "bad" coefficient, in the sense that phase and group velocities seem to be incompatible. The results are a hesitating β_V variation and a strong S anisotropy (-1.5%) between 200 and 400 km depth. It has, in fact, the largest S anisotropy of all the coefficients at 280 km depth. This raises an important point: S anisotropy appears to be rather sensitive to "defects" in the data. This is not unexpected: if Love or Rayleigh waves data are erroneous, the inversion tends to produce a nonphysical model that complies as best as possible to both data sets, thereby producing spurious large anisotropy variations. As a consequence, among the 12 coefficients that are above the noise level (given by the a posteriori standard deviation) at 280 km depth, there are as many "bad" coefficients (five) as "good" ones (five). Anisotropy is difficult to resolve, and we have to keep that problem in mind when analyzing the maps obtained by recombining the coefficients. The situation is not as serious for β_V variations: at 100 km depth from the 12 coefficients above the noise level, 2 are "bad," whereas 9 are "good"; 1 "bad" versus 5 "good" at 250 km depth; and no "bad" coefficient among the five coefficients above the noise level at 340 km depth.

Figure 24 shows our A_5^4 model. Although it is an odd order spherical harmonic coefficient, it is well constrained in the expansion and has compatible phase and group velocities. At 100 km

TABLE 1. Spherical Harmonic Coefficients A_{lm} and B_{lm} for β_V at Selected Depths

	Depth, km										
	47	80-	80+	160	220-	220+	310	400-	400+	533	670-
A10	17.1	14.5	10.8	0.3	-0.9	3.8	10.0	10.5	7.9	-7.0	-22.6
A11	20.5	23.1	29.4	23.9	16.0	3.5	1.3	4.9	17.4	15.8	2.0
B11	-24.8	-20.6	-18.9	10.2	20.4	20.6	10.4	-1.7	-8.0	-1.7	19.2
A20	-3.2	-2.3	-4.2	6.1	11.6	21.2	17.3	6.4	-8.7	-16.0	-6.4
A21	-54.2	-43.5	-22.7	12.7	20.0	-3.2	-10.9	-12.8	5.4	15.2	18.5
B21	-30.3	-24.5	-14.3	9.7	17.3	5.7	3.7	1.2	11.7	11.3	7.2
A22	16.7	17.3	19.2	11.4	3.5	-7.6	-10.1	-3.0	10.2	21.2	18.3
B22	-47.1	-39.3	-19.4	-3.0	-1.2	-22.3	-22.9	-19.7	1.2	-1.7	-16.5
A30	5.3	8.3	12.7	15.1	8.1	-6.1	-17.7	-17.9	-7.4	7.0	17.2
A31	-19.6	-14.5	-10.0	15.4	20.6	12.7	-0.3	-9.7	-8.7	1.7	21.0
B31	2.3	2.6	5.2	-1.0	-5.5	-11.1	-10.7	-5.8	1.2	4.9	0.9
A32	-33.0	-28.6	-28.7	7.5	21.0	24.9	11.9	-3.2	-15.1	-2.0	31.9
B32	46.2	41.2	38.4	0.8	-12.6	-11.4	2.4	16.7	23.1	10.5	-21.3
A33	5.4	-0.2	-11.4	-15.2	-7.6	7.3	16.7	11.5	-1.5	-25.0	-37.6
B33	-2.2	-5.7	-10.6	-16.2	-12.3	-3.2	6.0	7.8	2.9	-7.8	-17.7
A40	2.9	3.4	1.9	6.8	6.3	4.4	-2.3	-5.5	-5.9	2.2	13.9
A41	5.6	9.8	22.4	13.1	-0.2	-24.0	-27.7	-13.8	12.5	31.7	24.9
B41	-27.0	-22.7	-23.0	10.1	20.9	23.4	8.6	-5.0	-14.5	2.9	38.7
A42	3.1	-0.5	-3.8	-16.3	-17.8	-18.4	-8.5	2.4	11.0	12.2	-0.1
B42	-41.7	-32.5	-19.8	19.6	27.6	6.4	-7.5	-11.9	5.1	27.4	45.8
A43	26.1	12.9	-18.6	-33.0	-25.9	8.6	15.5	15.1	-11.3	0.7	28.3
B43	8.3	4.0	-5.7	-9.1	-6.4	1.2	3.9	4.5	-1.6	1.8	8.5
A44	-12.6	-10.8	-7.9	3.5	8.3	5.5	5.1	1.6	3.0	-2.0	-4.8
B44	19.9	19.9	9.9	23.1	25.3	37.3	19.1	0.4	-22.8	-13.6	24.0
A50	14.7	4.3	-11.9	-35.4	-32.5	-15.7	3.3	11.5	4.7	-10.6	-29.1
A51	-3.7	0.9	4.4	24.1	28.3	28.6	16.5	0.2	-10.0	-18.4	-8.3
B51	34.4	31.6	31.4	4.4	-6.1	-6.1	1.5	6.9	8.7	-10.8	-38.2
A52	-32.2	-31.4	-29.6	-13.9	-2.4	1.8	8.0	6.4	5.1	-0.4	-3.3
B52	-0.2	-0.0	-1.7	6.0	12.0	20.6	21.6	13.5	2.2	-11.3	-13.4
A53	6.6	3.2	-1.5	-12.0	-13.7	-13.3	-7.7	-1.7	2.2	1.9	-5.0
B53	-23.0	-19.1	-15.0	5.5	12.7	15.1	7.6	-4.1	-12.8	-15.8	-3.5
A54	27.1	32.2	41.6	35.8	24.0	15.1	5.1	2.1	4.4	4.2	2.2
B54	-8.8	-9.2	-6.2	-11.4	-10.0	-4.2	2.6	1.7	-4.2	-21.3	-34.5
A55	-0.3	9.0	24.5	37.3	30.0	16.6	-0.6	-6.4	-2.9	11.8	28.1
B55	43.8	40.6	40.9	7.4	-5.3	-2.7	7.5	13.6	13.2	-12.3	-46.3
A60	-5.4	-8.9	-22.0	-11.5	-4.4	6.4	0.5	-3.7	-13.6	7.9	40.6
A61	-6.6	-4.6	-0.3	2.3	0.4	-4.9	-9.0	-9.9	-7.2	-4.2	-0.9
B61	-52.0	-44.3	-33.3	5.7	17.0	1.2	-8.9	-15.0	-2.5	11.2	26.0
A62	-12.4	-10.6	-3.6	-1.3	0.4	-7.7	-0.8	3.7	14.2	3.8	-16.7
B62	37.4	32.4	27.5	-3.1	-16.7	-24.0	-18.7	-5.8	7.9	8.3	-9.8
A63	35.1	25.7	9.9	-19.2	-23.1	-6.4	5.5	11.4	1.3	-8.4	-18.4
B63	59.3	49.6	36.0	-7.7	-18.2	-2.3	13.7	21.3	11.6	-13.7	-43.8
A64	9.5	6.6	0.2	-7.3	-7.5	5.6	6.0	1.9	-12.3	-16.9	-10.4
B64	29.7	23.8	9.9	-3.5	-3.3	19.2	20.7	12.0	-12.9	-27.4	-22.4
A65	25.3	27.8	34.6	22.8	11.7	7.5	0.6	-4.9	-10.8	-23.0	-28.7
B65	-6.3	-2.6	-0.3	17.3	18.2	5.4	-7.2	-11.0	-0.6	16.2	31.6
A66	46.6	39.0	26.2	-6.5	-14.6	5.9	12.4	10.9	-9.7	-28.3	-36.4
B66	25.4	20.6	18.2	-9.6	-16.2	-15.6	1.2	14.5	22.5	5.5	-29.5
σ_{even}	47.	42.	29.	19.	32.	31.	16.	31.	35.	18.	44.
σ_{odd}	55.	48.	32.	21.	35.	33.	17.	32.	37.	22.	52.

Values in meters per second. The two last lines are the a posteriori standard deviations for the B_2^2 and A_3^3 coefficients and are considered to be typical of even and odd degree l, respectively.

TABLE 2. Spherical Harmonic Coefficients for ξ at Selected Depths

	Depth, km										
	47	80-	80+	160	220-	220+	310	400-	400+	533	670-
A10	0.4	0.7	0.8	3.4	4.9	6.0	6.3	4.7	1.3	0.2	-0.3
A11	-0.2	-2.9	-7.2	-9.9	-5.6	-0.8	10.8	20.3	9.1	10.9	8.2
B11	22.4	22.4	21.9	12.7	4.1	-1.1	-8.0	-8.9	-2.8	-1.6	-0.5
A20	-6.2	-4.1	-1.0	6.3	9.0	9.6	8.4	4.0	0.5	-1.9	-2.5
A21	15.4	14.9	13.0	7.9	4.5	4.6	3.1	3.1	1.1	1.3	1.1
B21	8.5	5.7	1.1	-6.9	-7.8	-5.6	-0.4	5.6	2.9	4.4	3.4
A22	7.2	5.4	2.5	-3.6	-5.6	-5.4	-4.3	-1.5	-0.1	1.0	1.1
B22	6.2	8.9	11.8	15.6	11.9	10.1	-3.2	-16.6	-9.2	-12.9	-10.1
A30	12.0	9.6	6.1	-5.3	-10.9	-13.2	-13.8	-9.0	-2.1	0.9	2.0
A31	15.3	13.9	11.7	1.2	-6.4	-9.7	-16.3	-18.1	-7.2	-6.6	-4.8
B31	2.5	3.2	4.4	3.2	-0.2	-3.0	-9.1	-12.6	-5.1	-4.9	-2.9
A32	12.9	12.9	12.9	6.7	1.1	-2.0	-7.2	-9.3	-3.8	-4.1	-3.5
B32	-17.9	-17.5	-17.3	-5.6	5.6	12.3	24.8	29.8	11.8	11.2	7.7
A33	10.3	8.0	5.4	-8.8	-18.1	-24.5	-30.5	-27.0	-8.5	-4.1	-0.6
B33	-4.3	-4.0	-3.5	-1.7	-0.6	-0.4	-0.2	-0.6	-0.3	-0.5	-0.4
A40	6.0	3.9	0.4	-4.6	-3.4	-1.3	7.0	15.2	7.3	9.1	6.7
A41	4.3	3.5	1.8	0.4	1.2	2.8	6.6	10.3	4.7	6.0	5.1
B41	9.4	8.5	6.9	3.9	4.3	5.9	10.5	13.5	5.3	4.6	2.0
A42	5.0	3.9	2.1	-1.7	-3.3	-3.6	-3.7	-2.4	-0.6	0.3	0.6
B42	26.3	21.1	12.6	-7.3	-13.4	-13.0	-5.9	6.7	5.0	9.4	7.8
A43	4.9	1.0	-3.8	-12.5	-9.4	-7.8	11.3	32.0	16.9	22.5	17.4
B43	10.6	7.5	3.1	-7.9	-10.7	-11.6	-5.6	4.7	4.3	8.2	7.2
A44	9.1	7.4	4.5	-0.5	-0.9	0.3	5.2	10.9	5.3	6.8	5.3
B44	-3.7	-4.8	-6.1	-4.8	0.1	3.8	12.9	17.5	6.8	5.7	2.2
A50	9.6	9.1	8.7	-0.5	-9.6	-16.5	-27.5	-30.7	-11.3	-9.2	-5.1
A51	2.7	2.9	3.2	3.3	3.0	3.1	2.4	1.2	0.0	-0.8	-1.2
B51	-10.5	-8.2	-4.9	3.6	5.3	5.0	-1.2	-9.4	-5.3	-7.7	-5.9
A52	-1.7	-3.1	-5.5	-4.5	1.5	6.5	19.3	28.5	12.2	13.3	9.5
B52	-5.9	-6.0	-5.8	-3.6	-0.9	0.5	4.4	6.6	2.8	3.0	2.0
A53	8.2	6.3	4.0	-7.1	-14.3	-18.9	-23.6	-21.0	-6.7	-3.3	-0.5
B53	-2.8	-0.3	3.4	8.7	7.6	6.0	-2.3	-11.8	-6.6	-9.8	-8.3
A54	-20.4	-17.1	-12.2	4.0	11.8	15.6	14.8	6.0	-0.3	-5.0	-5.6
B54	-20.6	-16.5	-10.3	6.3	12.3	14.1	9.1	-2.3	-3.7	-8.5	-7.7
A55	-22.6	-18.4	-12.2	7.4	16.9	21.9	21.4	10.6	0.7	-5.6	-6.9
B55	-20.7	-17.9	-14.2	3.4	14.0	19.3	24.3	20.9	6.7	3.6	1.6
A60	15.3	11.2	5.3	-7.5	-8.2	-7.2	6.8	23.7	12.7	17.5	13.6
A61	2.4	4.0	6.3	7.6	4.2	1.4	-7.4	-14.7	-6.9	-8.4	-6.2
B61	19.5	15.9	10.0	-4.0	-9.1	-8.5	-6.8	-2.2	-0.4	0.9	0.5
A62	9.6	8.9	7.6	1.4	-3.4	-6.0	-9.3	-8.0	2.2	0.1	1.7
B62	7.1	4.2	-0.2	-9.9	-13.5	-14.6	-13.9	-9.0	-2.3	0.6	1.8
A63	-4.3	-5.6	-7.0	-8.0	-5.3	-4.6	4.1	13.6	7.6	10.8	9.1
B63	-9.7	-8.0	-5.1	0.7	1.4	-0.8	-4.9	-8.5	-3.3	-3.3	-1.6
A64	-13.1	-9.6	-4.1	8.5	12.5	12.7	8.8	0.5	-1.6	-5.3	-5.2
B64	-12.5	-9.3	-4.2	7.3	10.6	10.1	5.7	-2.7	-2.8	-6.3	-6.1
A65	-15.0	-10.3	-2.9	9.3	8.4	5.0	-10.7	-27.5	-13.6	-17.9	-13.7
B65	20.8	14.2	4.5	-17.4	-22.2	-21.6	-9.1	10.0	7.8	14.7	12.7
A66	-24.9	-20.6	-13.4	3.0	8.0	7.3	1.1	-9.4	-5.6	-9.2	-7.6
B66	0.8	0.6	-0.1	-0.6	-0.8	-1.4	-0.8	1.3	1.4	3.1	3.6
σ_{even}	22.	20.	19.	16.	20.	17.	13.	19.	10.	11.	16.
σ_{odd}	27.	23.	21.	19.	23.	21.	15.	23.	12.	15.	18.

Units are 10^{-3}. See Table 1 footnotes.

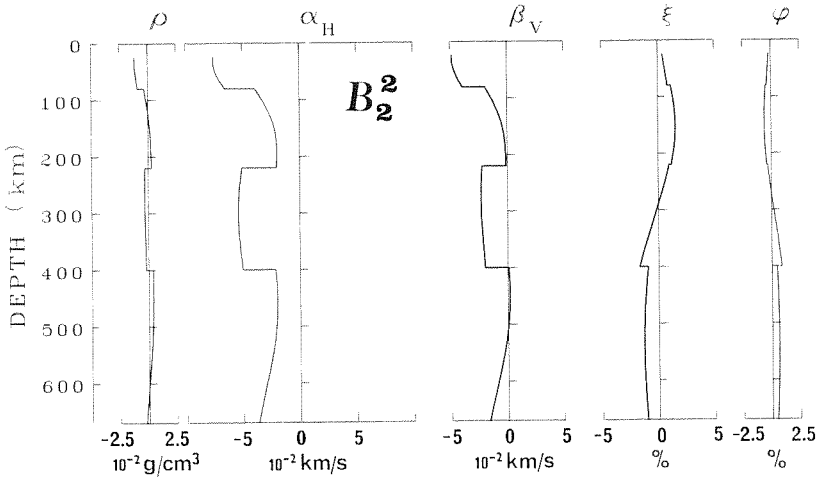

Fig. 22. Spherical harmonic coefficient B_2^2: model. Variations of the five inverted parameters as a function of depth. Same conventions as in Figure 9 but note that the horizontal scales are different.

depth, it has the largest β_V amplitude (0.042 km/s) of all coefficients, well above the noise level (0.022 km/s), and is needed to fit the very fast short-period Rayleigh waves (NA2). It also shows a significant S anisotropy (0.8%) between 200 and 400 km. It is interesting to note that the highest degrees in our expansion (5 and 6) have large velocity variations, especially at shallow depths. As we will see in the next section, this is a consequence of the strong variations that occur between different oceanic provinces or between oceans and continents, on a lateral scale equal to or smaller than 3500 km (the half wavelength of a degree 6 spherical harmonic function). This was shown in the regionalized data of Nakanishi and Anderson (1983, Figures 19 and 20).

10.2. Fits

For most spherical harmonic coefficients we obtain a good simultaneous fit of both Love and Rayleigh waves. Indeed the misfit to the T versus n data is always smaller than the data standard deviation for both Love and Rayleigh waves over the entire period range from 100 to 250 s for all spherical harmonic coefficients, with only two exceptions: the A_2^1 and A_4^3 coefficients for 100-s Rayleigh waves, for which the misfit reaches -1.2 and 1.3 times the standard deviation, respectively. This is a good indication that the inverse problem for a given coefficient is only weakly nonlinear and that the parameterization of our model is adequate. Although we invert only the T versus n data, the fit to group velocities is also quite good, a consequence of our method for combining phase and group velocity data before performing the inversion. For periods lower than 200 s, the misfit to group slowness is smaller than the error bar for both Love and Rayleigh waves, except for a few coefficients such as B_4^4 and A_6^5, for which the misfit reaches -1.9 times the error bar at 150 s. Above 200 s, the fit to group slowness deteriorates rapidly. For 240-s period Love waves, the misfit is larger than the data standard deviation for 22 coefficients, up to a factor of -2.6 for the A_4^1 coefficient. The closeness of the fits will be best seen on the maps obtained by recombining the coefficients. However, it is useful to examine one example of

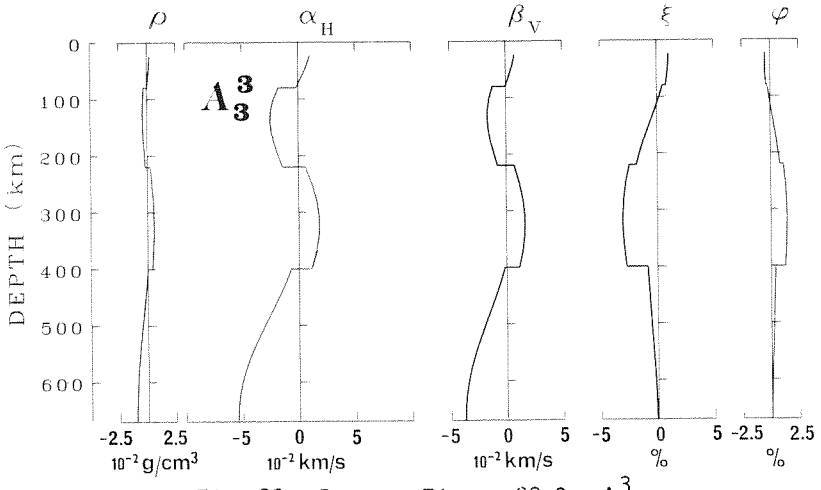

Fig. 23. Same as Figure 22 for A_3^3.

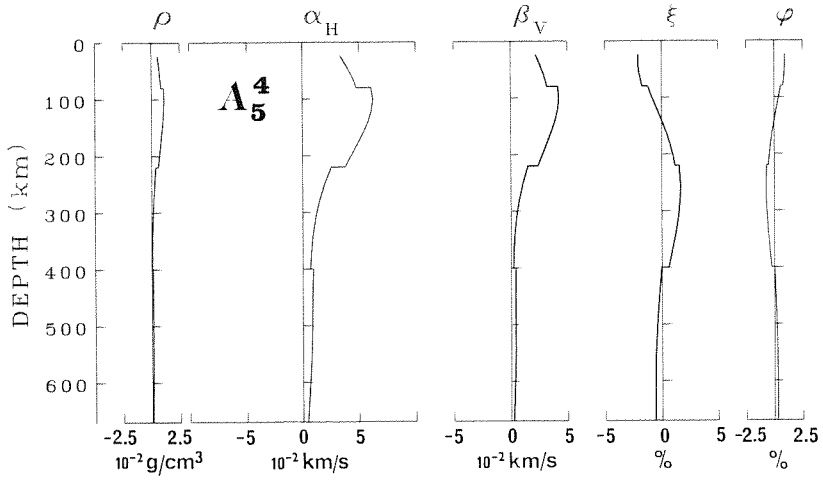

Fig. 24. Same as Figure 22 for A_5^4.

the fit obtained for an individual coefficient. Figure 25 shows the fit given by our B_2^2 model to the corresponding data (transformed through our combination algorithm, and after removal of the shallow layers' contribution) for both period and group slowness for Love and Rayleigh waves. The fit is quite good and always within the error bars, except for the longest-period group slowness of Rayleigh waves. Therefore our B_2^2 model is able to explain the observed heterogeneities for periods up to 270 s (mode $_0S_{28}$).

10.3. A Posteriori Standard Deviations

The a posteriori standard deviations have been calculated for a few spherical harmonic coefficients. Although they depend somewhat on the errors of the data, which are different from one coefficient to another, it would be too time consuming to calculate them for all the coefficients. The plot in Figure 26 (the a posteriori standard deviations for the B_2^2 and A_3^3 coefficients) can be considered as typical. The corres-

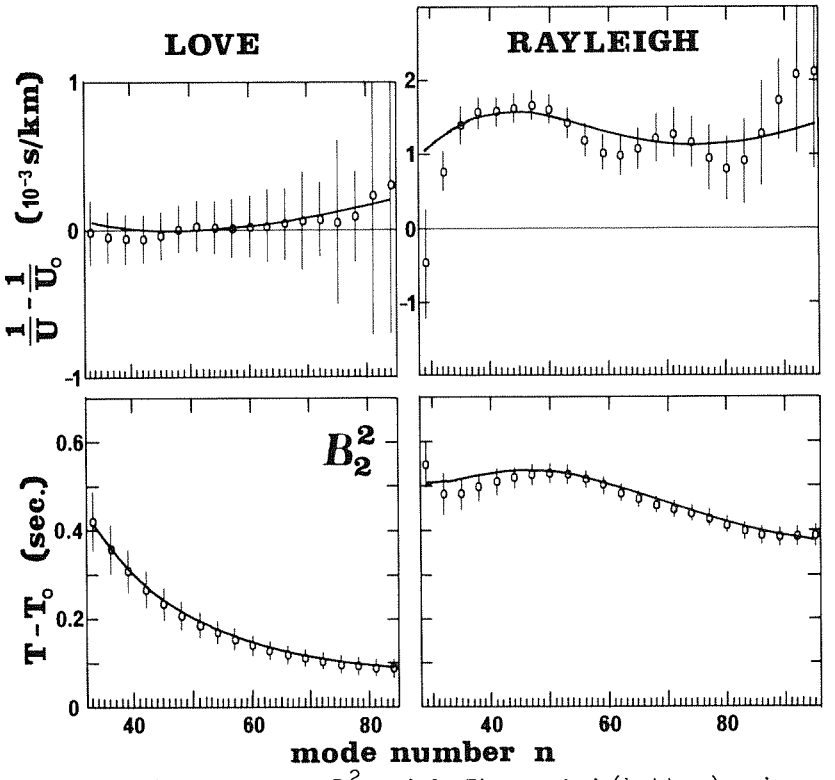

Fig. 25. Fits to the data from our B_2^2 model. The period (bottom) and group slowness (top) data points (at given mode numbers n) and their 2σ error bars have been derived from the original phase and group slownesses at given periods according to our special algorithm. The solid lines are the fits given by our B_2^2 model (drawn in Figure 22). Note that even the longest periods are well fitted. Other conventions as in Figure 13.

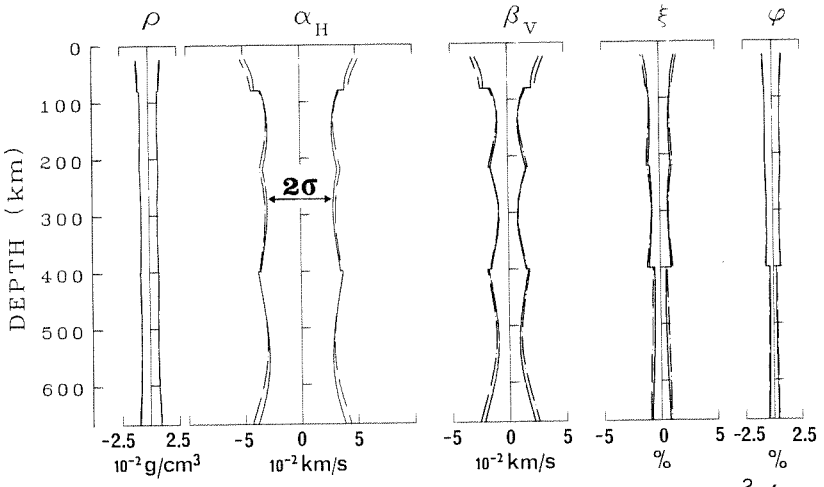

Fig. 26. A posteriori standard deviations on the parameters for the B_2^2 (solid line) and A_3^3 (dashed line) spherical harmonic coefficients.

ponding values for β_V and ξ are reported in the last lines of Tables 1 and 2. We note that the variance reductions are slightly larger than in the case of the regionalized inversion (maxima of 98% for β_V, and 93% for ξ). This is primarily due to the constraints brought in by the group velocity data through the combination algorithm.

10.4. Reliability Tests

To assess further the reliability of the models, we compare them to the results of an earlier inversion derived with a different, and less realistic, in our opinion, a priori information. It concerned a degree 7 expansion (instead of the present degree 6 expansion) and had the following a priori information: no a priori correlation between parameters; inversion for ρ, α_H, β_V, ξ, ϕ, and η with a priori standard deviations equal to 0.1 g/cm^3, 0.1 km/s, 0.1 km/s, 0.1, 0.1, 0.1, respectively; a correlation length of 100 km; and $\lambda=0$ at discontinuities. Figure 27 compares the two inversion results for the A_6^5 coefficient (a "good" coefficient). As expected, the parameters ρ, α_H, ϕ, and η, for which the data bring almost no information, show little resemblance. However, β_V and ξ, which are the best resolved parameters, show very similar trends in the two inversions, except for the uppermost β_V structure where we know that the resolution is poor. This gives us some confidence that the features we will discuss later are in fact robust. The situation is not as nice when dealing with the "bad" coefficients. Figure 28 compares the two results obtained for the A_3^3 coefficient. Although the dominant feature (strong negative S anisotropy between 220 and 400 km) is present in both inversions, the β_V structure is totally different. This points again to the danger of contamination that erroneous or poorly constrained coefficients can bring into the maps obtained by recombining the coefficients.

11. Combining the Spherical Harmonic Inversion Coefficients

By recombining the spherical harmonic coefficients obtained from the inversion at a chosen depth, it is possible to build a picture of the earth's lateral heterogeneities. This picture is

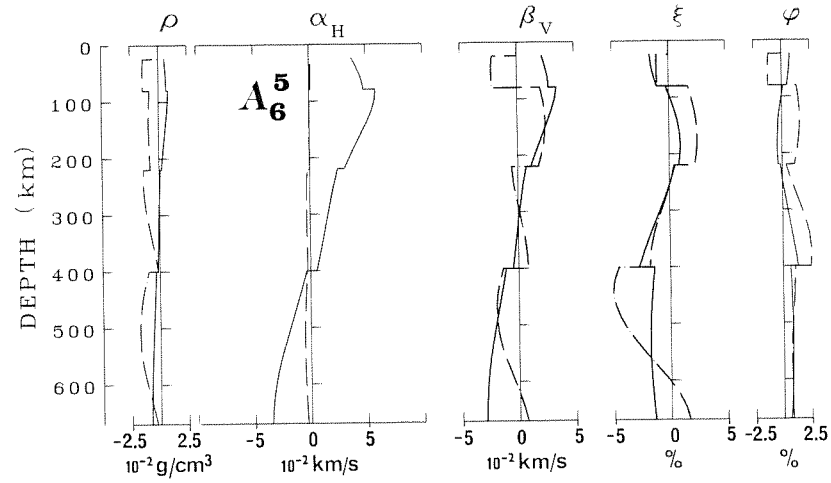

Fig. 27. Comparing two A_6^5 models obtained with very different a priori information (see text). Same conventions as in Figure 22. Note that the two well-constrained parameters β_V and ξ are very similar in the two inversions of this "good" coefficient.

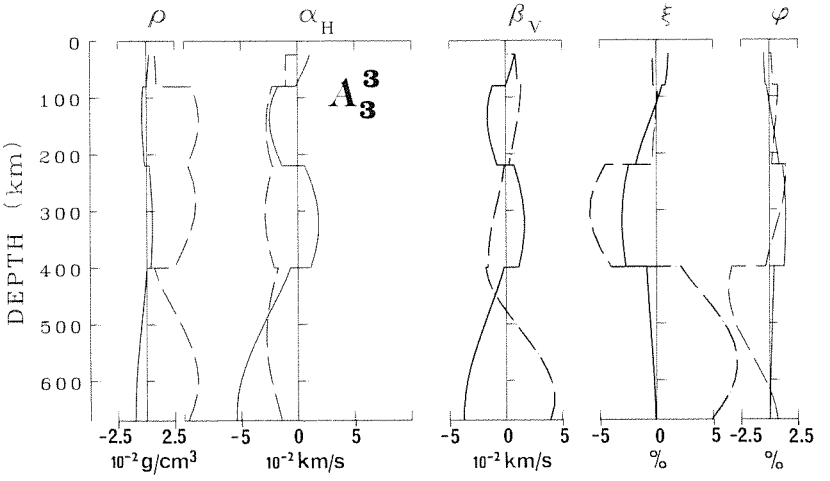

Fig. 28. Same as Figure 27 but for a "bad" coefficient: A_3^3. Note that even the best resolved parameters β_V and ξ have little in common from one inversion to the other.

rather coarse as yet, since harmonics up to degree 6 only are used. Nevertheless, it has the precious advantage that no a priori information based on surface tectonics has been used to produce it. It therefore gives us a more "objective" view of what the earth's upper mantle really looks like. Paradoxically, the first thing we will try to find in these maps is the signature of the features that are known to be associated with surface tectonics.

11.1. Shear Wave Velocity Heterogeneities

Figure 29 shows maps of the SV heterogeneities at selected depths. At 50 km the correlation with surface tectonics is striking (as pointed out by Nataf et al. (1984)). All major shields show up as fast regions (Canada, South America, Africa, Antarctica, West Australia, Siberia). Most ridges show up as slow regions (East Pacific, triple junctions in the Indian and Atlantic oceans, East African rift). The amplitude of the variation is quite large (±10%) but is somewhat unconstrained since the a posteriori standard deviation is also quite large at this depth. At 150 km the pattern remains much the same. The amplitude of the heterogeneities, better constrained at this depth, is now only ±6%, comparable to the range found in body wave studies. Farther down, at 250 km, most shields have retained their fast signature; not all ridges are slow, but the East African region remains slow. At 350 km the fast regions seem to trace the subductions zones (Pacific belt, Mediterranean basin, Antilles, South Sandwich). At 450 km the fastest regions are the South Atlantic and Eurasia. The correlation with surface tectonics seems to have disappeared; ridges are no longer slow. At 550 km the picture is not very different, and resolution becomes poor. In this brief survey we have concentrated our attention on the regions that seem to correlate with surface tectonics. The real goal of our study is, however, to try to go one step beyond and detect "anomalous" regions. We cautiously point to a few: the region around French Polynesia seems to behave differently from the surrounding oceanic regions: quite slow at shallow depth, it becomes fast at 250 km and slow again at greater depths. The Red Sea is surrounded by a wide slow anomaly. The central Pacific is fast at shallow depths and slow at greater depths. Southeast of South America lies a region that is fast at all depths, except around 250 km. Though exciting, these findings must remain tentative at this stage. Indeed, the poor behavior of some of the spherical harmonic coefficients and the lack of resolution, both horizontally and vertically, do not allow us to make definitive statements about these seemingly anomalous regions.

11.2. Shear Wave Anisotropy Heterogeneities

Since the signature of surface tectonics in terms of S anisotropy is not well established, the interpretation of the ζ maps shown in Figure 30 must be done with even more care. As expected from the resolution/trade-off curves, the first map, at 50 km, bears a strong resemblance to the β_V map at the same depth, with the opposite sign. The amplitude of the anomalies is unrealistically large (±10% (SH-SV)/SV anisotropies). At 150 km the amplitudes are much less (±5%), and the pattern is quite different. Note that the anisotropies are deviations from the average. Since the average earth model (PREM) is anisotropic at this depth, with SH>SV, there are more regions with SH>SV (i.e., horizontal flow) than it appears from the map. Regions with SV>SH (i.e., vertical flow) are mostly west and South America and a large part of the South Atlantic Ocean and Africa. At 250 km and 350 km, where the trade-off with β_V is minimum, most ridges seem to have SV>SH (i.e., vertical flow). The amplitudes are around ±8%. Old regions of the Pacific ocean also have SV>SH. Antarctica and South America have strong SH>SV (i.e., horizontal flow) signatures. We notice a strong N-S sectorial zoning in the 250 km map, probably the contribution of the large A_3^3 and A_5^5 coefficients. We have seen that these coefficients were poorly behaved. This is one more reason to be cautious about the significance of the S anisotropy heterogeneities.

11.3. Fits to the Data

In section 10.2 we have discussed the fit obtained for the period and group slowness versus mode number data for the individual spherical

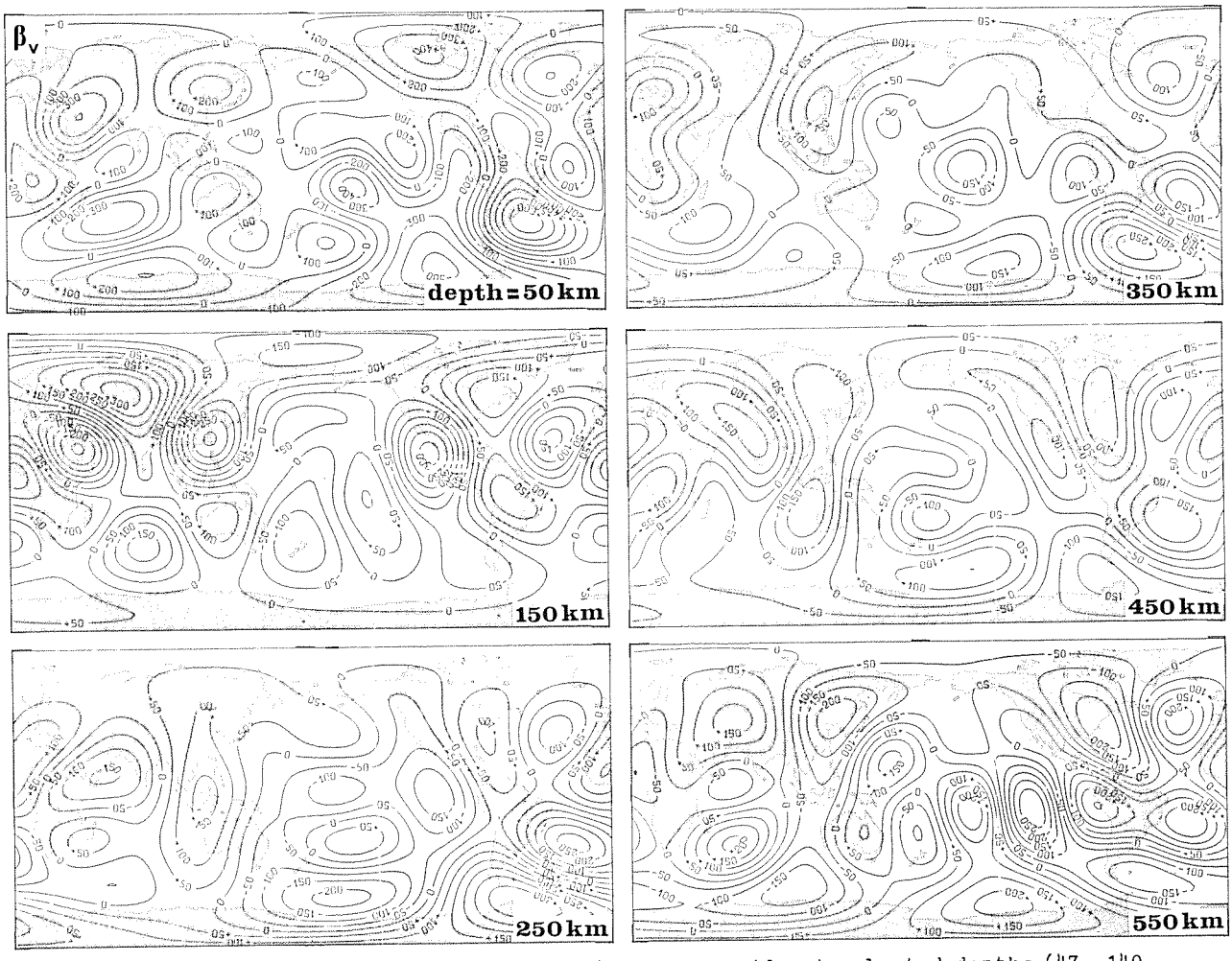

Fig. 29. Maps of β_V heterogeneities in the upper mantle at selected depths (47, 140, 250, 340, 444, 556 km), synthetized from our degree 6 spherical harmonic expansion models. The contour interval is 50 m/s (100 m/s for the shallowest map).

harmonic coefficients. Here we compare the maps obtained by recombining the original phase and group velocity coefficients (before phase and group velocities were combined and transformed and before crustal corrections were applied) to the fits produced by our model. A few examples are given in Figure 31. It is remarkable that the fit is very good for Love and Rayleigh waves simultaneously for both phase and group velocities, even though we did not invert the latter directly. However, the fit deteriorates for the largest periods, as mentioned in section 10.2. In particular, the group velocity map for 250-s Love waves fails to match the amplitudes seen in the data. Nevertheless, the patterns are very similar, and the amplitudes predicted by our fit are in fact probably more realistic (NA2).

12. Discussion

In this section, we try to assess further the reliabilty of the results presented in the previous section by comparing them to other recent models. We also discuss their geodynamical relevance and examine the correlation with the geoid. Finally, we examine the validity of the geometric optics approximation in the light of our results.

12.1. Comparison With Woodhouse and Dziewonski's Models

Woodhouse and Dziewonski (1984) have recently produced models of the heterogeneities of shear wave velocities in the upper mantle. They also chose a spherical harmonic representation. A comparison of the two results is a useful check, since the data, their treatment, the inversion procedure, and the authors are different. Woodhouse and Dziewonski obtain their models by direct waveform inversion of Love and Rayleigh waves with periods larger than 135 s. Their path coverage being much denser than ours (they use about 4 times as many paths as we do), they can push their expansion up to degree 8. They retain only the differences between average ocean and average continent to treat crustal corrections, and they do not allow for lateral variations in anisotropy. One can compare individual spherical harmonic coefficients as a function of depth or maps of recombined coefficients at a given depth.

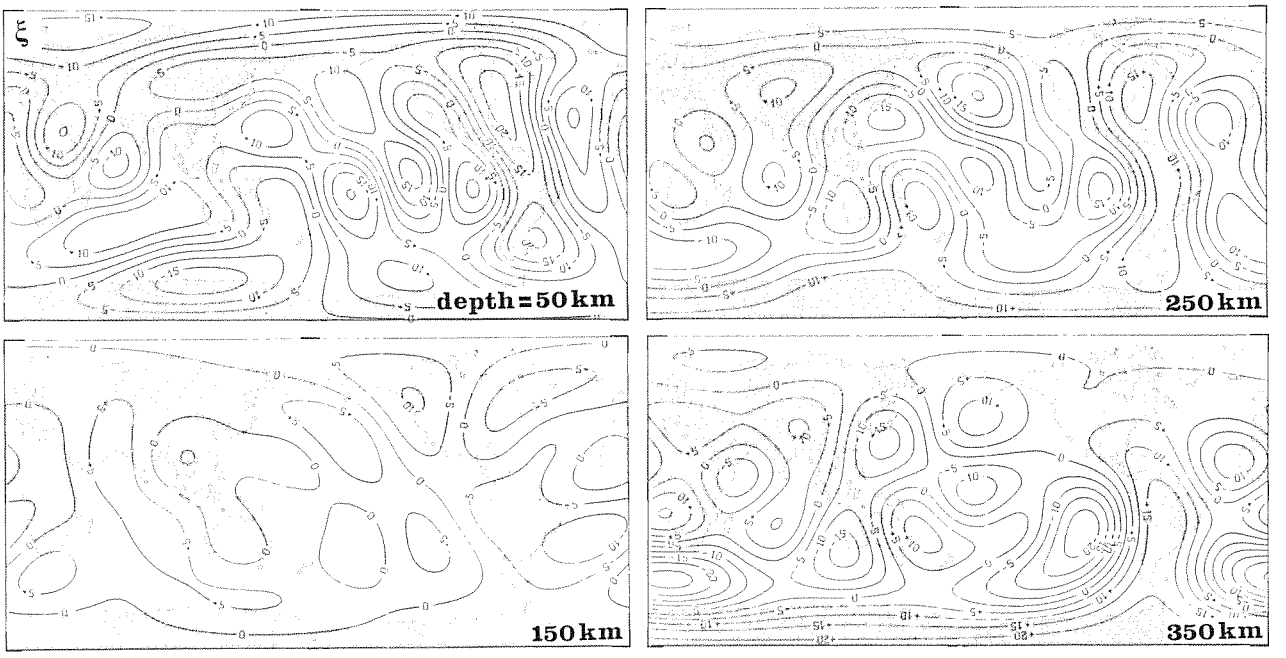

Fig. 30. Maps of ξ heterogeneities in the upper mantle at selected depths (47, 140, 250, 340 km), synthetized from our degree 6 spherical harmonic expansion models. The contour interval is 5%. Divide by 2 to obtain approximate (SH-SV)/SV anisotropy.

12.1.1. Maps. The maps of our Figure 29 can be compared directly to their Plate 2 (their model M84C). The resemblance between the two sets of S velocity maps is striking down to a depth of about 400 km. Below 400 km, the two models have little in common, except the fast velocity region in the South Atlantic. Their shallow maps delineate more closely surface tectonics features than ours, probably because of the better horizontal resolution achieved in their study. We note that the anomalous regions under French Polynesia and the central Pacific are also present on their maps. The anomaly we described southeast of South America and the one around the Red Sea are displaced to much greater depths in their model.

12.1.2. Individual coefficients. We compare the results of the two studies for the B_2^2 coefficient. As we have already mentioned, it is an interesting coefficient in that it carries most of the degree 2 variation. In both studies, it is one of the best resolved coefficients. The two models are plotted in Figure 32, together with Masters et al.'s (1982) transition zone model. Although Masters et al. did not include crustal corrections, it is not important here since these corrections are very small for the B_2^2 coefficient (see Appendix A). It is remarkable that all three studies agree on the sign and on the size of the heterogeneity. However, they disagree on the depth of that anomaly. Our model requires no anomaly below 400 km. Since both Woodhouse and Dziewonski (1984) and Masters et al. (1982) analyze data at longer periods than we do, they have more resolution at depth. On the other hand, if shallow anomalies, better constrained by our shorter-period data, are as large as we find them, they could be responsible in part for the long-period anomaly. In any case, it appears that even for the best resolved spherical harmonic coefficients there may be a serious problem for constraining the depth of the heterogeneity responsible for the surface wave variations.

12.2. Comparison With Our Regionalized Models

Our regionalized models can be expanded in spherical harmonics and compared to the direct spherical harmonic expansion models. That comparison is useful for determining the origin of the heterogeneities and for discussing which places are "anomalous." Once again the comparison can be performed coefficient by coefficient or by looking at maps of recombined coefficients.

12.2.1. Coefficients. Figure 33 gives the variation with depth of the B_2^2 coefficient obtained from the expansion of our regionalized models. The plot can be compared directly to the plots of Figure 32, except that the scale has been increased by a factor of 5. Indeed, the amplitudes of the anomalies are much less for the regionalized expansion; this is not unexpected since the regionalization has averaged out some of the variations; also, the a priori information for the inversion is not quite the same. However, the large negative β_V anomaly is rather similar to the direct B_2^2 inversion model and in fact is closer to Woodhouse and Dziewonski's results due to its deep negative signature. The resemblance between the two S anisotropy models is striking; they seem to differ only in amplitude. The same is true for the other degree 2 coefficients (except for the A_2^1 anisotropy). We are led to follow Kawakatsu (1983) and Nakanishi and Anderson (1983) in affirming that regionalized models can indeed predict the observed degree 2 patterns; their conclusion being now extended from data to

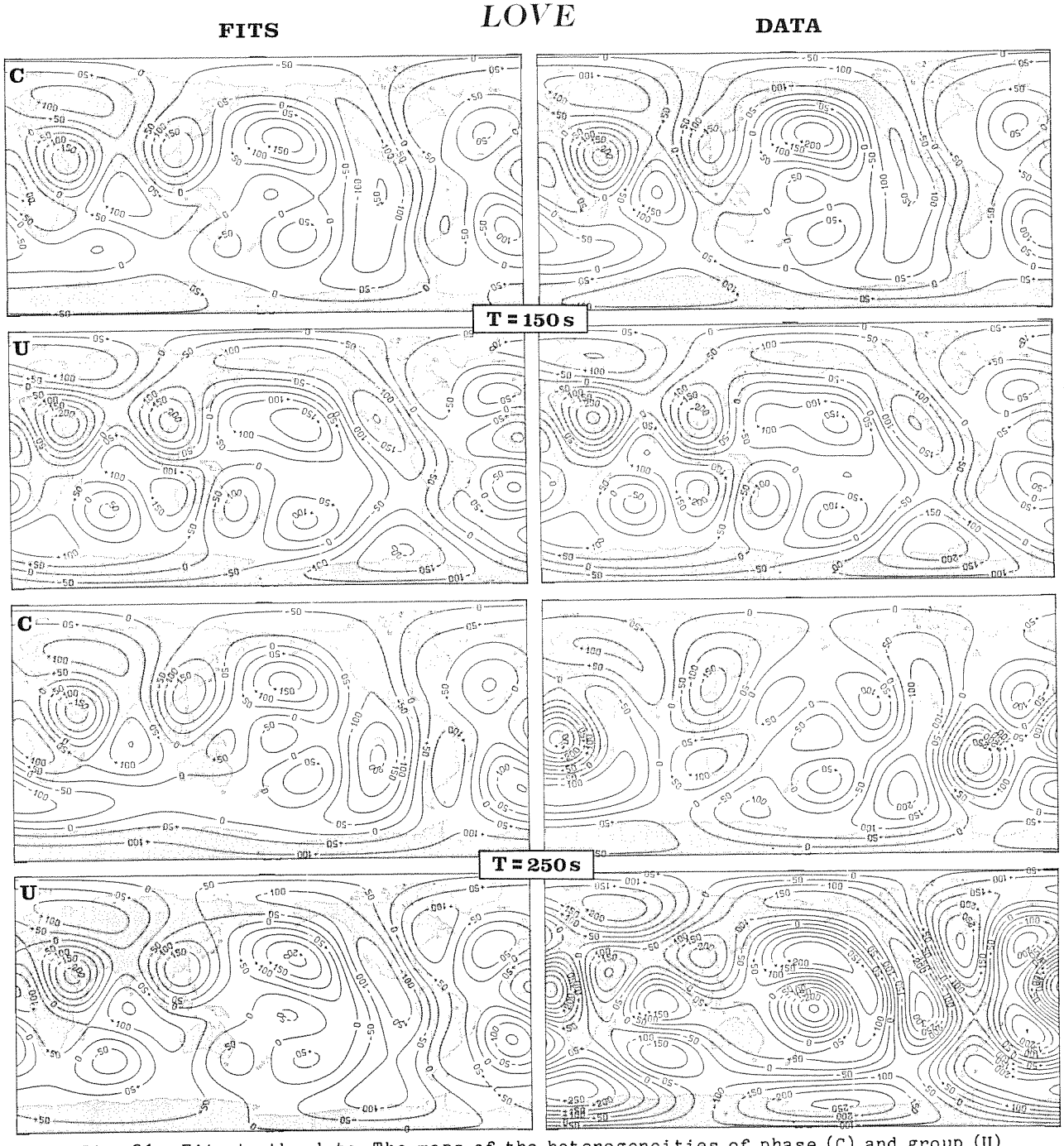

Fig. 31. Fits to the data. The maps of the heterogeneities of phase (C) and group (U) velocities for Love and Rayleigh waves synthetized from a degree 6 expansion in NA2 are compared to the corresponding maps predicted by our inversion model, at 150 and 250 s. The corrections due to shallow layers, which had been subtracted before inverting, have been added back to the predicted fits. The contour interval is 50 m/s. No filtering has been applied.

models and for both β_V and S anisotropy. Such a statement might be misleading: it does not mean that degree 2 features are intrinsically linked to surface tectonics. In fact, "pure path" regionalizations are very sensitive to degree 2 heterogeneities (Kawakatsu, 1983). If there exists a degree 2 pattern of heterogeneity, the regionalization has enough degree 2 sampling to unduely distribute these heterogeneities between the different regions.

12.2.2. Maps. Figure 34 shows degree 6 maps of the regionalized shear wave velocities at selected depths. The amplitudes are much smaller than those obtained from the direct spherical harmonic inversion. At 150 km both shields and ridges clearly show up. At 350 km there is an interesting result: at this depth, all the oceanic regions but one (the oldest ocean, region A) have the same velocity (see Figures 9 and 10), and continents are fast. However, on the degree 6

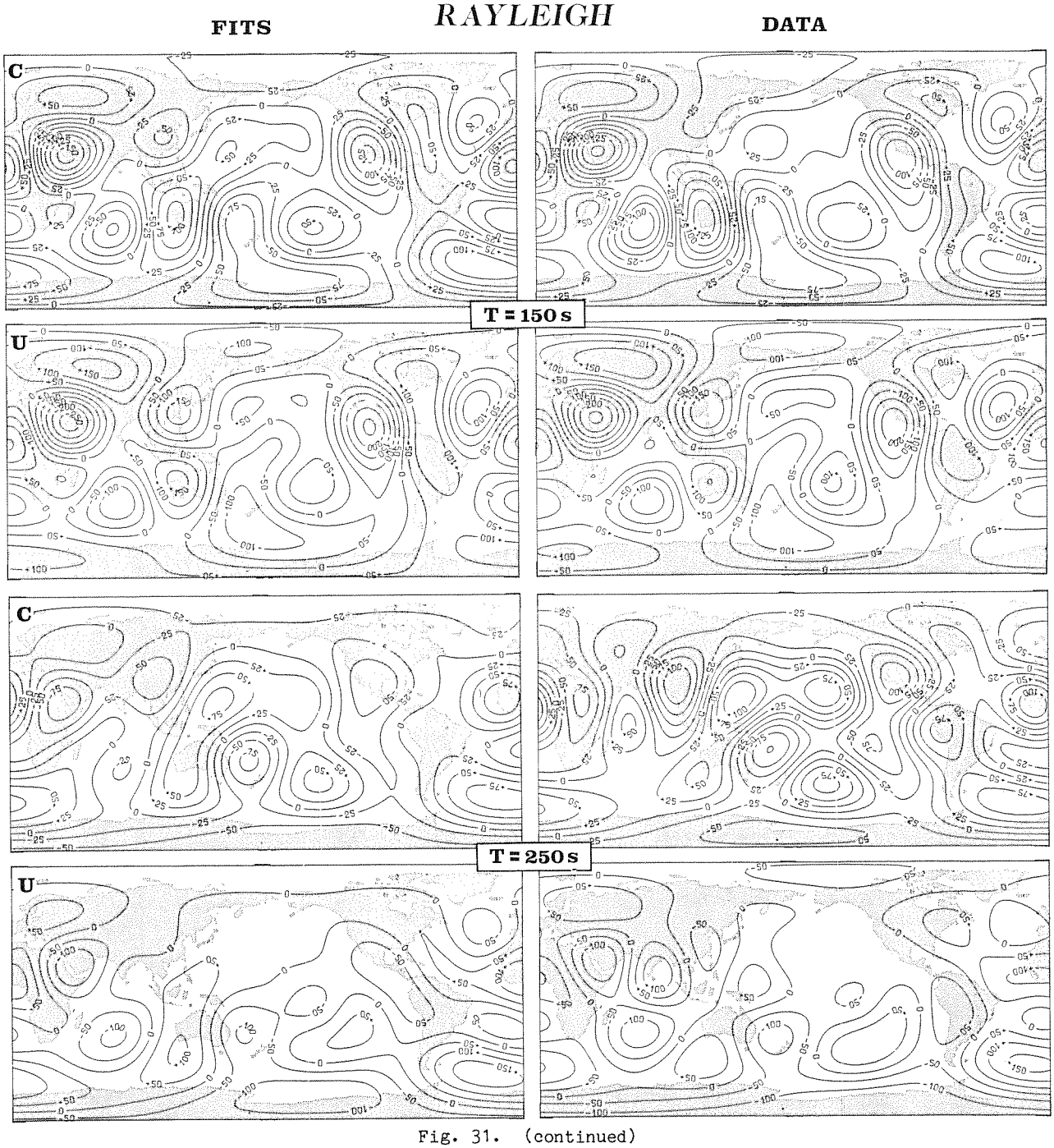

Fig. 31. (continued)

filtered map, ridges seem to show up as slow regions. This may be an artifact due to the coarseness of the expansion and to the fact that ridges are parts of the ocean that often lay at equal distances from the surrounding continents. At 450 km the dominant feature is the fast signature of the subducted slabs (region T), as in the direct expansion at a somewhat shallower depth.

The degree 6 maps of the regionalized anisotropy bear little resemblance to the direct inversion maps, despite the great similarities between their degree 2 components. This could mean that anisotropy is not simply related to surface tectonics or that our results for anisotropy are very poorly constrained.

12.3. Correlation With the Geoid

If the shear velocity anomalies that we determine are indeed due to temperature variations in the mantle, the variations in density that they produce should alter the gravity field of the earth. It therefore seems natural to correlate the geoid with the lateral heterogeneities of seismic velocities in the mantle. The spherical harmonic decomposition is particularly well suited to do this operation since the spherical harmonic coefficients of the density heterogeneities can be integrated directly to yield an equivalent geoid coefficient. In a dynamic earth, however, density heterogeneities at depth produce

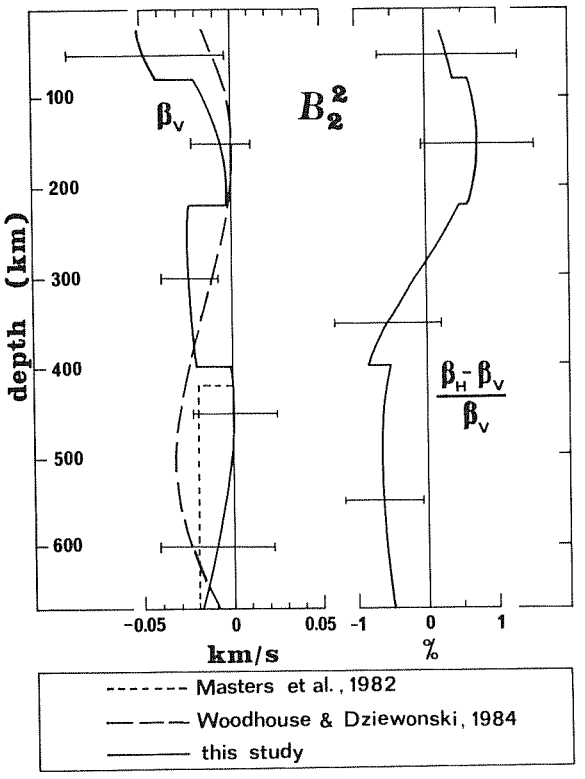

Fig. 32. A comparison of the β_V B_2^2 models obtained by different authors for the B_2^2 spherical harmonic coefficent. The model drawn with the error bars for β_V and S anisotropy is our model. The dashed line β_V model has been obtained by Woodhouse and Dziewonski (1984) by waveform inversion. The short dashed line is a simple β_V model that was found by Masters et al. (1982) to give a good fit to the shifts of spheroidal modes periods. All models have been converted to β_V variations by using an average β_V value of 5 km/s. The $Im(\delta m_2^2)$ of Masters et al. has been corrected by a $-1/\sqrt{2\pi}$ normalization factor to perform the comparison.

deformations of the surface that often contribute more to the geoid than the actual heterogeneity (McKenzie, 1977). Since very shallow heterogeneities are not resolved at all in our study, one can wonder if the geoid calculated directly should bear any resemblance to the real geoid. Recently, the geoid response of a spherical dynamical earth to density heterogeneities at depth has been derived for different possible earth models (Ricard et al.; 1984, Richards and Hager, 1984). In this approach, for a given spherical harmonic order l, the deformation of the surface, and of other interfaces at depth, caused by a density heterogeneity are calculated, and a resulting geoid response is produced that takes into account all contributions. Hager (1984) has used this approach to compute the geoid anomalies caused by the subducted slabs. Here we use the geoid response of the model e of Ricard et al. (1984) to calculate the equivalent geoid produced by the density heterogeneities we deduce from our seismic model. Figure 35 is a plot of the correlation coefficients between the real geoid and the calculated geoid, versus the degree l, obtained by various authors. The lower mantle P velocity model of Dziewonski (1984) shows a remarkable l=2 anticorrelation with the geoid. A significant l=2 positive correlation for the upper mantle is found by Masters et al. (1982) and Woodhouse and Dziewonski (1984). However, the correlation is found for S velocity upper mantle models that were derived without taking into account crustal corrections. Woodhouse and Dziewonski (1984) point out that when these corrections are introduced, the l=2,3 correlation with the geoid breaks down. Masters et al. and Woodhouse and Dziewonski obtained the calculated geoid by direct integration of the seismic heterogeneities. Our model, which includes crustal corrections, has no l=2,3 correlation with the geoid. For degrees l=4,5,6, we find a marginally significant correlation when using the dynamic response of a stratified mantle with a chemical boundary at 670 km (model **e** of Ricard et al. (1984)). The correlation is maximum (r=0.6) for degree 5. For this degree the geoid that we predict using our density model has the same amplitude as the observed one. On the contrary, Woodhouse and Dziewonski (1984) predict the wrong sign for the geoid and an amplitude too large by a factor of 5. However, Hager et al. (1985) show that a very good positive correlation is obtained for degrees l=2,3 when the dynamic response of a single-layer convecting mantle is applied to Dziewonski's (1984) lower mantle model. Density heterogeneities associated with subducted slabs seem to contribute significantly to the higher degree components of the geoid (Hager, 1984).

The correlation found between the seismic

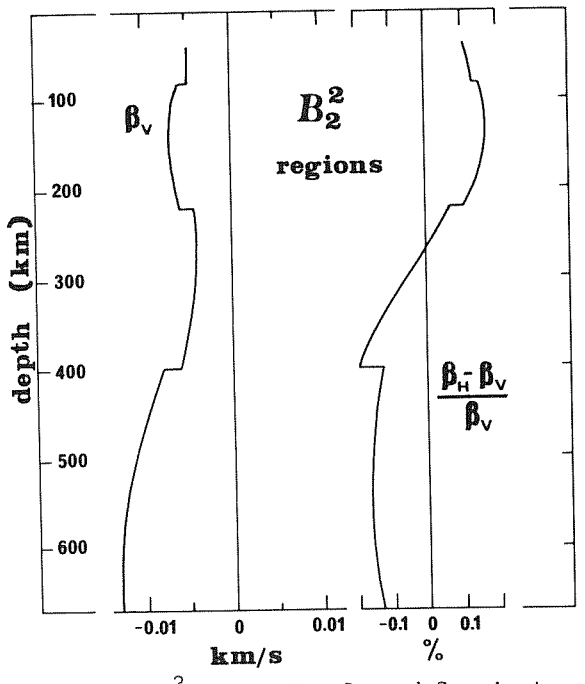

Fig. 33. The B_2^2 model for β_V and S anisotropy obtained by expanding our regionalized models in spherical harmonics. The result is very similar to the models presented in Figure 32, obtained by direct spherical harmonic inversion. Note that the horizontal scale is 5 times as large in this figure.

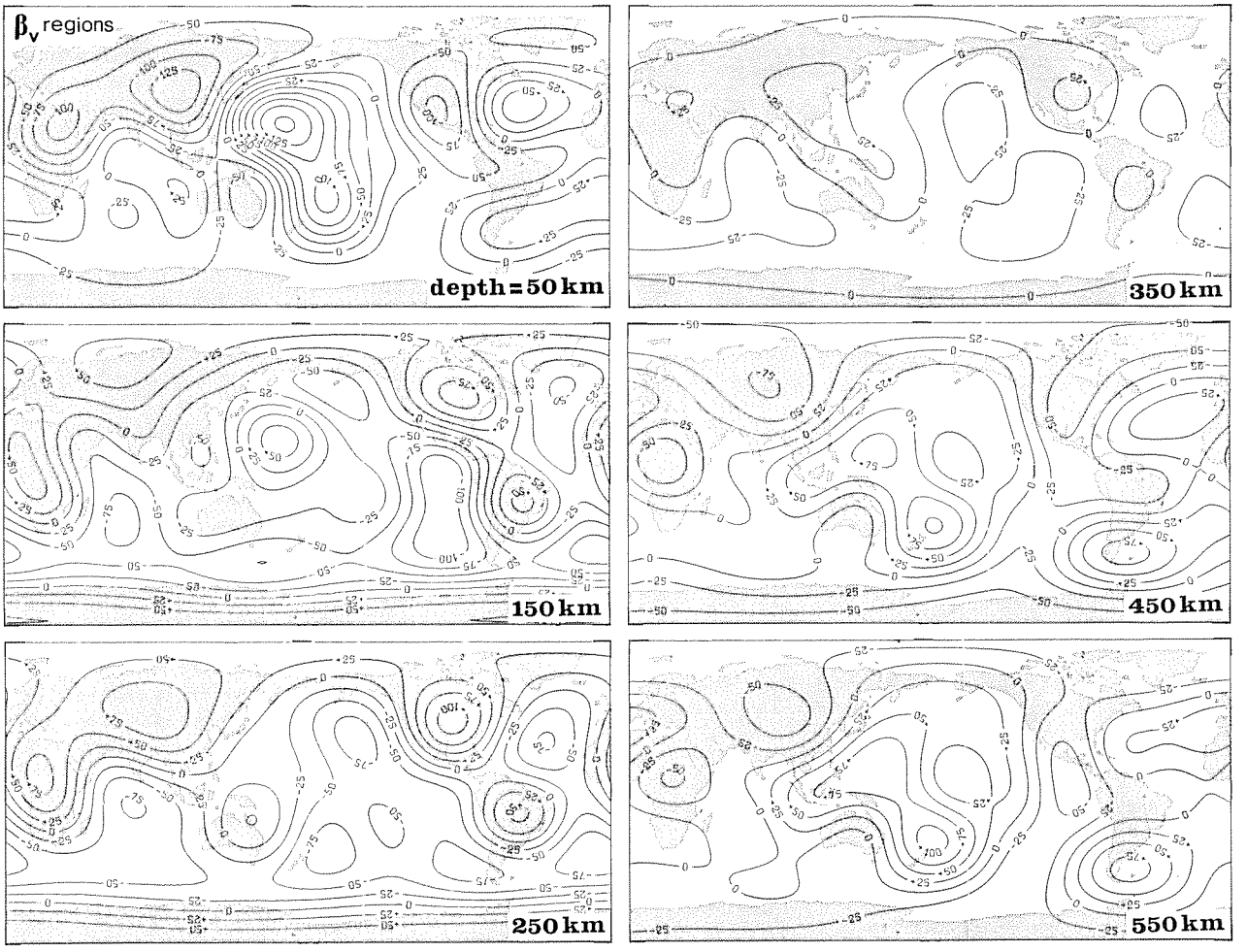

Fig. 34. Contour maps of the β_V lateral heterogeneities at various depths obtained from the degree 6 spherical harmonic expansion of our regionalized models. The contour interval is 25 m/s. Compare to the results of the direct spherical harmonic inversion of Figure 29.

models and the geoid is encouraging. From the results obtained so far, it is clear that density heterogeneities in both the upper and the lower mantle contribute to the low-order geoid. For the geoid to be used as a tool for investigating the earth's dynamic structure, it is necessary to combine information coming from different seismic models and from surface observations. Only when this is done properly and when a large set of possible earth models is tested, is it possible to be confident that the correlation between seismic models and the geoid does constrain the dynamic behavior of the mantle and in particular whether whole mantle convection or layered convection takes place in the earth.

12.4. Geometric Optics Approximation

As mentioned in the introduction, our models are derived under the "geometric optics" approximation. Under that approximation, the phase slowness observed at the station is simply the integral average of the local phase slowness over the source-receiver great circle path (Jordan, 1978). The same approximation is used by Masters et al. (1982) and Woodhouse and Dziewonski (1984). In reality, the observed phase slowness is also affected by heterogeneities that lie off the mean path, and the mean path itself is not a great circle because of refraction effects.

However, there is no tractable theory that would enable us to account for these effects rigorously. Indeed, we do not know how to calculate routinely the synthetic seismograms on an aspherical heterogeneous earth, which is really why we perform only one iteration, and that from a spherical model, to derive our aspherical model. Woodhouse and Girnius (1982) have developped a theory that nicely accounts for the contributions from off-great circle heterogeneities, under the Born approximation of seismic scattering. As noted by Woodhouse and Dziewonski (1984), even that approximate theory, when applied to our inversion problem, would require computations that are far exceeding present possibilities.

It is important to realize that one of the major outcomes of the newly derived aspherical earth models is precisely that they can be used to evaluate quantitatively higher-order effects and help derive a realistic yet tractable theory. Indeed, many different promising approaches are

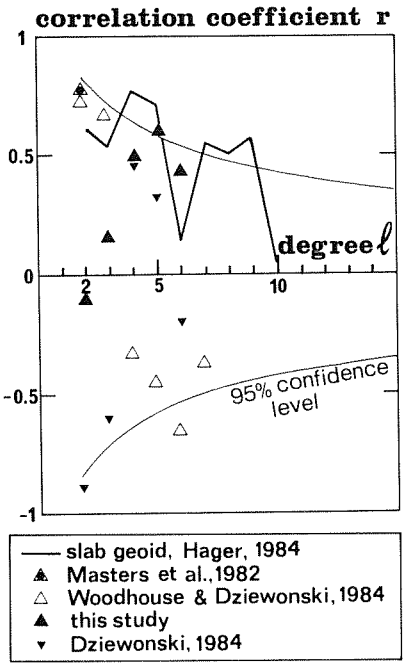

Fig. 35. Correlation coefficients between the real geoid and the predicted geoid for various models, plotted against the degree l. The smooth lines are the limits above (under) which the correlation (anticorrelation) is significant at the 95% confidence level. Triangles are for upper mantle models. Inverted triangles are for a lower mantle model.

now being proposed and tested: ray tracing for surface waves (Lay and Kanamori, 1985), Gaussian beams on a sphere (Jobert and Jobert, 1983; Yomogida and Aki, 1985), variational methods (Tsuboi et al., 1985), first-order asymptotic theory (Romanowicz and Roult, 1986; Davis and Henson, 1986), and other methods (Park and Gilbert, 1984; Dahlen and Henson, 1985; Wong and Woodhouse, 1984).

Now, a legitimate and important question regarding our model is the following: Would our model be very different if the higher order effects that we have neglected were accounted for? This is a difficult question to answer at this stage, since no complete analysis of these effects is feasible. Nevertheless, partial tests now available indicate that although higher-order effects can be quite important locally, they are unlikely to greatly affect the global model that we derived.

For example, Lay and Kanamori (1985) performed surface wave ray tracing using the phase velocity model of NA2. They find that refraction could cause the ray path to deviate from the source-receiver great circle by up to several thousand kilometers in some instances, but that this is not the general case, at least for the R_2 and R_3 wave trains used in NA2. They also show that the amplitude variations predicted by these focusing-defocusing effects (which depend on the second spatial derivative of the heterogeneities) have the right size, and sometimes the right pattern, to explain amplitude variations observed in the data. A similar conclusion is reached by Wong and Woodhouse (1984). Furthermore, Schwartz and Lay (1985) calculated the error made in attributing the phase delay anomaly accumulated on the actual ray path to heterogeneities on the great circle. They find that the error, although it can reach values as high as 12 s locally, is usually much smaller than the errors on the data.

Off-great circle contributions have been analyzed by Woodhouse and Girnius (1982) under the Born approximation. They show that the width of the sensitivity kernel decreases with the period of the surface wave but also depends on the position along the source-receiver great circle, on the focal mechanism and on the epicentral distance, and has many minima and maxima off the great circle. However, when the kernel is integrated against a realistic regionalization, the deviation from the geometric optics approximation is found to be less than 10% at 200 s, except locally (Woodhouse and Girnius, 1982, Figure 4). Nice examples of clear violations of the geometric optics assumption have been presented by Silver and Jordan (1981) and Roult et al. (1986). Most dramatic are the periodic oscillations observed in the eigenfrequency shifts versus mode number plots at some specific epicentral distances Δ. These oscillations are expected on the basis of the first-order asymptotic theory, which predicts deviations from the geometric optics approximation in $\Omega''\left[\tan(l+1/2)\Delta - \pi/4\right]$, where l is the mode number and Ω'' depends on the first or second transverse spatial derivative of the heterogeneities along the path (Woodhouse and Girnius, 1982; Romanowicz and Roult, 1986; Davis and Henson, 1986). Again, Romanowicz and Roult (1986) show that the amplitude of the fluctuations observed in the data is relatively well matched when Ω'' is calculated from the aspherical models of NA2 or Woodhouse and Dziewonski (1984). Obviously, even if Ω'' is very small, the tangent term can lead to tremendous excursions away from the geometric optics approximation for some specific combinations of l and Δ. However, the largest deviations occur at values of l for which the receiver is close to a node (Woodhouse and Girnius, 1982; Romanowicz and Roult, 1986). Although this remains a question to be debated, it seems unlikely that these higher-order effects should produce a systematic bias in our model, but they clearly contribute to the variance of the data that is not accounted for by our model.

13. Conclusions and Perspectives

What have we learned from this study concerning convection in the earth's mantle?

1. On the scale of the tectonic plates, the dominant scale of convection in the upper mantle, several trends have been confirmed. The regionalized models confirm the increase of mantle velocities above 200 km with the age of the ocean floor. This is due to the cooling of the oceanic lithosphere. The spherical harmonic expansion models demonstrate quite clearly the typical signature of ridges (slow) and shields (fast) in the first 250 km. In both approaches, the presence of cold subducted lithosphere below trenches is detected as a pronounced fast S velocity anomaly below about 300 km. All these aspects of convection at the scale of the plates are, of course, well known or at least not unexpected, but their confirmation by observational evidence is worth noting.

2. On a smaller scale, our results raise the interesting possibility that some average properties of sublithospheric small-scale convection have been detected. Thermal boundary layer instabilities could develop under the aging oceanic lithosphere on a horizontal scale of a few hundreds of kilometers. Although such convective plumes would be too small to be detected individually in our study, they might contribute to the observed regional heterogeneities. Inhibited under ridges, they would reach their full strength under old oceanic lithosphere. It is then tempting to see their signature in the difference between young and old oceans at depth. S anisotropy between 200 km and 400 km depth could be telling us the same story: vertical flow under ridges turning into horizontal flow under average age oceans, becoming vertical again under old oceans where the plumes falling off the base of the lithosphere are well developed.

3. At the other extreme, very large scale patterns seem to dominate at large depth. They might reveal the presence of a superscale (degree 2) of convection related to possible degree 2 convection in the lower mantle (Busse, 1983) or to a previous configuration of continental and old oceanic plates. However, even more than in the above discussion where the interaction of small-scale convection with plate circulation was seen to be an important phenomena, the mixing of scales might be difficult to disentangle.

4. Finally, the spherical harmonic maps have revealed the existence of yet another scale of heterogeneities: what we called the "anomalous regions." The strong slow β_V anomaly at shallow depth under the south central Pacific might be related to hot spot activity, which is intense in that region. The strong fast anomaly southeast of South America, also in a region of hot spots, appears more mysterious. This and the fast anomaly under western Australia and the southern Indian Ocean may represent subducted Pacific lithosphere and the consequent cooling of the upper mantle. This would suggest storage of subducted material in the upper mantle.

The superiority of the spherical harmonic expansion approach over the regionalized approach in the domain of scale mixing is that if there is some interaction between different scales of convection in the mantle, it will be a matter of a posteriori interpretation, whereas in the regionalized approach it is intermingled from the beginning.

The present situation with lateral heterogeneities in the mantle is reminescent of the early days of the mapping of the geoid, when the first satellites were launched some 25 years ago. As then for the geoid, the image we get is a coarse one, but it carries in it the seeds of its improvement.

Indeed, the present models can be used to correct for the effects of propagation in source studies and thereby help produce better moment tensors to be used in structural studies (Tanimoto and Kanamori, 1985).

The spherical harmonic representation is well suited for investigating the refraction of surface waves away from great circle paths (Jobert and Jobert, 1983; Wong and Woodhouse, 1983, 1984; Lay and Kanamori, 1985; Yomogida and Aki, 1985). That effect has been neglected in our study and related studies (Woodhouse and Dziewonski, 1984; Masters et al., 1982). It mostly affects the amplitudes of the seismograms. Although difficult, the inversion of amplitudes patterns might prove an important tool for constraining lateral heterogeneities.

In fact, it is probably one of the major advantages of the present models that they can be used to evaluate quantitatively higher-order effects that have been neglected in deriving them. Already many authors have used them to test theories that could in turn greatly improve the present models (e.g., Park and Gilbert, 1984; Davis and Henson, 1986; Tsuboi et al., 1985; Dahlen and Henson, 1985). In particular, methods that can bring information on the spatial derivatives of the heterogeneities should be most useful for deriving better models (Lay and Kanamori, 1985; Wong and Woodhouse, 1984; Romanowicz and Roult, 1986).

Azimuthal anisotropy studies that complement the azimuthally averaged models presented here are already under way (Tanimoto and Anderson, 1984, 1985). These papers show that the inclusion of azimuthal anisotropy has little effect on the maps of heterogeneity. More refined models can also be derived: Tanimoto (1985, 1986) treated the horizontal resolving length and showed that kernels could be constructed with available data that had a radius of about 2000 km.

Finally, the spherical harmonic models make it possible to replace local studies in a global frame.

Nevertheless, and as for the exploration of the gravity field, better tools will also be needed in order to improve the resolution of the spherical harmonic images of mantle heterogeneities.

This means more digital long-period stations around the world to increase the horizontal resolution. Our study has shown that odd harmonics were more poorly determined than even harmonics. This has primarily to do with the fact that direct R_1 or L_1 wave trains cannot be analyzed for great earthquakes because their amplitudes are too large for the dynamical response of the IDA and GDSN seismographs. In that respect, the networks of high dynamical range, three-component seismographs that are now being installed (GEOSCOPE (Romanowicz, 1983; Romanowicz et al., 1984)) or planned (Dziewonski, 1983; Incorporated Research Institutions for Seismology, 1984) are very promising. Concerning the distribution of the stations, we note that the purely sectorial odd coefficients (A_3^3, A_5^5) are among the worst resolved at present.

The vertical resolution will benefit greatly from the analysis of shorter periods and of overtones (Nolet, 1977; Cara, 1979; Lerner-Lam and Jordan, 1983; Nolet et al., 1986). In particular, overtones will be needed to better constrain polarization anisotropy (Lévêque and Cara, 1983, 1985).

Finally, we note that surface waves are unable to discriminate between bulk heterogeneities and heterogeneites due to undulations of the seismic discontinuities. Body waves have been used to look for displacements of the upper mantle seismic discontinuities (e.g., Grand and Helmberger, 1984; Walck, 1984). It will be necessary to have more data in this field if heterogeneities obtained from surface wave studies are to be related to the geoid (Hager, 1984).

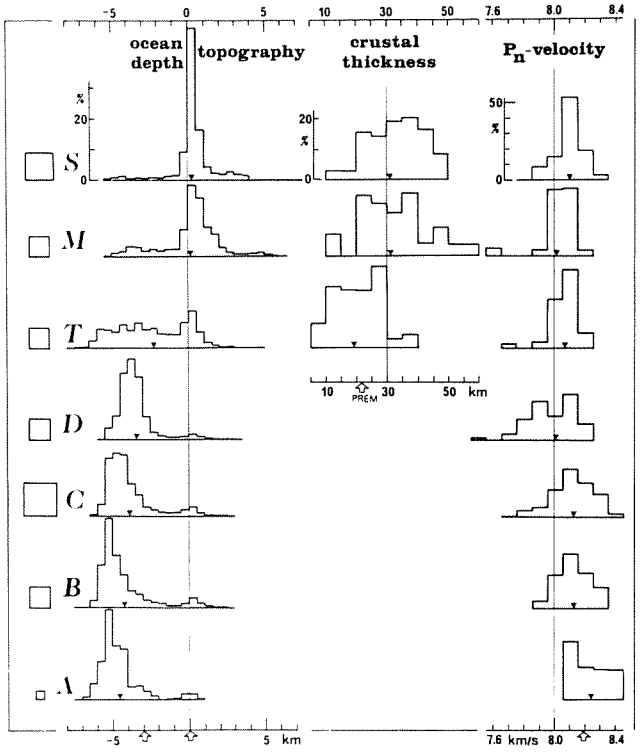

Fig. A1. Surface histograms of ocean depth or topography, crustal thickness, and P_n velocity for the seven tectonic regions defined in Figure 1. For each region the surface of the square on the left indicates the proportion of the earth's surface it covers. The arithmetic averages are marked by triangles. The arrows indicate the values used in PREM.

Appendix A: Shallow Layer Corrections.

Four factors are considered: crustal thickness, P_n-S_n velocities, ocean depth, and topography. The distribution of crustal thickness and P_n velocity is obtained from a compilation of worldwide available data by Soller et al. (1981). The 15° x 15° visual averages are estimated, where possible, from their contoured maps. Ocean depth and topography are from a 5°x5° Rand.Sio compilation.

A.1. Regions

Figure A1 shows the surface distribution histograms of all four factors for the seven different regions. In the oceans, crustal thickness is fairly uniform, and we use the results of Christensen and Salisbury (1975), rather than Soller et al.'s 5 km-spaced contours, to estimate the structure of the crust as a function of age. Averages are calculated for each region and are built into the corresponding starting velocity model. S_n velocities are deduced from the observed P_n velocities by assuming a constant V_{PH}/V_{SH} ratio of 1.78 (equivalent to a Poisson's ratio $\sigma = 0.27$). These velocities at the base of the crust are smoothly connected to a common PREM velocity at 80 km depth.

The crust is assumed to be isotropic, and PREM anisotropy is taken for all starting models. It would be better to include observed P_n anisotropy and to use measured S_n velocities, but these data are too sparse as yet for a global survey to be done. Table A1 gives the crustal model for each region.

A.2. Spherical Harmonics

In order to use the same a priori model for all 49 coefficients of the L = 6 spherical harmonic expansion, we choose to correct the data for the effects due to shallow layers, rather than including them in the starting model as in the previous case. The corrections proceed in three steps: the four factors considered are expanded in spherical harmonics; the correction $\delta T(n)$ to apply for a unit change in each of the factors is computed for each mode number n; the two calculations are combined to produce the corrections to apply to each of the 49 sets of dispersion curves according to the following equation:

$$\Delta T_{lm}(n) = (\delta T_{crust}(n) \times crust_{lm}) + (\delta T_{ocean}(n) \times ocean_{lm}) + (\delta T_{P_n}(n) \times P_n\ velocity_{lm}) + (\delta T_{elev} \times elev_{lm}) \quad (A1)$$

TABLE A1. Crustal Models Chosen for the Seven Tectonic Regions of Okal (1977)

Oceanic Regions	ρ, g/cm³	α, km/s	β, km/s	thickness, km A	B	C	D	T
Ocean	1.02	1.45	0.0	4.6	4.2	3.9	3.4	4.2
Layer 1	2.0	1.65	1.0	0.3	0.2	0.1	0.0	0.2
Layer 2	2.6	5.0	3.0	1.4	1.4	1.4	1.5	1.4
Layer 3	2.9	6.7	3.8	5.0	5.0	5.0	4.0	5.0
	P_n velocity, km/s			8.23	8.12	8.12	8.00	8.12

Continental Regions	ρ, g/cm³	α, km/s	β, km/s	thickness, km M	S
Upper crust	2.4	4.9	2.8	1.0	1.0
Middle crust	2.75	6.0	3.47	20.0	20.0
Lower crust	3.06	6.7	3.79	10.0	10.0
	P_n velocity, km/s			8.01	8.10

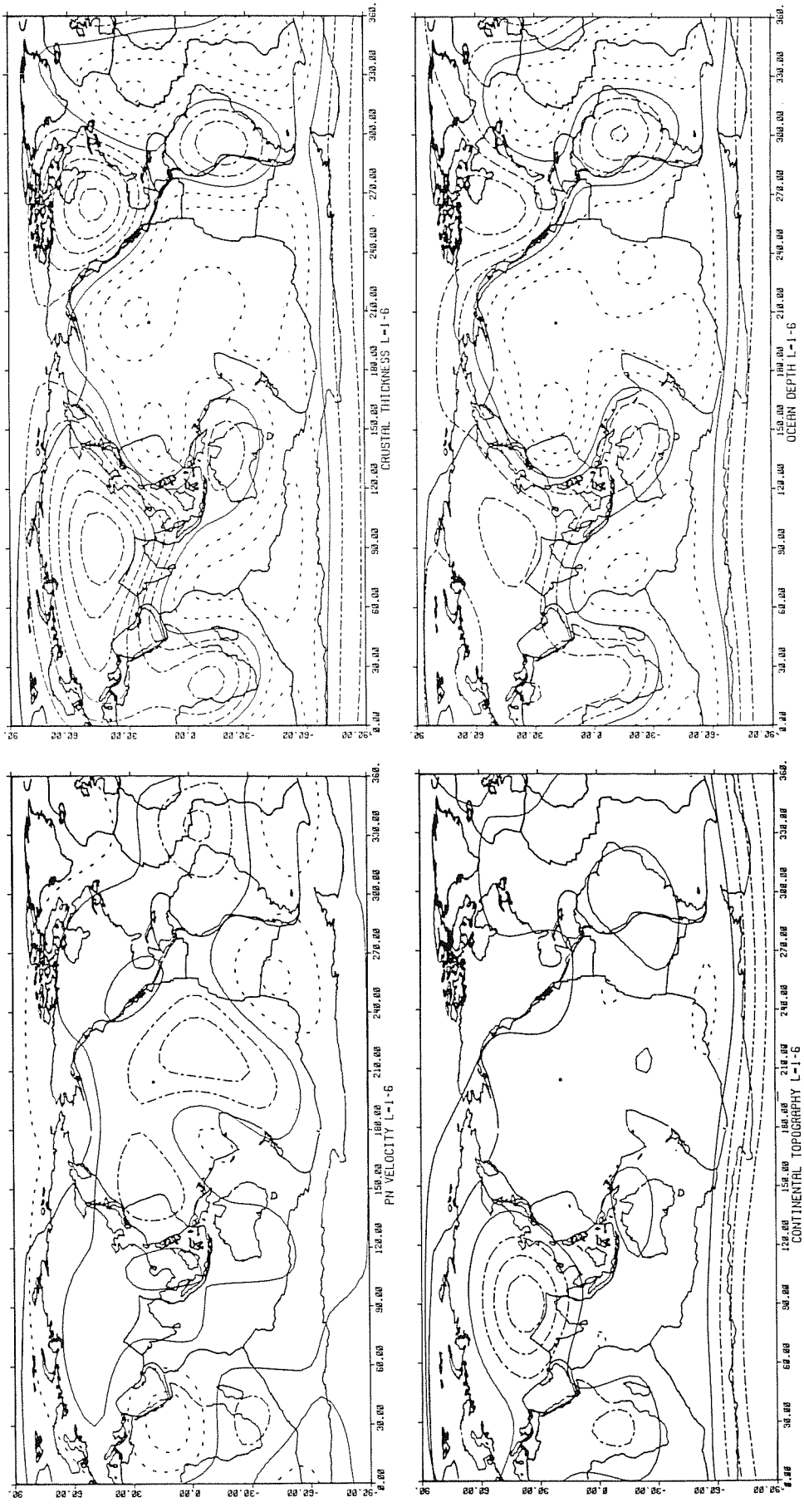

Fig. A2. Contour maps of crustal thickness (in kilometers), P_n velocity (in kilometers per second), ocean depth, and topography (in kilometers), synthetized from their degree 6 spherical harmonic expansion.

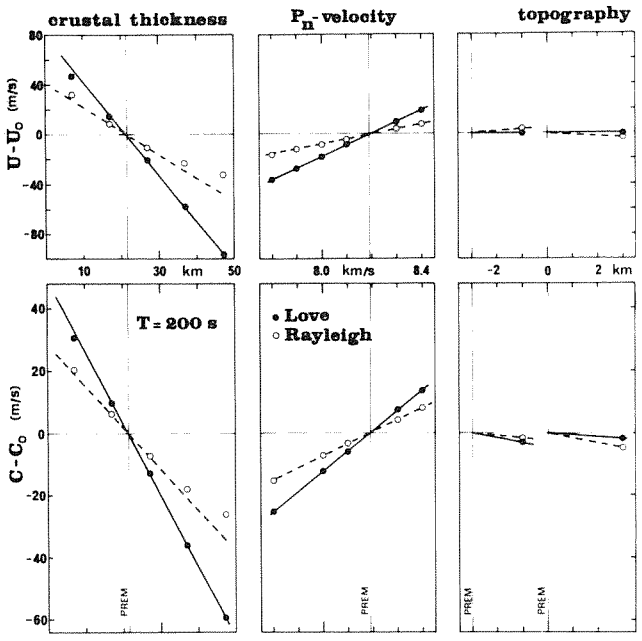

Fig. A3. Variation of the phase and group velocities of 200 s Love and Rayleigh waves for plausible variations in crustal thickness, P_n-S_n velocity, and ocean depth or topography. The straight lines in each graphic are the linearized laws taken to correct the spherical harmonic coefficients. Note that the dominant factor is crustal thickness, which can produce variations in phase velocity up to 2% even at this period.

where $crust_{lm}$, $ocean_{lm}$, ... are the (l,m) spherical harmonic coefficient of the expansion of the corresponding factor (crustal thickness, ocean depth, ...) and $\Delta T_{lm}(n)$ is the total period shift of the normal mode n by which the (l,m) coefficient is corrected. The correction for group slowness is derived in a similar way. It should be noted that our approach assumes that the correction to apply is linearly related to the variation of the parameters for all four factors, over their whole range of variation. This is a good approximation for the corrections due to P_n-S_n velocity, ocean depth, and topography variations. However for crustal thickness, the dominant factor, the approximation is not as good because the thickness of the crust can vary by large amounts from region to region, with the result that some curvature is observed in the correction-versus-variation curve, as we show below. Nevertheless, this nonlinear effect is small enough that no problem arises, considering the uncertainties in the crustal thickness distribution.

A.2.1. Shallow layers in spherical harmonics. The Rand.Sio 5°x5° topography compilation can be directely expanded in spherical harmonics yielding the needed $ocean_{lm}$ and $elev_{lm}$ coefficients. For crustal thickness and P_n velocity, we first fill in the 15°x15° cells that are left empty in Soller et al.'s (1981) contoured maps with the average value obtained for the appropriate tectonic region. With this method, similar to Chapman and Pollack's (1975) tectonic predictor for heat flow, we achieve complete coverage and a spherical harmonic expansion can be performed, yielding the desired $crust_{lm}$ and P_n $velocity_{lm}$ coefficients.

Figure A2 shows the contour maps of crustal thickness, P_n velocity, and topography, obtained by recombining the corresponding spherical harmonic coefficients up to degree L = 6. The latter map is useful for illustrating how crude a picture of actual heterogeneities one gets from limitating the expansion to a maximum degree of

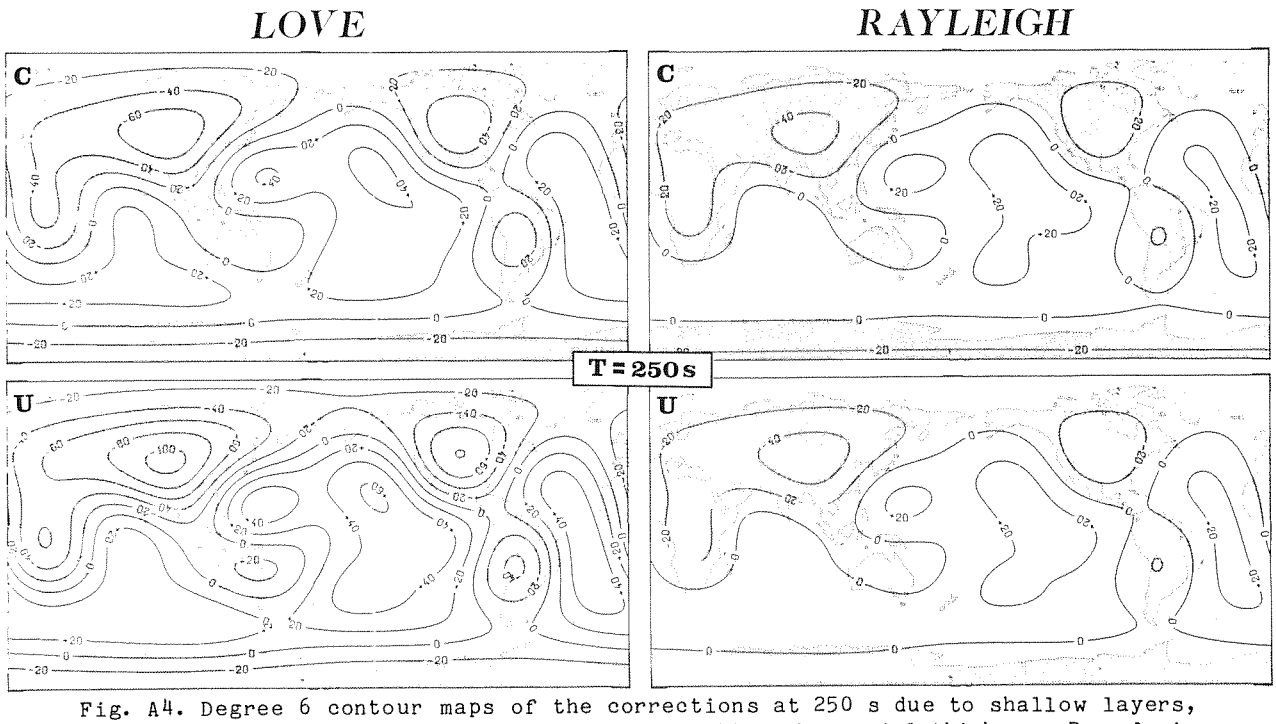

Fig. A4. Degree 6 contour maps of the corrections at 250 s due to shallow layers, obtained by combining the effects of lateral variations in crustal thickness, P_n velocity, and ocean depth or topography. The contour interval is 20 m/s for both phase and group velocities, Love and Rayleigh waves.

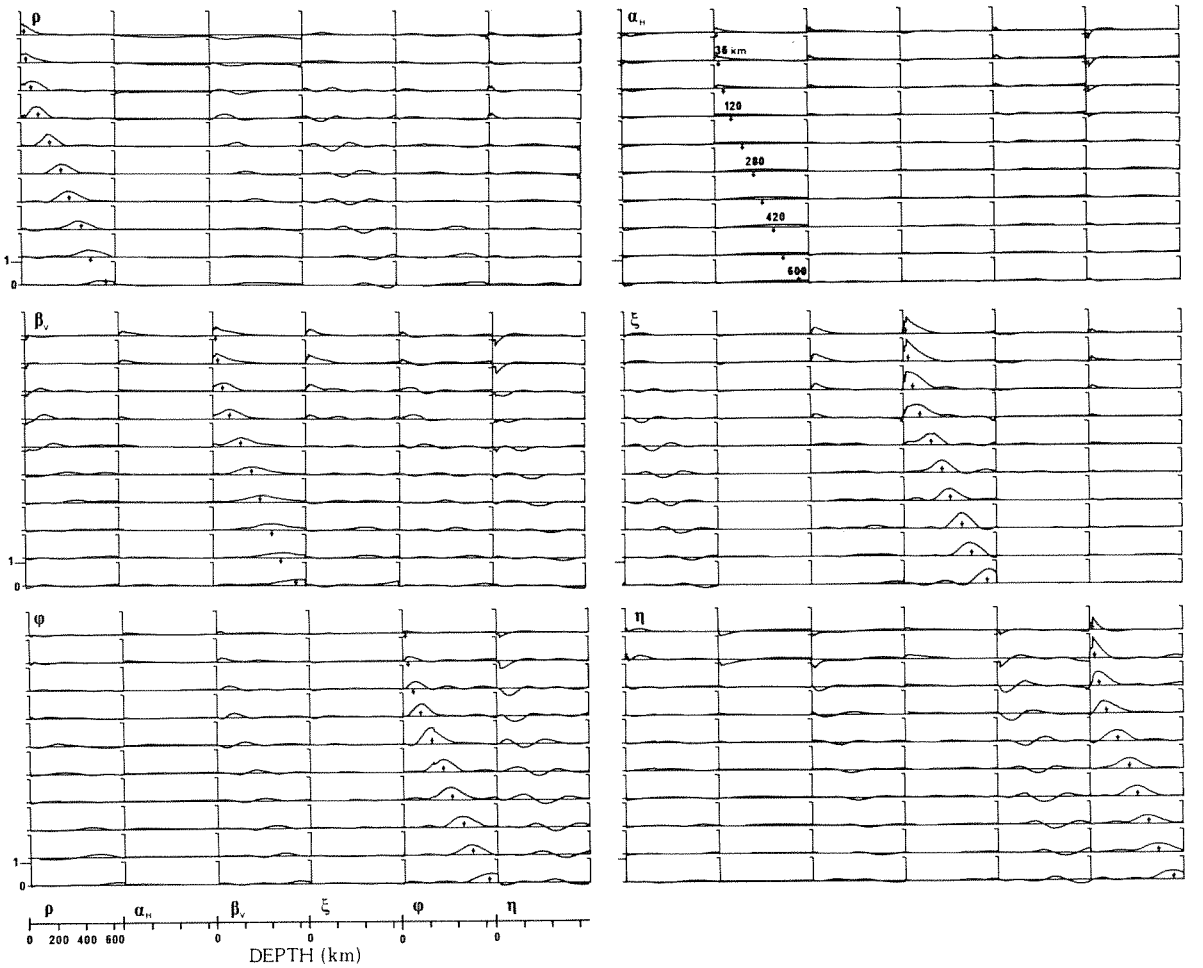

Fig. B1. Resolution kernels obtained for the inversion of a global earth normal modes data set taken from Dziewonski and Anderson (1981). Same conventions as in Figure 8. Units on the vertical axis are 10^{-5} km^{-1}.

L=6. We have tried to make the most complete shallow layer correction possible with available data. The effect of a simple bimodal correction versus no crustal correction can be seen in the work by Woodhouse and Dziewonski (1984).

A.2.2. Corrections. In order to retrieve the $\delta T(n)$ value corresponding to a unit change in the variation of each factor, we calculate the period, phase and group velocities of given normal modes for models that have different crustal thickness, ocean depth, etc. Figure A3 give an example of the corrections produced by reasonable variations of the four different factors. As we need to add the corrections due to all four factors at the end, it is necessary to take these parameters to be as "independent" as possible. For example, the effect of ocean depth is investigated while keeping the thickness of the crust constant (as it would be for a subsiding oceanic lithosphere). As we pointed out, the correction due to crustal thickness is not quite linear over the complete range of its reasonable variations; however the nonlinearity is negligible for variations from 5 km to 30 km, which bracket most of the low-order differences between oceans and continents.

A.2.3. Shallow layer corrections in spherical harmonics. By combining the two preceding steps, corrections are calculated for every spherical harmonic coefficient (l,m) at all needed mode numbers n and are applied to the data. The individual corrections due to all four factors can also be recombined and compared to the corresponding data maps. A few examples of L=6 recombined correction maps are shown in Figure A4.

Appendix B: Resolution Kernels in the Upper Mantle for a PREM Data Subset

We present the resolution kernels obtained from the inversion of the 120 normal modes of the PREM data set (Dziewonski and Anderson, 1981) that are most sensitive to the structure of the upper mantle. The modes we choose are

B.1. Toroidal Modes

Fundamental: n = 4, 6, 8, 10, 14, 20, 24, 28, 32, 36, 40, 44, 48, 52, 56, 60, 64, 67.
First overtone: n = 10, 12, 16, 20, 24, 28, 32, 36, 40, 44, 48, 52, 60, 66.
Second overtone: n = 25, 29, 33, 38, 44, 52, 61.
Third overtone: n = 47, 57, 62, 68, 73.
Fourth overtone: n = 64, 67, 80, 90, 99.
Fifth overtone: n = 79, 105, 118.

B.2. Spheroidal Modes

Fundamental: n = 4, 6, 8, 9, 12, 14, 18, 22, 26, 30, 34, 38, 42, 46, 50, 54, 58, 62, 66, 80,

100, 120, 140, 160.
First overtone: n = 10, 16, 20, 24, 32, 40, 48, 56, 64, 75.
Second overtone: n = 6, 8, 10, 12, 15, 26, 30, 34, 40, 45, 50, 60, 71, 76.
Third overtone: n = 9, 12, 15, 18, 21, 24, 41, 45, 49, 53, 63, 73.
Fifth overtone: n = 11, 14, 19, 23.
Sixth overtone: n = 16, 20, 24, 28.

We use the inversion method described in the text with the following a priori information: a priori model, PREM; no a priori correlation between the six different parameters (ρ, a_H, β_V, ξ, ϕ, η); correlation depth, 1 km; no correlation between the data points; standard deviations on the data as listed by Dziewonski and Anderson (1981). The a priori standard deviations for the parameters are: 0.1 g/cm^3 for ρ; 0.1 km/s for a_H and β_V; 0.1 for ξ, ϕ, and η. These units are used to draw the resolution plot.

Figure B1 displays the resolution kernels. We note that S anisotropy is well resolved and shows little trade-off with the other parameters throughout the upper mantle, except in the top 60 km. This behavior is due to the information brought in by the overtones. On the other hand, even with that extensive data set, ϕ and η cannot be resolved independently, as they show a rather strong mutual trade-off. The low value of the maximum resolution obtained (1.2×10^{-5} km^{-1}) is due to the small a priori correlation length chosen (1 km).

Appendix C: Equivalent Transversely Isotropic Earth

Smith and Dahlen (1973) have calculated the azimuthal dependence of surface wave phase velocities for the most general anisotropic medium with 21 independent C_{ij} elastic coefficients, for the case of weak anisotropy. Montagner and Nataf (1986) show that the average over all azimuths of the phase velocity reduces to a term, which involves five independent combinations of the elastic coefficients. In the special case of a transversely isotropic medium, these five combinations reduce to the A, C, F, L, N elastic coefficients that define such a medium, following Love (1927) and Takeuchi and Saito (1972). As expected, the azimuthal average of surface waves phase velocities in the most general anisotropic medium can therefore be described by means of an equivalent transversely isotropic model. The elastic coefficients of this equivalent model are found as

$$\begin{aligned} A &= \tfrac{3}{8}(C_{11}+C_{22}) + \tfrac{1}{4}C_{12} + \tfrac{1}{2}C_{66} \\ C &= C_{33} \\ F &= \tfrac{1}{2}(C_{13}+C_{23}) \\ L &= \tfrac{1}{2}(C_{44}+C_{55}) \\ N &= \tfrac{1}{8}(C_{11}+C_{22}) - \tfrac{1}{4}C_{12} + \tfrac{1}{2}C_{66} \end{aligned} \qquad (C1)$$

where the C_{ij} are the elastic coefficients of the actual anisotropic medium, in the usual simplified index notation (e.g., Fuchs, 1983). These expressions will prove useful for evaluating the effect different crystal or rock orientations produce on the azimuthal average of surface wave velocities. Realistic examples are given in Appendix D.

Appendix D: Equivalent Transverse Isotropy for Realistic Materials

In this appendix we use the expressions derived in Appendix C to calculate the A, C, F, L, N elastic coefficients of the equivalent isotropic medium for different orientations of olivine single crystals and other earth materials.

D.1. Olivine Single Crystals

We use the following values of the C_{ij} coefficients of olivine single crystals calculated at a 50 km depth and 670°C temperature by Fuchs (1983) from experimental data obtained by Kumazawa and Anderson (1969):

$$C_{ij} = \begin{pmatrix} 3.141 & 0.669 & 0.724 & 0. & 0. & 0. \\ . & 1.890 & 0.781 & 0. & 0. & 0. \\ . & . & 2.265 & 0. & 0. & 0. \\ . & . & . & 0.597 & 0. & 0. \\ . & . & . & . & 0.722 & 0. \\ . & . & . & . & . & 0.725 \end{pmatrix} \qquad (D1)$$

expressed in megabars (1 Mbar = 10^{11} Pa) in the natural **a**-**b**-**c** orthonormal basis of the olivine orthorhombic crystallographic system.

We calculate the coefficients of the equivalent transversely isotropic medium for two different crystal orientations:

1. **a** horizontal, **b** horizontal, **c** vertical

$$\left.\begin{array}{l} A=2.416 \\ C=2.265 \\ F=0.752 \\ L=0.659 \\ N=0.824 \end{array}\right\} \Rightarrow \begin{array}{l} a_H=8.559 \text{ km/s} \\ \beta_V=4.470 \text{ km/s} \\ \xi=1.250 \\ \phi=0.937 \\ \eta=0.686 \end{array} \qquad \begin{array}{l} \frac{SH-SV}{SV}=11.8\% \\ \\ \frac{PV-PH}{PH}=-3.2\% \end{array} \qquad (D2)$$

(in Mbar)

where a density $\rho=3.298$ g/cm^3 has been chosen; equations (C1) have been used to calculate the A, C, F, L, N and equations (4) to calculate a_H, β_V, ς, ϕ, and η.

2. **a** vertical, **b** horizontal, **c** horizontal

$$\left.\begin{array}{l} A=2.052 \\ C=3.141 \\ F=0.696 \\ L=0.723 \\ N=0.623 \end{array}\right\} \Rightarrow \begin{array}{l} a_H=7.888 \text{ km/s} \\ \beta_V=4.684 \text{ km/s} \\ \xi=0.861 \\ \phi=1.531 \\ \eta=1.151 \end{array} \qquad \begin{array}{l} \frac{SH-SV}{SV}=-7.2\% \\ \\ \frac{PV-PH}{PH}=23.7\% \end{array} \qquad (D3)$$

(in Mbar)

D.2. Realistic Anisotropic Mantle

The mantle is not made of perfectly aligned olivine single crystals. However, olivine crystals do show a strong preferred orientation in natural ultramafic rocks on both the sample scale and the massif scale. Using petrofabric field measurements on ophiolites and single crystals elastic coefficients, Peselnick and Nicolas (1978) derive a C_{ij} matrix for lithospheric upper mantle:

$$C_{ij} = \begin{pmatrix} 2.365 & 0.725 & 0.723 & -0.001 & -0.020 & 0.000 \\ . & 2.208 & 0.719 & 0.017 & 0.016 & -0.004 \\ . & . & 2.202 & 0.018 & -0.002 & 0.004 \\ . & . & . & 0.749 & -0.006 & -0.010 \\ . & . & . & . & 0.792 & 0.013 \\ . & . & . & . & . & 0.788 \end{pmatrix} \quad \text{(D4)}$$

where the reference axes are $\mathbf{x}_1$: perpendicular to the ridge; $\mathbf{x}_2$: parallel to the ridge; $\mathbf{x}_3$: vertical (at a 17 km depth and a 250°C temperature).

We deduce the equivalent transverse istropic medium for two different flow patterns:

1. Horizontal flow (i.e., keeping the same axes as in (D4))

$$\left.\begin{array}{l} A=2.290 \\ C=2.202 \\ F=0.721 \\ L=0.770 \\ N=0.784 \\ \text{(in Mbar)} \end{array}\right\} \Longrightarrow \begin{array}{l} a_H=8.324 \text{ km/s} \\ \beta_V=4.828 \text{ km/s} \\ \xi=1.018 \\ \phi=0.961 \\ \eta=0.963 \end{array} \qquad \begin{array}{l} \frac{SH-SV}{SV} = 0.9\% \\ \\ \frac{PV-PH}{PH} = -1.9\% \end{array} \quad \text{(D5)}$$

with a density $\rho=3.305$ g/cm^3.

2. Vertical flow ($\mathbf{x}_1$ vertical, $\mathbf{x}_2$ and $\mathbf{x}_3$ horizontal)

$$\left.\begin{array}{l} A=2.208 \\ C=2.365 \\ F=0.724 \\ L=0.790 \\ N=0.746 \\ \text{(in Mbar)} \end{array}\right\} \Longrightarrow \begin{array}{l} a_H=8.174 \text{ km/s} \\ \beta_V=4.889 \text{ km/s} \\ \xi=0.944 \\ \phi=1.071 \\ \eta=1.153 \end{array} \qquad \begin{array}{l} \frac{SH-SV}{SV} = -2.8\% \\ \\ \frac{PV-PH}{PH} = 3.5\% \end{array} \quad \text{(D6)}$$

These variations are used to place a priori bonds on the expected heterogeneities in the mantle and on the way they correlate.

If the flow in the mantle changes from horizontal in one place to vertical in another place, the variations to expect for the parameters we invert for are deduced from (D5) and (D6) as being

$$\begin{array}{l} \rho = 0. \text{ g/cm}^3 \\ a_H = -0.15 \text{ km/s} \\ \beta_V = 0.061 \text{ km/s} \\ \xi = -0.074 \\ \varphi = 0.11 \\ \eta = 0.19 \end{array} \quad \text{(D7)}$$

Appendix E: Combining Phase and Group Slowness Spherical Harmonic Coefficients

We derive the relationship between the spherical harmonic coefficients of phase slowness on one hand and group slowness on the other hand. At a given "point" (θ,φ) at the surface of the earth, phase and group velocities are related by the usual dispersion formulas, so that one has

$$n(x,\theta,\varphi) = \frac{x}{C(x,\theta,\varphi)} - \frac{1}{2} \quad \text{(E1)}$$

$$\frac{dn}{dx}(x,\theta,\varphi) = \frac{1}{U(x,\theta,\varphi)} \quad \text{(E2)}$$

with $x = (2\pi R_\oplus)/T$, $C(x,\theta,\varphi)$ the phase velocity and $U(x,\theta,\varphi)$ the group velocity at the point (θ,φ) for the period T.

Phase slowness F and group slowness G are expanded in spherical harmonics as

$$F(T,\theta,\varphi) = \sum_l \sum_m f_{lm}(T)\, Y_l^m(\theta,\varphi) \quad \text{(E3)}$$

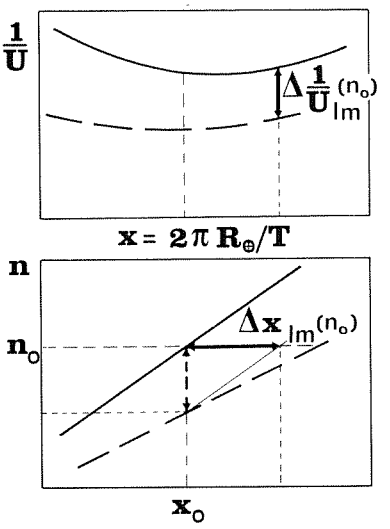

Fig. E1. Schematic drawings showing how to convert from data at a given period $T_o=(2\pi R_\oplus)/x_o$ to data at a given mode number n_o. The solid lines are the dispersion curves for the average earth (l=m=0); the dashed lines are the dispersion curves for the earth perturbed with the (l,m) spherical harmonic term.

$$G(T,\theta,\varphi) = \sum_l \sum_m g_{lm}(T)\, Y_l^m(\theta,\varphi) \quad \text{(E4)}$$

where $Y_l^m(\theta,\varphi)$ stands as an abbreviation of the $\cos m\varphi\, p_l^m(\theta)$ and $\sin m\varphi\, p_l^m(\theta)$ of equation (1). Combining equations (E1) with (E3), and (E2) with (E4), one gets

$$n(x,\theta,\varphi) = \left[\sum_l \sum_m x\, f_{lm}(x)\, Y_l^m(\theta,\varphi)\right] - \frac{1}{2} \quad \text{(E5)}$$

$$\frac{dn}{dx}(x,\theta,\varphi) = \sum_l \sum_m g_{lm}(x)\, Y_l^m(\theta,\varphi) \quad \text{(E6)}$$

These equations being true for any (θ,φ), it follows that

$$y_{lm}(x) = x\, f_{lm}(x) \quad \text{(E7)}$$

$$y_{lm}'(x) = g_{lm}(x) \quad \text{(E8)}$$

and we can apply our method for fitting a smooth $y_{lm}(x)$ curve knowing the values y_{lm} takes and the values its derivative y_{lm}' takes at selected points x_i. We can thus test the compatibility of phase and group data for each individual coefficient.

However, it remains to convert these data at given x_i (i.e., given periods T_i) to data at given mode numbers n, the problem being that y_{lm} is no longer the mode number. Figure E1 shows how the conversion is performed, the approximation used being valid when the lateral heterogeneities are small as compared to the average term l=m=0.

For a given mode number n_o, one has

$$\Delta T_{lm}(n_o) = 2\pi R_\oplus \left(\frac{1}{x_o + \Delta x_{lm}(n_o)} - \frac{1}{x_o}\right) \quad \text{(E9)}$$

with $x_o = (2\pi R_\oplus)/T$ and $n_o = x_o\, f_{oo}(x_o) - \frac{1}{2}$ and

$$\Delta x_{lm}(n_o) = -\frac{x_o\, f_{lm}(x_o)}{g_{oo}(x_o)} \qquad (E10)$$

the group slowness anomaly at a given n_o is given by

$$\Delta\left[\frac{1}{U}\right]_{lm}(n_o) = g_{lm}\left[x_o + \Delta x_{lm}(n_o)\right] \qquad (E11)$$

Integer n_o values are picked, and the $\Delta T_{lm}(n_o)$ is calculated according to equations (E9) and (E10) from the smooth $y_{lm}(x)$ curve constructed to fit the phase and group slowness data.

Our approach rests upon the dispersion relationship $C = \omega/k$ and $U = d\omega/dk$. These relationships are not strictly valid when attenuation is taken into account (see, for example, Kanamori and Anderson (1977)). Numerical tests indicate that the actual group velocity can deviate from the theoretical $U = d\omega/dk$ relationship by 0.01 km/s for PREM-like attenuation. This systematic error is of the same order as the experimental errors on the measurement of group velocities (NA2), but its effect can be important when fitting the better resolved average earth (l=m=0) group velocities, which have errors less than 0.002 km/s (NA2). It is worth noting that the same bias is introduced when partial derivatives for group velocity are calculated by numerical differentiation of phase velocity kernels, following the method of Rodi et al. (1975), which also is based upon the $U = d\omega/dk$ relationship.

Acknowledgments. The authors wish to thank Nelly Jobert for making computer facilities available to us and Adam Dziewonski for a computer program. Brigitte Hannetelle and Yanick Ricard kindly provided some of the data used in Figure 35. We acknowledge useful suggestions and comments from Albert Tarantola, Jean-Paul Montagner, Janice Regan, Brad Hager, Jean-Jacques Lévêque, Michel Cara, Barbara Romanowicz, Hiroo Kanamori, John Woodhouse, Dave Harkrider, Tom Hearn, and Bernard Valette. We thank two anonymous reviewers for useful criticisms. This research was supported in part by National Science Foundation, Earth Sciences Section grants EAR 811-5236 and EAR 831-7623. Contribution 4144, Division of Geological and Planetary Sciences, California Institute of Technology, Pasadena, California. Most numerical results presented in this paper are available in a computer compatible format. Color versions of some of our β_V and ξ maps have appeared in the works by Anderson (1984) and Dziewonski and Anderson (1984).

References

Aki K., A. Christofferson and E.S. Husebye, Determination of the three-dimensional seismic structure of the lithosphere, J. Geophys. Res., 82, 277-296, 1977.

Anderson Don L., Elastic wave propagation in layered anisotropic media, J. Geophys. Res., 66, 2953-63, 1961.

Anderson Don L., Surface wave tomography, Eos Trans. AGU, 65, 147-148, 1984.

Anderson Don L., Latest information from seismic observations, in The Earth's Mantle, edited by T. F. Gaskell, pp. 355-420, Academic, Orlando, Fla., 1967.

Anderson Don L. and J. Regan, Uppermantle anisotropy and the oceanic lithosphere, Geophys. Res. Lett., 10, 841-844, 1983.

Anderson Don L. and M.N. Toksöz, Surface waves on a spherical Earth. 1, Upper mantle structure from Love waves, J. Geophys. Res., 68, 3483-3500, 1963.

Babuška V., J. Plomerová and J. Šilený, Spatial variations of P residuals and deep structure of the European lithosphere, Geophys. J. R. astr. Soc., 79, 363-384, 1984.

Backus G.E., Geographical interpretation of measurements of average phase velocities of surface waves over great circular and great semicircular paths, Bull. Seismol. Soc. Am., 54, 571-610, 1964.

Backus G.E., Converting vector and tensor equations to scalar equations in spherical coordinates, Geophys. J. R. astr. Soc., 13, 71-101, 1967.

Backus G. and F. Gilbert, Numerical applications of a formalism for geophysical inverse problems, Geophys. J. R. astr. Soc., 13, 247-276, 1967.

Backus G. and F. Gilbert, The resolving power of gross earth data, Geophys. J. R. astr. Soc., 16, 169-205, 1968.

Backus G. and F. Gilbert, Uniqueness in the inversion of inaccurate gross earth data, Philos. Trans. R. Soc. London., 266, 123-192, 1970.

Bamford D., Refraction data in western Germany--A time-term interpretation, Z. Geophys., 39, 907-927, 1973.

Bamford D. and S. Crampin, Seismic anisotropy--The state of the art, Geophys. J. R. astr. Soc., 49, 1-8, 1977.

Brune J. and J. Dorman, Seismic waves and earth structure in the Canadian shield, Bull. Seismol. Soc. Am., 53, 167-210, 1963.

Busse F.H., Quadrupole convection in the lower mantle?, Geophys. Res. Lett., 10, 285-288, 1983.

Cara M., Lateral variations of S-velocity in the upper mantle from higher Rayleigh modes, Geophys. J. R. astr. Soc., 57, 649-670, 1979.

Chapman D.S. and H.N. Pollack, Global heat flow: A new look, Earth Planet. Sci. Lett., 28, 23-32, 1975.

Christensen N.I. and M.H. Salisbury, Structure and composition of the lower oceanic crust, Rev. Geophys., 13, 57-86, 1975.

Christensen N.I. and M.H. Salisbury, Seismic anisotropy in the oceanic upper mantle: Evidence from the Bay of Islands ophiolite complex, J. Geophys. Res., 84, 4601-4610, 1979.

Crampin S., E.M. Chesnokov and R.G. Hipkin, Seismic anisotropy--The state of art, II, Geophys. J. R. astr. Soc., 76, 1-16, 1984.

Dahlen F.A. and I.H. Henson, Asymptotic normal modes of a laterally heterogeneous earth, J. Geophys. Res., 90, 12,653-12,681, 1985.

Davis J.P. and I.H. Henson, Validity of the great circular average approximation for inversion of normal mode measurements, Geophys. J. R. astr. Soc., in press, 1986.

Dorman J., M. Ewing and J. Oliver, Study of shear velocity distribution in the upper mantle by mantle Rayleigh waves, Bull. Seismol. Soc. Am., 50, 87-115, 1960.

Dziewonski A.M., On regional differences in dis-

persion of mantle Rayleigh waves, Geophys. J. R. astr. Soc., 22, 289-325, 1971.
Dziewonski A.M., The philosophy of PLATO, (abstract), Eos Trans. AGU, 64, 767, 1983.
Dziewonski A.M., Mapping the lower mantle: Determination of lateral heterogeneity in P velocity up to degree and order 6, J. Geophys. Res., 89, 5929-5952, 1984.
Dziewonski A.M. and Don L. Anderson, Preliminary reference earth model, Phys. Earth Planet. Inter., 25, 297-356, 1981.
Dziewonski A.M. and Don L. Anderson, Seismic tomography of the earth's interior, Am. Sci., 72, 483-494, 1984.
Dziewonski A.M. and J.M. Steim, Dispersion and attenuation of mantle waves through waveform inversion, Geophys. J. R. astr. Soc., 70, 503-527, 1982.
Fleitout L. and D.A. Yuen, Secondary convection and the growth of the oceanic lithosphere, Phys. Earth Planet. Inter., 36, 181-212, 1984.
Forsyth D.W., The early structural evolution and anisotropy of the oceanic upper mantle, Geophys. J. R. astr. Soc., 43, 103-162, 1975.
Franklin J.N., Well-posed stochastic extensions of ill-posed linear problems, J. Math. Anal. Appl., 31, 682-716, 1970.
Fuchs K., Recently formed elastic anisotropy and petrological models for the continental subcrustal lithosphere in southern Germany, Phys. Earth Planet. Inter., 31, 93-118, 1983.
Gilbert F., Differential kernels for group velocity, Geophys. J. R. astr. Soc., 44, 649-660, 1976.
Grand S. and D.V. Helmberger, Upper mantle shear structure of North America,Geophys. J. R. astr. Soc, 76, 399-438, 1984.
Hager B.H., Subducted slabs and the geoid: Constraints on mantle rheology and flow, J. Geophys. Res., 89, 6003-6016, 1984.
Hager B.H., R.W. Clayton, M.A. Richards, R.P. Comer and A.M. Dziewonski, Lower mantle heterogeneity, dynamic topography and the geoid, Nature, 313, 541-545, 1985.
Harkrider D.B. and Don L. Anderson, Computation of surface wave dispersion for multilayered anisotropic media, Bull. Seismol. Soc. Am., 52, 321-332, 1962.
Hearn T., P_n travel times in southern California, J. Geophys. Res., 89, 1843-1855, 1984.
Hess H., Seismic anisotropy of the uppermost mantle under oceans, Nature, 203, 629-631, 1964.
Hess H.H., Mid-oceanic ridges and tectonics of the sea-floor, in Submarine Geology and Geophysics, Colston Pap. 17, pp. 317-333, Butterworths, Stoneham, Mass., 1965.
Houseman G, Large aspect ratio convection cells in the upper mantle, Geophys. J. R. astr. Soc., 75, 309-334, 1983.
Houseman G. and D.P. McKenzie, Numerical experiments on the onset of convective instability in the earth's mantle, Geophys. J. R. astr. Soc., 68, 133-164, 1982.
Incorporated Research Institutions for Seismology, Science plan for a New Global Seismographic Network, Washington, D.C., 1984.
Jackson D.D., The use of a priori data to resolve non-uniqueness in linear inversion, Geophys. J. R. astr. Soc., 57, 137-157, 1979.
Jaupart C. and B. Parsons, Convective instabilities in a variable viscosity fluid cooled from above, Phys. Earth Planet. Inter., 39, 14-32, 1985.
Jobert N. and G. Jobert, An application of ray theory to the propagation of waves along a laterally heterogeneous spherical surface, Geophys. Res. Lett., 10, 1148-1151, 1983.
Jordan T.H., Estimation of the radial variation of seismic velocities and densities in the Earth, Ph.D. thesis, 199 pp., California Institute of Technology, Pasadena, 1973.
Jordan T.H., The continental tectosphere, Rev. Geophys., 13, 1-12, 1975.
Jordan T.H., A procedure for estimating lateral variations from low-frequency eigenspectra data, Geophys. J. R. astr. Soc., 52, 441-455, 1978.
Jordan T.H. and J.N. Franklin, Optimal solutions to a linear inverse problem in Geophysics, Proc. Natl. Acad. Sci. U.S.A., 68, 291-293, 1971.
Journet B. and N. Jobert, Variation with age of anisotropy under oceans, from great circle surface waves, Geophys. Res. Lett., 9, 179-181, 1982.
Kanamori H., Velocity and Q of mantle waves, Phys. Earth Planet. Inter., 2, 254-275, 1970.
Kanamori H. and Don L. Anderson, Importance of physical dispersion in surface waves and free oscillation problems, Rev. Geophys., 15, 105-112, 1977.
Kawakatsu H., Can 'pure-path' models explain free oscillation data?, Geophys. Res. Lett., 10, 186-189, 1983.
Kumazawa M. and O.L. Anderson, Elastic moduli, pressure derivatives and temperature derivatives of single crystal olivine and single crystal forsterite, J. Geophys. Res., 74, 5961-72, 1969.
Lay T. and H. Kanamori, Geometric effects of global lateral heterogeneity on long-period surface wave propagation, J. Geophys. Res., 90, 605-621, 1985.
Lerner-Lam A. and T.H. Jordan, Earth structure from fundamental and higher mode waveform analysis, Geophys. J. R. astr. Soc., 75, 754-798, 1983.
Lévêque J.-J., Regional upper mantle S-velocity models from phase velocities of great-circle Rayleigh waves, Geophys. J. R. astr. Soc., 63, 23-43, 1980.
Lévêque J.-J. and M. Cara, Long period Love wave overtone data in North America and the Pacific ocean: New evidence for upper-mantle anisotropy, Phys. Earth Planet. Inter., 33, 164-179, 1983.
Lévêque J.-J. and M. Cara, Inversion of multimode surface wave data: evidence for sublithospheric anisotropy, Geophys. J. R. astr. Soc., 83, 753-774, 1985.
Love A.E.H., The Mathematical Theory of Elasticity, Cambridge University Press, New York, 1927.
Masters G., T.H. Jordan, P.G. Silver and F. Gilbert, Aspherical earth structure from fundamental spheroidal-mode data, Nature, 609-613, 1982.
McKenzie D.P., Some remarks on heat flow and gravity anomalies, J. Geophys. Res., 72, 6261-6273, 1967.
McKenzie D.P., Surface deformation, gravity anom-

alies and convection, Geophys. J. R. astr. Soc., 48, 211-238, 1977.
McKenzie D.P., Finite deformation during fluid flow, Geophys. J. R. astr. Soc., 58, 689-715, 1979.
Mitchell B.J. and G.-K. Yu, Surface wave dispersion, regionalized velocity models, and anisotropy of the Pacific crust and upper mantle, Geophys. J. R. astr. Soc., 63, 497-514, 1980.
Montagner J.-P., Seismic anisotropy of the Pacific ocean inferred from long-period surface waves dispersion, Phys. Earth Planet. Inter., 28, 28-50, 1985.
Montagner J.-P., Regional three-dimensional structures using long-period surface waves, Ann. Geophys., in press, 1986.
Montagner J.-P. and N. Jobert, Investigation of upper mantle structure under young regions of the southeast Pacific using long-period Rayleigh waves, Phys. Earth Planet. Inter., 27, 206-222, 1981.
Montagner J -P. and N. Jobert, Variation with age of the deep structure of the Pacific ocean inferred from very long-period Rayleigh wave dispersion, Geophys. Res. Lett., 10, 273-276, 1983.
Montagner J.-P. and H.-C. Nataf, A simple method for inverting the azimuthal anisotropy of surface waves, J. Geophys. Res., 91, 511-520, 1986.
Morgan W.J., Convection plumes in the lower mantle, Nature, 230, 42-43, 1971.
Morris G.B., R.W. Raitt and G.G. Shor, Velocity anisotropy and delay-time maps of the mantle near Hawaii, J. Geophys. Res., 74, 4300-4316, 1969.
Nakanishi I., Shear velocity and shear attenuation models inverted from the world-wide and pure-path average data of mantle Rayleigh waves ($_0S_{25}$ to $_0S_{80}$) and fundamental spheroidal modes ($_0S_2$ to $_0S_{24}$), Geophys. J. R. astr. Soc., 66, 83-130, 1981.
Nakanishi I. and Don L. Anderson, World-wide distribution of group velocity of mantle Rayleigh waves as determined by spherical harmonic inversion, Bull. Seismol. Soc. Am., 72, 1185-1194, 1982.
Nakanishi I. and Don L. Anderson, Measurements of mantle wave velocities and inversion for lateral heterogeneity and anisotropy, 1, Analysis of great circle phase velocities, J. Geophys. Res., 88, 10267-84, 1983.
Nakanishi I. and Don L. Anderson, Measurements of mantle wave velocities and inversion for lateral heterogeneity and anisotropy, 2, Analysis by the single-station method, Geophys. J. R. astr. Soc., 78, 573-618, 1984
Nataf H.-C., I. Nakanishi and Don L. Anderson, Anisotropy and shear-velocity heterogeneities in the upper mantle, Geophys. Res. Lett., 11, 109-112, 1984.
Nicolas A., J.-L. Bouchez, F. Boudier and J.-C. Mercier, Textures, structures and fabrics due to solid state flow in some European lherzolites, Tectonophysics, 12, 55-86, 1971.
Nolet G., The upper mantle under western Europe inferred from the dispersion of Rayleigh modes, Z. Geophys., 43, 265-285, 1977.
Nolet G., J. van Trier and R. Huisman, A formalism for nonlinear inversion of seismic surface waves, Geophys. Res. Lett., 13, 26-29, 1986.
Okal E.A., The effect of intrinsic oceanic upper-mantle heterogeneity on regionalization of long-period Rayleigh-wave phase velocities, Geophys. J. R. astr. Soc., 49, 357-370, 1977.
Park J. and F. Gilbert, Computed splitting of multiplets by aspherical models of the structure of the mantle (abstract), Eos Trans. AGU, 65, 1002, 1984.
Parsons B. and D.P. McKenzie, Mantle convection and the thermal structure of the plates, J. Geophys. Res., 83, 4485-4496, 1978.
Peselnick L. and A. Nicolas, Seismic anisotropy in an ophiolite peridotite: Application to oceanic upper mantle, J. Geohys. Res., 83, 1227-1235, 1978.
Peselnick L., A. Nicolas and P.R. Stevenson, Velocity anisotropy in a mantle peridotite from the Ivrea zone: Application to upper mantle anisotropy, J. Geophys. Res., 79, 1175-1182, 1974.
Raitt R.W., G.G. Shor, T.J.G. Francis and G.B. Morris, Anisotropy of the Pacific upper mantle, J. Geophys. Res., 74, 3095-3109, 1969.
Regan J. and Don L. Anderson, Anisotropic models of the upper mantle, Phys. Earth Planet. Inter., 35, 227-263, 1984.
Ricard Y., L. Fleitout and C. Froidevaux, Geoid heights and lithospheric stresses for a dynamical earth, Ann. Geophys., 2, 267-286, 1984.
Richards M.A. and B.H. Hager, Geoid anomalies in a dynamical earth, J. Geophys. Res., 89, 5987-6002, 1984.
Richter F.M. and B. Parsons, On the interaction of two scales of convection in the mantle, J. Geophys. Res., 80, 2529-2541, 1975.
Rodi W.L., P. Glover, T.M.C. Li and S.S. Alexander, A fast, accurate method for computing group-velocity partial derivatives for Rayleigh and Love modes, Bull. Seismol. Soc. Am., 65, 105-114, 1975.
Romanowicz B., Seismic structure of the upper mantle beneath the United States of America by 3-dimensional inversion of body wave arrival times, Geophys. J. R. astr. Soc, 57, 479-506, 1979.
Romanowicz B., Geoscope: A new long period three component global seismic network, Terra Cognita, 3, 301-305, 1983.
Romanowicz B. and G. Roult, First order asymptotics for the eigenfrequencies of the earth and application to the retrieval of large scale lateral variations, Geophys. J. R. astr. Soc., in press, 1986.
Romanowicz B., M. Cara, J.M. Fels and D. Rouland, Geoscope: A French initiative in long-period three components global seismic networks, Eos Trans. AGU, 65, 753-754, 1984.
Roult G., B. Romanowicz and N. Jobert, Observations of departures from classical approximations on very long period GEOSCOPE records, Ann. Geophys., in press, 1986.
Sabatier P.C., Positivity constraints in linear inverse problems, I, General theory, Geophys. J. R. astr. Soc., 48, 415-441, 1977a.
Sabatier P.C., Positivity constraints in linear inverse problems, II, Applications, Geophys. J. R. astr. Soc., 48, 443-459, 1977b.
Satô Y., Attenuation, dispersion, and the wave guide of the G wave, Bull. Seismol. Soc. Am., 48, 231-251, 1958.
Schlue J.W. and L. Knopoff, Shear wave polariza-

tion anisotropy in the Pacific Basin, Geophys. J. R. astr. Soc., 49, 145-165, 1977.
Schwab F. and E. Kausel, Long-period surface wave seismology: Love wave phase velocity and polar phase shift, Geophys. J. R. astr. Soc., 45, 407-435, 1976.
Schwartz S. and T. Lay, Comparison of long-period surface wave amplitude and phase anomalies for two models of global lateral heterogeneity, Geophys. Res. Lett., 12, 231-234, 1985.
Silver P.G. and T.H. Jordan, Fundamental spheroidal mode observations of aspherical heterogeneity, Geophys. J. R. astr. Soc., 64, 605-634, 1981.
Smith M.L. and F.A. Dahlen, The azimuthal dependence of Love and Rayleigh wave propagation in a slightly anisotropic medium, J. Geophys. Res., 78, 3321-33, 1973.
Soller D.R., R.D. Ray and R.D. Brown, A global crustal thickness map, Phoenix Corp., McLean, Virginia, 1981.
Souriau A. and M. Souriau, Test of tectonic models by great circle Rayleigh waves, Geophys. J. R. astr. Soc., 73, 533-551, 1983.
Stacey F.D., Physics of the Earth, 2nd ed., 329 pp., John Wiley, New York, 1977.
Takeuchi H. and M. Saito, Seismic surface waves, Methods Comput. Phys., 11, 217-295, 1972.
Tanimoto T., The Backus-Gilbert approach to the three-dimensional structure in the upper mantle, I, Lateral variation of surface wave phase velocity with its error and resolution, Geophys. J. R. astr. Soc., 82, 105-124, 1985.
Tanimoto T., The Backus-Gilbert approach to the three-dimensional structure in the upper mantle, II, SH and SV velocity, Geophys. J. R. astr. Soc., 84, 49-70, 1986.
Tanimoto T. and Don L. Anderson, Mapping convection in the mantle, Geophys. Res. Lett., 11, 287-290, 1984.
Tanimoto T. and Don L. Anderson, Lateral heterogeneity and azimuthal anisotropy of the upper mantle: Love and Rayleigh waves 100-250 s, J. Geophys. Res., 90, 1842-1858, 1985.
Tanimoto T. and H. Kanamori, Linear programming approach to moment tensor inversion of earthquake sources and some tests on the three-dimensional structure of the upper mantle, Geophys. J. R. astr. Soc., 84, 413-430, 1986.
Tarantola A. and B. Valette, Inverse problems = quest for information, J. Geophys., 50, 159-170, 1982a.
Tarantola A. and B. Valette, Generalized nonlinear inverse problems solved using the least squares criterion, Rev. Geophys., 20, 219-232, 1982b.
Toksöz M.N. and Don L. Anderson, Phase velocities of long-period surface waves and structure of the upper mantle, 1, Great circle Love and Rayleigh wave data, J. Geophys. Res., 71, 1649-1658, 1966.
Tsuboi S., R.J. Geller and S.P. Morris, Partial derivatives of the eigenfrequencies of a laterally heterogeneous earth model, Geophys. Res. Lett., 12, 817-820, 1985.
Turcotte D.L. and E.R. Oxburgh, Finite amplitude convective cells and continental drift, J. Fluid Mech., 28, 29-42, 1967.
Vetter U. and J.-B. Minster, P_n velocity anisotropy in southern California, Bull. Seismol. Soc. Am., 71, 1511-1530, 1981.
Walck M.C., The P-wave upper mantle structure beneath an active spreading center: The Gulf of California, Geophys. J. R. astr. Soc., 76, 697-723, 1984.
Wielandt E., First-order asymptotic theory of the polar shift of Rayleigh waves, Pure Appl. Geophys., 118, 1214-1227, 1980.
Wielandt E. and L. Knopoff, Dispersion of very long-period Rayleigh waves along the East Pacific Rise: Evidence for S wave velocity anomalies to 450 km depth, J. Geophys. Res., 87, 8631-8641, 1982.
Wiggins R.A., The general linear inverse problem: Implication of surface waves and free oscillations for earth structure, Rev. Geophys., 10, 251-285, 1972.
Wong Y.K. and J.H. Woodhouse, Ray theory for surface waves on a sphere (abstract), Eos Trans. AGU, 64, 260, 1983.
Wong Y.K. and J.H. Woodhouse, Amplitude, phase and path anomalies for mantle waves (abstract), Eos Trans. AGU, 65, 244, 1984.
Woodhouse J.H. and A.M. Dziewonski, Mapping the upper mantle: Three-dimensional modeling of earth structure by inversion of seismic waveforms, J. Geophys. Res., 89, 5953-5986, 1984.
Woodhouse J.H. and T.P. Girnius, Surface waves and free oscillations in a regionalized earth model, Geophys. J. R. astr. Soc., 68, 653-673, 1982.
Wu F.T., Mantle Rayleigh wave dispersion and tectonic provinces, J. Geophys. Res., 77, 6445-6453, 1972.
Yomogida K. and K. Aki, Waveform synthesis of surface waves in a laterally heterogeneous earth by the Gaussian beam method, J. Geophys. Res., 90, 7665-7688, 1985.
Yu G.K. and B.J. Mitchell, Regionalized shear velocity models of the Pacific upper mantle from observed Love and Rayleigh wave dispersion, Geophys. J. R. astr. Soc., 57, 311-341, 1979.

Don L. Anderson, Seismological Laboratory, California Institute of Technology, Pasadena, CA 91125.

I. Nakanishi, Department of Geophysics, Faculty of Science, Hokkaido University, Sapporo, 060, Japan.

H.-C. Nataf, Laboratoire de Géophysique et Géodynamique interne, Bâtiment 510, Université Paris-Sud, 91405 Orsay Cedex, France.

(Received April 8, 1985;
revised October 21, 1985;
accepted January 30, 1986.)